

The Electrocatalytic Reduction of CO₂ on Cu and Ag Based Nanoparticle Electrodes

Masterthesis

by

Kees Kolmeijer



supervised by

Dr. Longfei Wu

Dr. Ward van der Stam

First examiner: Dr. W. van der Stam

Second examiner: Dr. F.T. Rabouw

Inorganic chemistry and Catalysis
Debye institute of Nanomaterial Science
Utrecht University
The Netherlands

February 2021

Acknowledgements

From start till end, I have received a great deal of support during my master project by a wide verity of people for which I am very thankful for. This includes my supervisors, associated and non associated PhD candidates, fellow students and friends within and outside of the ICC research group.

First, I would like to thank dr. Ward van der Stam for the supervision over my project. Ward allowed me the freedom to explore every possible direction that my project could take and as a result allowed me to develop a strong foundation as a scientist and the confidence to try different approaches and new directions.

Secondly I would like to thank my second supervisor dr. Longfei Wu, who through our discussions helped me translate and formulate my thoughts and experiments into a form that is credible and presentable.

While being the first member official member of the newly established electrocatalysis research group by Ward, I was also the least experienced. Therefore I would like to thank Jochem Wijten, Hongyu An, Longfei Wu and Shuang Yang for showing me the ropes of electrochemistry and catalysis as well as for the help and guidance throughout my project. Furthermore I would like to thank the electrocatalysis group members that joined shortly after, Pedro Mazaira Couce, Joris Janssens, Jim de Ruiter, Thimo Jacobs and Jan Hollander. While our time together was mostly limited by corona or spent online in team meetings, a group feeling was certainly present and made working much more enjoyable.

Trough collaboration with the University of Antwerpen and the University of Eindhoven part of my research was published. For this I would like to thank Yue Zhang, Marta Costa Figueiredo, Emiel J. M. Hensen from Eindhoven and Sven Arnouts, Sara Bals, Thomas Altantzis from Antwerpen. Being part of the development of the manuscript was exciting and insightful.

Abstract

Nanostructured electrodes provide a promising strategy for the efficient reduction of CO₂ by electrical catalysis. However nanostructured electrodes have been reported to suffer from severe stability issues as a result of potential induced aggregation under electrochemical conditions causing the loss of the original shape and structure. Measured faradaic efficiencies usually resembles the respective bulk component of the material. In this master thesis, colloidally synthesized copper and silver nanoparticles with a narrow size distribution (<10%) and dominant (111) surface facet are used in the electrochemical CO₂ reduction reaction. Severe aggregation of nanoparticles was observed for monometallic electrodes already at mild reaction conditions starting at -0.8 V vs. RHE, determined from *ex situ* SEM imaging with faradaic efficiencies resembling their bulk component. However, by co-deposition of Cu and Ag nanoparticles forming binary electrodes, the stability was greatly increased at CO₂ reducing potentials of -0.8V vs. RHE. The observed stability effect allowed for the determination of the intrinsic selectivity of the Cu (10% methane) and Ag (9% CO) nanoparticles. We attribute the observed stabilisation effect to the immiscible character of the Cu and Ag lattice. This stabilization effect allows for the design of highly active nanostructured electrocatalyst for the CO₂ reduction reaction with high durability.

Table of Contents

Introduction	5
1 Theoretical background	9
1.1 Electrochemistry	9
1.1.1 What is electrochemistry?	9
1.1.2 Electrocatalysis	10
1.1.3 Half reactions of the CO ₂ Reduction Reaction	10
1.1.4 Electrochemical H-cell reactor	11
1.1.5 Cyclic voltammetry and electrochemical active surface area	13
1.1.6 Chronoamperometry and faradaic efficiency	14
1.2 CO ₂ reduction Mechanism	16
1.2.1 CO ₂ adsorption and reaction pathways	16
1.2.2 Rate-determining steps	16
1.2.3 Copper bimetallic electrodes	17
1.3 Crystal structure	18
1.3.1 Structure-Function	18
1.3.2 Unit cell	18
1.3.3 Miller index notation	19
1.3.4 X-ray diffraction techniques	20
1.3.5 Electron crystallography	21
1.3.6 Diffraction patterns and unit cells	21
1.4 Metal nanoparticle colloidal synthesis	22
1.4.1 Colloidal synthesis	22
1.4.2 Heat-up synthesis	22
1.4.3 Classical nucleation theory	24
1.4.4 Interactions between metals and ligands	25
1.4.5 Localised surface plasmon resonance	26
1.5 Characterisation and element quantification	27
1.5.1 Electron microscopy	27
1.5.2 High angle annular dark field imaging	28
1.5.3 Energy-dispersive X-ray spectroscopy	28
1.5.4 Inductively coupled plasma atomic optical emission spectrometry	29
1.5.5 X-ray photoelectron spectroscopy	29
1.5.6 Vibrational spectroscopy	30
2 Nanoparticle synthesis and characterisation	31
2.1 Experimental methods and materials	31
2.1.1 Chemicals	31
2.1.2 Cu nanoparticle synthesis	31
2.1.3 Ag nanoparticle synthesis	33
2.2 Characterization techniques	34
2.2.1 UV/Vis-spectroscopy	34

2.2.2	Transmission electron microscopy and electron diffraction	34
2.2.3	X-ray diffraction	34
2.2.4	X-ray photoelectron spectroscopy	34
2.3	Results and Discussion	35
2.3.1	Cu nanoparticle synthesis optimisation	35
2.3.2	Ag nanoparticle synthesis optimisation	37
2.3.3	Crystal structure determination of Cu and Ag nanoparticles	38
2.3.4	Cu nanoparticle surface species	41
2.3.5	Ag nanoparticle surface species	43
3	Electrochemical measurements and catalysis	45
3.1	Experimental methods and materials	45
3.1.1	Activity set-up	45
3.1.2	Electrode preparation	45
3.2	Characterization techniques	46
3.2.1	Inductively coupled plasma optical emission spectrometry	46
3.2.2	Infrared spectroscopy (<i>ex situ</i>)	46
3.2.3	Raman spectroscopy (<i>in situ</i>)	46
3.2.4	Scanning electron microscopy (<i>ex situ</i>)	46
3.3	Electrochemical measurements	46
3.3.1	Cyclic voltammetry	46
3.3.2	Chronoamperometry	46
3.4	Results and discussion	47
3.4.1	Study of ligands under CO ₂ RR conditions	47
3.4.2	Study of the electrode surface and oxide species during the CO ₂ RR	51
3.4.3	Dropcasted Cu nanoparticle electrodes faradaic efficiency/stability	53
3.4.4	Dropcasted Ag nanoparticle electrodes faradaic efficiency/stability	55
3.4.5	Dropcasted Cu-Ag nanoparticle electrodes faradaic efficiency/stability	57
3.4.6	Electrochemical active surface area	60
3.4.7	Cu and Cu-Ag nanoparticle electrodes by electrophoresis deposition faradaic efficiency/stability	61
3.4.8	Comparison between drop-casting and electrophoresis deposition	63
4	Conclusions	64
5	Outlook	65
	Appendix	66
	References	75

Introduction

Reducing greenhouse gas emission has been a world wide concern for the last few years, as negligence could lead to environmental catastrophes due to global warming. To address this issue, parties of the international environmental treaty called the United Nations Framework Convention on Climate Change (UNFCCC) constructed the “Paris Agreement” in 2015. After its presentation at the climate conference in Paris, the agreement was signed by 189 countries, including The Netherlands. By signing the agreement, countries are legally obliged to “keep the increase in global average temperature to below 2°C above pre-industrial levels; and pursue efforts to limit the increase to 1.5°C”. By following this temperature guideline, the impacts and risks of climate change would be substantially reduced.¹

To realise the temperature target of the Paris Agreement, the European Union (EU) responded with “The European Green Deal” in 2019, a detailed plan describing the requirements for each member state to pursue the 1.5°C goal. Most notably, a huge emphasis was put on the reduction of emitted greenhouse gasses. In 2030 members of the European Union should strive for a reduction of emitted CO₂ by 55%, and in 2050 all parties should strive for a climate neutral economy. These drastic measures call for a balance between anthropogenic emissions by sources and removals by sinks of greenhouse gasses. Therefore, the development of novel technologies providing carbon negative solutions is necessary. One of these promising developments is the electrocatalytic reduction of CO₂ into hydrocarbons (CO₂RR), creating a pathway that uses CO₂ as a feedstock to store electrical energy into chemical bonds at room temperature and ambient pressure.^{2,3} This process turns CO₂ into a circular resource, which would be the essence of a carbon neutral economy (figure 1).

Fundamental studies of the electrochemical CO₂ reduction reaction started as early as the 19th century, and has vastly advanced in recent years. Beginning with the comprehensive studies by Hori. In 1994, Hori published the selectivity and activity of various bulk metal electrodes for CO₂ reduction in aqueous electrolyte.⁴ From these results, each metal could be assigned to a group with the same main product. The reported groups were: CO (Au, Ag, Zn, Pd and Ga), HCOO⁻ (Pb, Hg, In, Sn, Cd, and Ti), H₂ (Ni, Fe, Pt and Tl) and lastly the hydrocarbon group which is solely occupied by copper. Hori attributed the unique carbon coupling capability of Cu to the stabilization of adsorbed CO₂ and COOH intermediates at its surface. Further investigation by the computational studies of Norskov in 2012 revealed that Cu is distinct from other metals by having an intermediate *CO binding strength, achieving a balance of barriers for activation of CO₂ and hydrogenation of *CO.^{5,6} When used as an electrode, Cu produces a wide range of products including: 33% methane (CH₄), 26% ethylene (C₂H₄), 9% Formate (HCOO⁻), 6% Propanol (PrOH), 1% CO and lastly 20% hydrogen (H₂) at an applied electric potential of -1.05V vs RHE. Unfortunately, the broad selectivity of products, and a lacking selectivity for long hydrocarbons combined with the high required potential, makes bulk copper electrodes unsuitable for commercial use. To make electrochemical CO₂ reduction worthwhile, the selectivity for ethylene must either be drastically increased or a reasonable selectivity for C₂₊ products needs to be achieved.

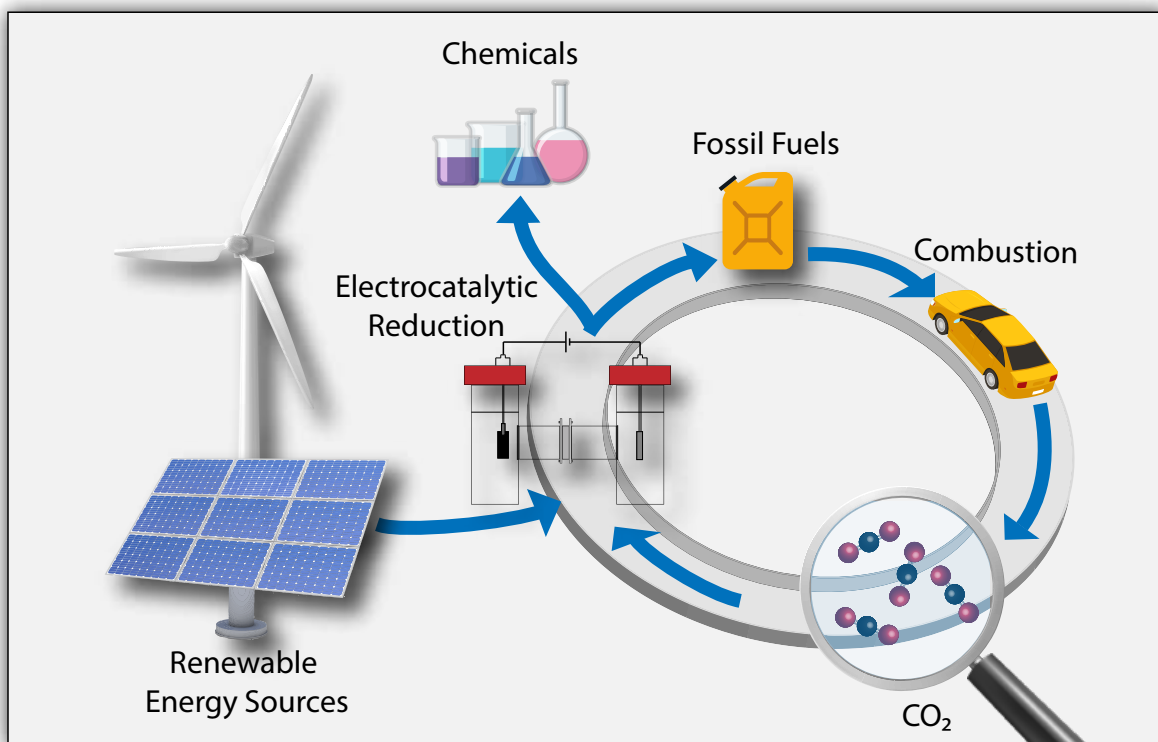


Figure 1: Example of how electrocatalytic reduction can turn CO₂ into a circular resource with the use of electricity provided by renewable energy sources and carbon capture techniques.

Electrode design strategies

To enhance the selectivity towards C_{2+} products, multiple electrode design strategies have been researched in the past few years in order to make the CO_2RR a viable pathway for CO_2 conversion. From various series of Cu single crystal experiments by Hori starting from 1995, it was found that the nature of the surface has a close relation with the selectivity towards a certain reaction product.⁷⁻⁹ For example, single crystal Cu(111) possessed an increased selectivity towards CH_4 and for Cu(100) C_2H_4 selectivity was increased with respect to a polycrystalline electrode. Also, it was revealed that higher selectivity for C_2H_4 could be achieved by introducing steps and kinks of (111) or (110) to the Cu(100) basal plane of a Cu(100) terrace surface. Fine-tuning the Cu surface by a controlled synthesis approach could therefore be a promising strategy to increase selectivity.

The second strategy is the use of nanostructured electrodes. Generally, nanoparticle electrocatalysts outperform bulk electrocatalysts with respect to activity and selectivity. Due to the much higher surface area, the selectivity correlation of under-coordinated facets will be more pronounced as they are much more abundant. Also, nanoparticles are highly compatible with specialised electrical cell reactors as the nanoparticles can be deposited into porous or other high surface area electrodes. In these reactors mass transfer limitations are minimized increasing the overall efficiency of the reaction.¹⁰⁻¹³

The last strategy to enhance the selectivity of a Cu electrocatalyst, is the addition of metals from different product groups to make binary or alloyed electrodes. Most notably, binary electrodes with metals of the CO group have been reported to greatly enhance the selectivity towards C_{2+} products.¹⁴⁻¹⁷ CO is widely accepted as an important intermediate in the CO_2RR as surface adsorbed CO is thought to be involved in the rate limiting steps for both C_1 and C_{2+} products.¹⁸⁻²² Locally increasing the CO concentration with CO producing active sites could therefore increase the selectivity for hydrocarbons by spilled over CO to a hydrocarbon producing active site of Cu.

Colloidal Synthesis

A highly tunable synthesis method is required to realise nanoparticles abundant in the hydrocarbon promoting surface facets Cu(111) and Cu(100). For this reason, a colloidal synthesis approach is preferred. Colloidal chemistry allows for precise control over size, shape and composition. Furthermore, colloidal chemistry is scalable and can be solution processed on any desired substrate.²³ lastly, By mixing of colloidal dispersions, the development of well mixed bimetallic electrodes can be realised. A possible negative aspect of colloidal chemistry are the organic ligands that are bound to the surface of the colloidal particles, which might hinder the accessibility of the surface and hence impede the reactivity. However, other techniques to prepare catalytic nanoparticles without ligands, such as wet impregnation, suffer from reproducibility and polydispersity issues, which limits the use of *in-situ* spectroscopy and diffraction techniques with ensemble statistics. Furthermore, ligands aid in the stability of the colloidal particles however it has been reported to be stripped of within the first hour of electrolysis insinuating a balance between surface accessibility and stability.²⁴

Project Outline

To rationally design the ultimate CO₂RR catalyst, detailed fundamental understanding of structure-function relationships is crucial. That is why in this master thesis the effectiveness of the three electrode design strategies for the CO₂RR is put up to the test by developing electrodes that are: 1. Abundant in the methane producing facet Cu(111) or Cu(100) 2. Nanoscale, ensuring high surface area and 3. Bimetallic by mixing of Cu and Ag colloidal dispersions. To achieve these electrodes, highly monodisperse Ag and Cu nanoparticles have been synthesised by a colloidal chemistry approach and used to create mono and bimetallic nanostructured electrodes. Of the nanoparticles, the size and shape are determined from high resolution transmission electron microscopy imaging. A detailed characterisation was performed of the surface structure by electron and X-ray diffraction techniques and the Cu surface species has been examined by X-ray photoelectron spectroscopy (XPS) and Energy-dispersive X-ray spectroscopy (EDX). The presence of the organic ligands of the colloidal nanoparticles during the CO₂RR was investigated by *in situ* Raman and *ex situ* infrared spectroscopy. The Faradaic efficiency of the nanostructured electrodes was determined from gas chromatography peak area of gaseous products using an electrochemical H-cell with aqueous electrolyte. Lastly the stability of the nanoparticle films after the CO₂RR was examined by *ex situ* scanning electron microscopy (SEM). An overall outline of the project is shown in figure 2.

By using a combination of these various diffraction, imaging and spectroscopic techniques before and after or during the CO₂RR, insight can be obtained on dynamic effects such as potential induced surface reconstruction, surface oxygen stripping and ligand interactions, elucidation of structure-function relationships and the determination of possible synergistic effects between Cu and Ag nanoparticles in terms of selectivity and stability.

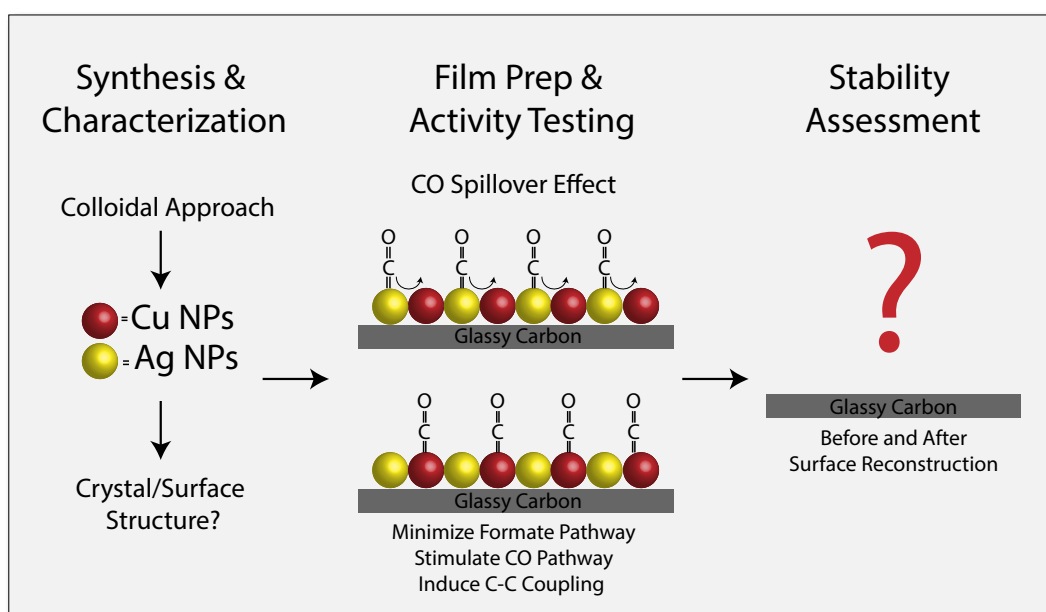


Figure 2: Project Outline

1 Theoretical background

1.1 Electrochemistry

1.1.1 What is electrochemistry?

Electrochemistry is the branch of physical chemistry that studies the relationship between electrical energy and chemical change. This relationship can be perceived in both ways. In batteries electrical energy is gained from spontaneous reactions that occur within the battery. Inversely, in electrolysis electrical energy is used to drive chemical reactions that would otherwise be non-spontaneous. A key characteristic of any electrochemical process, in either direction, is the direct transfer of electrons between molecules and/or atoms. Such a reaction is called a redox reaction, of which many can occur in a single electrochemical process. In electrochemistry, these reactions are studied by using electrodes with an intervening electrolyte connected to an external electric circuit. In figure 3, examples are given of a galvanic cell (electrical battery) and an electrolysis cell used for water splitting. On each electrode parts of the redox reaction occurs, called a half reaction. Half reactions where electrons are gained occur on the cathode and are called reduction reactions, whereas half reactions that generate electrons occur on the anode and are called oxidation reactions. The electrolyte between the electrodes, usually a solution of ions, ensures electrical conductivity. For both batteries and electrolysis cells, the type of electrode material used is crucial for an efficient reaction. For electrolysis these electrode materials are studied based on their electrocatalytic capability.

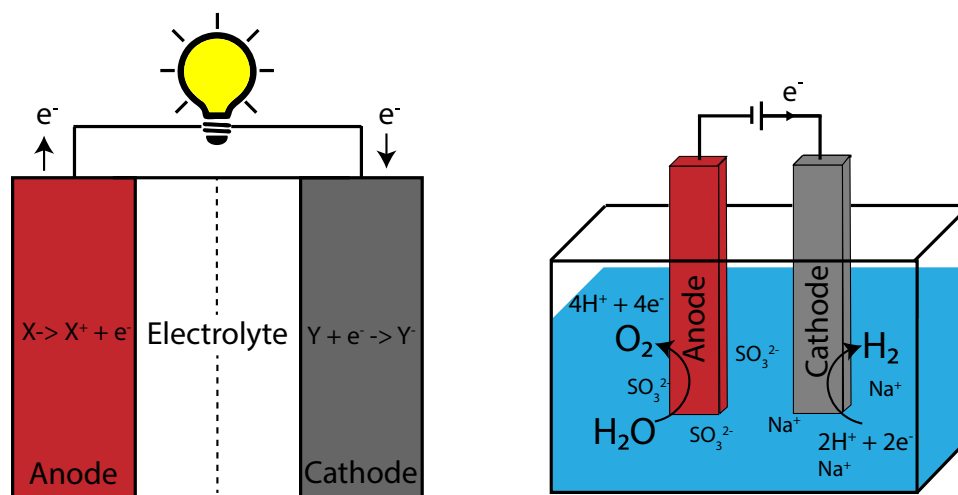


Figure 3: Left, a schematic of a galvanic cell and right a schematic of a electrolysis cell for water splitting with their respective half reactions.

1.1.2 Electrocatalysis

Electrocatalysis is the subject of electrochemistry that puts the focus on the relation between the rates of electrochemical reactions and the surface properties of the electrode at which these reactions take place. In redox reactions, the electrode is not truly inert. Other than its general function to feed current through the electrolyte, it also functions as a catalyst by providing a reaction mechanism involving surface bound intermediates and transition states that decrease the overall activation energy required for the chemical reaction.^{5,18,25-34} A lower activation energy usually results in a drastic increase in the reaction rate, making otherwise slow or high energy consuming reactions much more efficient. Furthermore, a catalyst is also able to promote the rate of certain individual reaction steps in chemical reactions with parallel pathways, thus influencing the selectivity of the overall reaction.²⁶⁻³⁴

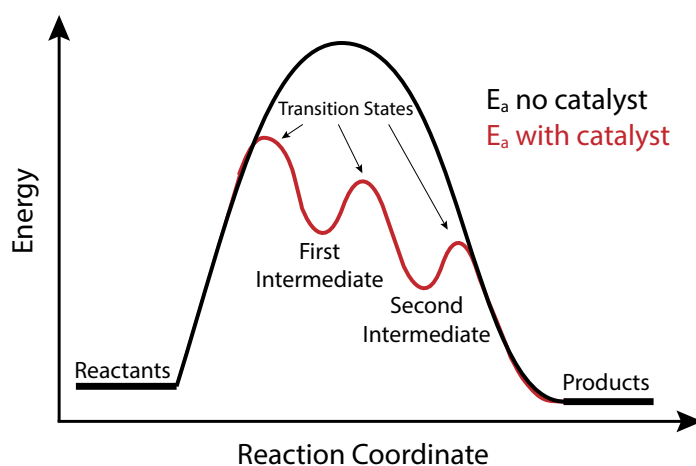


Figure 4: Difference in activation energy (E_a) of the same reaction with and without a catalyst.

1.1.3 Half reactions of the CO₂ Reduction Reaction

The reactions of interest that are catalysed in the CO₂RR are the half reactions that occur on the cathode. As one can imagine in the study of the CO₂RR, realising the reduction reactions of CO₂ is of great importance; however, some reactions are more desired than others based on the value of the resulting products. To increase selectivity towards the more valuable ethylene for example, suppression of competing half reactions is required. A collection of the most common half reactions that can occur during the CO₂RR with their corresponding equilibrium potential is given in table 1. To make a complete redox reaction, the oxidation of water in the oxygen evolution reaction is required to supply the CO₂RR of protons and electrons. With a general copper catalyst, each half reaction involving the reduction of CO₂ in table 1 will occur to some extent, together with the competing hydrogen evolution reaction.

Table 1: (Product) Names of common CO₂RR half reactions and their respective equilibrium potential. Table adapted from ref [35].

Reaction	E^0 /[V vs. RHE]	(Product) Name
$2\text{H}_2\text{O} \rightarrow \text{O}_2 + 4\text{H}^+ + 4\text{e}^-$	1.23	Oxygen evolution reaction
$2\text{H}^+ + 2\text{e}^- \rightarrow \text{H}_2$	0	Hydrogen evolution reaction
$\text{CO}_2 + 2\text{H}^+ + 2\text{e}^- \rightarrow \text{HCOOH}(\text{aq})$	-0.12	Formic acid
$\text{CO}_2 + 2\text{H}^+ + 2\text{e}^- \rightarrow \text{CO}(\text{g}) + \text{H}_2\text{O}$	-0.10	Carbon monoxide
$\text{CO}_2 + 8\text{H}^+ + 8\text{e}^- \rightarrow \text{CH}_4(\text{g}) + 2\text{H}_2\text{O}$	0.17	Methane
$2\text{CO}_2 + 12\text{H}^+ + 12\text{e}^- \rightarrow \text{C}_2\text{H}_4(\text{g}) + 3\text{H}_2\text{O}$	0.08	Ethylene

1.1.4 Electrochemical H-cell reactor

To execute electrochemical reactions in a controlled manner, an electrochemical cell reactor is used. A commonly used electrochemical cell for the study of the CO₂RR is the H-cell. The H-cell consist of two compartments, the anodic side and the cathodic side which are separated by a proton-exchange membrane allowing for the generated protons and electrons from the counter electrode to reach the working electrode without cross contamination. As the studied reaction is the CO₂RR, the working electrode is cathodic and the counter electrode where the oxygen evolution reaction takes place is anodic. For the reliable measurement of electrode potentials, a reference electrode is required. A reference electrode is a highly stable electrode which when used allows for precise measurement of the potential and current of the working electrode. The reference electrode also allows for the measurements performed using different working electrodes to be comparable. Each of the electrodes is connected to a potentiostat, an electric device which allows over the control of the current or potential one wants to apply for a particular experiment. Furthermore, all three electrodes are submerged in an aqueous electrolyte. For the CO₂RR, generally a solution of potassium bicarbonate (KHCO₃) is used, however other carbonate salts could be used instead, and have been reported to have some effect on the selectivity of the CO₂RR.³⁶⁻⁴¹ Lastly, the H-cell reactor typically features a connection to feed CO₂ and other gasses and an outlet to a detection instrument such as a gas chromatograph or a mass spectrometer for product quantification. Liquid products can be collected and analysed by techniques such as high pressure gas chromatography or nuclear magnetic resonance. A schematic figure illustrating each component of the H-cell is given in figure 5.

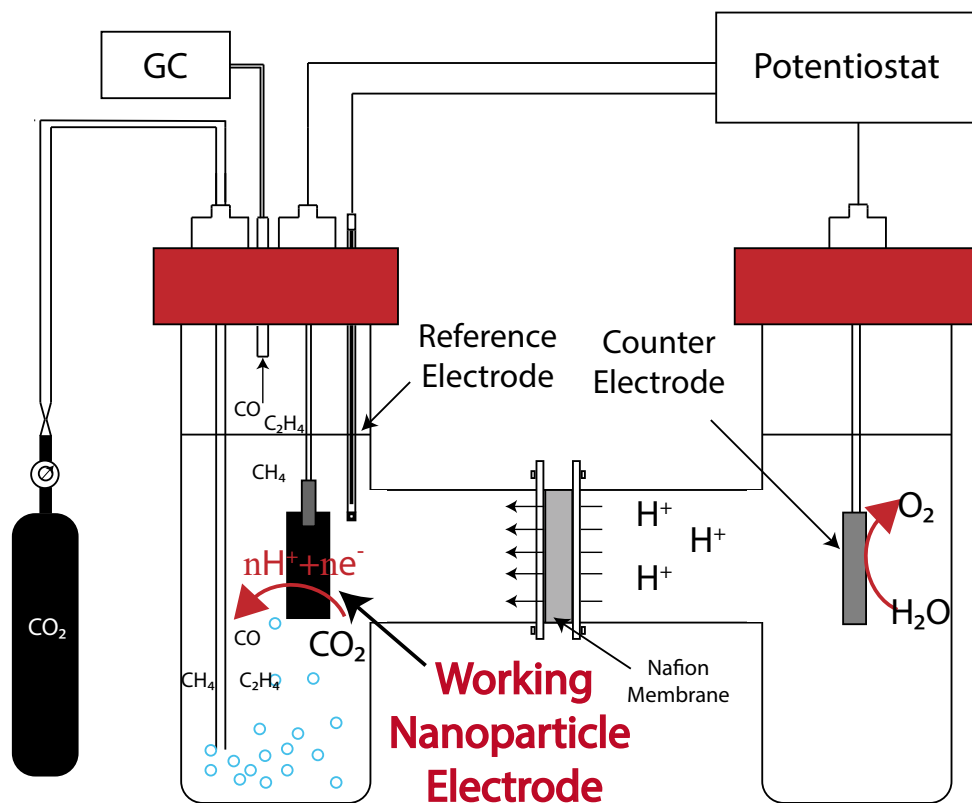


Figure 5: Schematic representation of an electrochemical h-cell used for the CO₂RR.

1.1.5 Cyclic voltammetry and electrochemical active surface area

An important electrochemical method for the analysis of the CO₂RR is cyclic voltammetry. Cyclic voltammetry (CV) is an electrochemical technique used to study the reduction and oxidation reactions that occur at the working electrode. This allows for the determination of the change in oxidation state of the electrode or electron transfer-initiated chemical reactions that occur at the electrodes surface within a window of scanning potential with respect to the measured current.^{42,43} An example of a simple cyclic voltammogram can be seen in figure 6a. A graph of CV consists of two parts, a reduction part where the potential is scanned with a specific rate (mVs⁻¹) from an oxidizing to a reducing potential and an oxidation part where the potential is scanned from a reducing potential back to the initial oxidizing potential value. Any peaks that may be observed along the way indicate a half reaction of a species that has occurred on the electrode. These half reactions change the concentration of said species causing a change in electrode potential. The relationship between the concentration of oxidized and reduced analytes and electrode potential is described by the Nernst equation in equation 1.⁴²

$$E = E^0 + \frac{RT}{nF} \ln \frac{(\text{Ox})}{(\text{Red})} = E^0 + 2.3026 \frac{RT}{nF} \log_{10} \frac{(\text{Ox})}{(\text{Red})} \quad (1)$$

Where E is the potential (V) of an electrochemical cell related to the standard potential (V) of a species E⁰ and the relative activities of the oxidized (Ox) and reduced (Red) analyte at equilibrium. R is the ideal gas constant J.K⁻¹.mol⁻¹, T is temperature in K, n is the number of moles and F is the Faraday constant in C.mol⁻¹

Other than insight about electrochemical processes that occur at the surface also information can be obtained about the surface area of the electrode. From the charging current measured with different scanning rates in a non-faradaic region, the active electrochemical surface area (ECSA) can be calculated. In a non-faradaic region no electron transfer reactions take place, a flow of current is still present however due to the charge and discharge in the electric double layer formed at the electrode interface by the cations and anions from the electrolyte. The flow within the double layer causes the observable offset between the reduction and the oxidation scan in a CV. Accumulation of these charges leads to capacitance within the double layer, illustrated in figure 6b.⁴⁴ The double layer capacitance is calculated from the slope of a linear fit of the charging current measured at varying scan rates in a non-faradaic region.⁴⁵ The scan rate of the experiment controls how fast the applied potential is scanned. Faster scan rates result in a decrease in the size of the diffusion layer causing higher currents increasing the offset between the slopes of the scan, as illustrated in figure 6c.⁴²

For the calculation of the ECSA of a catalytic film, first the roughness factor (R_f) must be calculated. The roughness factor is defined as the ratio of the double layer capacitance of the sample (C) and the double layer capacitance of the substrate (C_s), R_f = C/C_s. Once obtained the ECSA can be calculated by multiplication of the roughness factor times the geometric surface area of the electrode, ECSA = R_f × S.⁴⁵

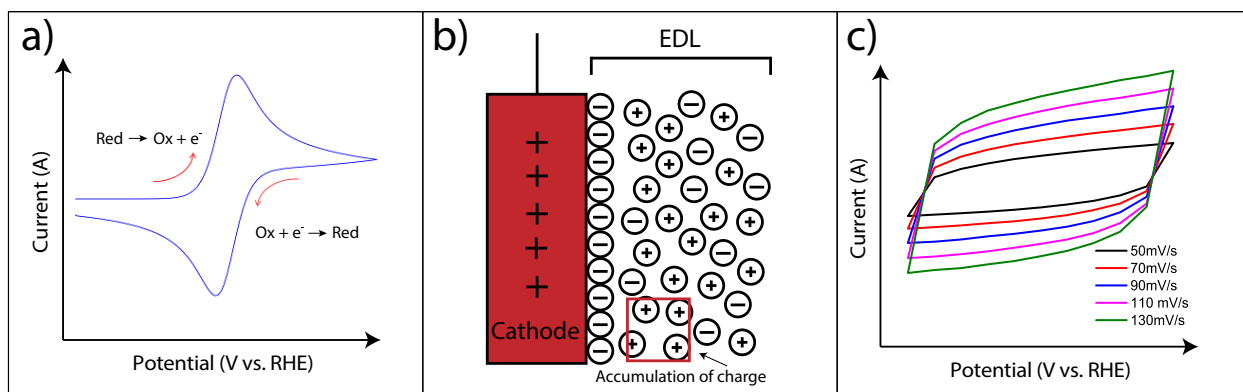


Figure 6: a) A simple voltammogram of a reversible redox reaction, (b) schematic figure illustrating the electrical double layer (EDL) and its capability to store charge and (c) CV's recorded at different scan rates in a non-faradaic region for double capacitance determination.

1.1.6 Chronoamperometry and faradaic efficiency

Faradaic efficiency (FE) describes the efficiency of transferred electrons by a chemical reactions. To generate a quantifiable amount of reaction products a constant current is applied. By chronoamperometry the current at the working electrode can be monitored at the chosen potential as a function of time. Fluctuations in current provide information about the stability of the electrode. For example, a decreasing current for nanoparticle electrodes usually entails a decreasing surface area. A increase in current could be caused by deposition of material on the electrode or roughening of the surface increasing its surface area. A suitable applied potential for the CO₂RR on a general Cu electrode is usually a reducing potential between -0.6 to -1.2 V vs. RHE depending on the desired product as can be seen in figure 7.

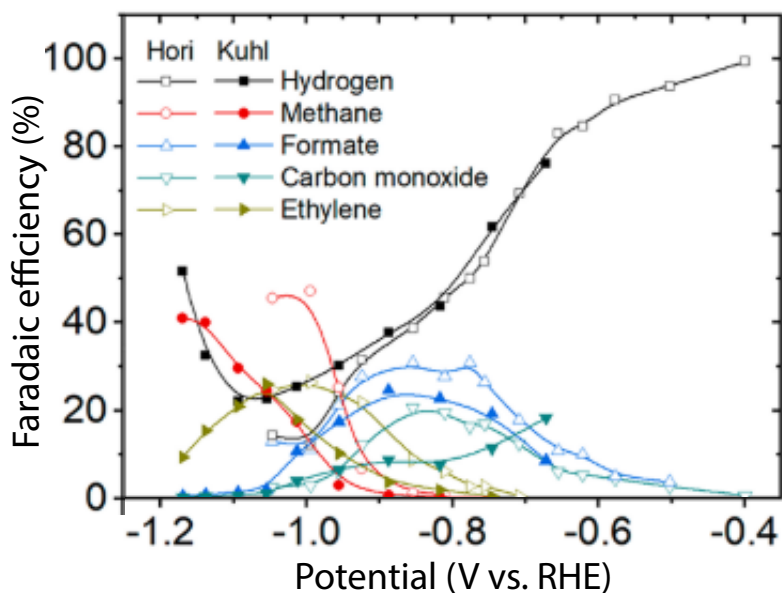


Figure 7: Faradaic efficiency of common reaction products of a general Cu electrode from the CO₂RR at various applied potentials. Figure adapted from Ref [35].

The calculation of the faradaic efficiency for a reaction such as the CO₂RR requires the quantification of produced products. An explanation will be given for the calculation of the faradaic efficiency from the ppm of the quantified products. Once the products have been detected and converted to ppm by gas chromatography from their peak area (with the use of calibration gas), the Faradaic efficiency can be calculated using equation 2. The calculation follows from the amount of electrons that end up in a certain reaction product divided by the total amount of electrons that have been involved in the overall reaction.

$$\text{Faradaic efficiency} = \frac{\text{ppm} \times n \times \text{flowrate} \times F}{RTI} \quad (2)$$

In equation 2, n stands for the amount of electrons transferred for a specific reaction product according to their respective half reaction (see table 1), the flow rate of the supplied CO₂ and I , the partial current in A, measured by the chronoamperometry.

1.2 CO₂ reduction Mechanism

1.2.1 CO₂ adsorption and reaction pathways

The wide variety of obtainable products during the CO₂RR on Cu is linked to a complex reaction mechanism. Starting with the first step, the adsorption of CO₂ on a Cu surface electrode. Multiple possible ways for the adsorption of CO₂ have been proposed, determining the following reaction steps that ultimately result in specific reaction products.^{5,18,25-34}

The two major reaction pathways that are mostly agreed upon are the formate and the carbon monoxide pathway, that follow from the second reaction step after adsorption of CO₂ as can be seen in figure 8. Either CO₂ adsorbs by a concerted proton-electron transfer (CPET) or by a decoupled pathway through a charged intermediate.²⁸ Most proposed mechanisms accept that only from the CO reaction pathway, C₂ products follow as a result of C-C coupling and hydrogenation reactions in addition to the C₁ product methane. These products require however, that the CO molecule remains adsorbed on the Cu electrodes surface for following reactions to have a chance of occurring, instead of desorption into gaseous CO.

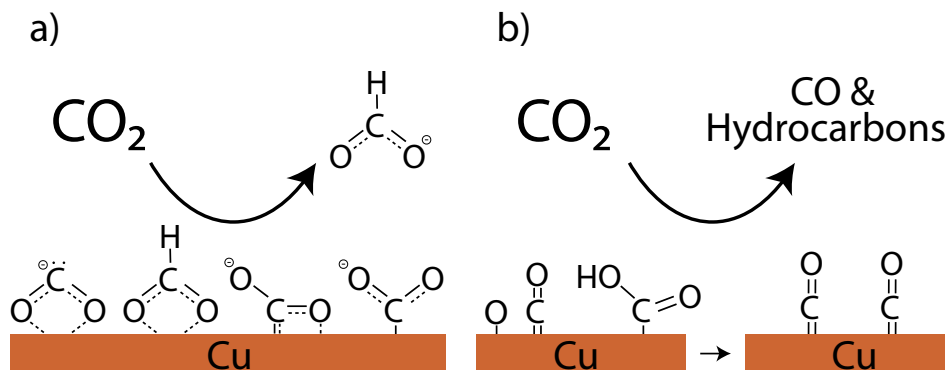


Figure 8: Illustration of the proposed intermediates for the adsorption of CO₂ on the surface of a Cu electrode resulting in either (a) the formate or (b) the CO reaction pathway. Figure adapted from ref [35].

1.2.2 Rate-determining steps

For any chemical process, the rate of the overall reaction is determined by the slowest step, known as the rate-determining step or rate-limiting step. The job of a catalyst is to make the intermediate following this step more easily accessible, thereby increasing the reaction rate of the overall reaction drastically. Most proposed mechanisms of the CO₂RR agree that for the two electron transfer products formate and CO, the rate limiting step is the CO₂ adsorption onto the Cu surface. For C₁ formation the limiting step has been thought to be surface adsorbed CO protonation either through a *COH or *CHO intermediate (fig 9a).^{18-20,46-48} For C₂₊ product formation however, the limiting step has generally been thought to be CO dimerization that is decoupled from proton transfer (fig 9b).^{19,22,49-52}

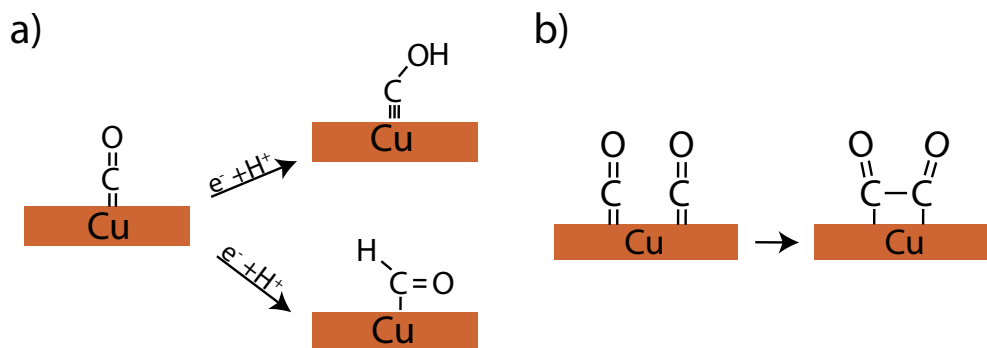


Figure 9: Illustrations of (a) the rate determining step for C_1 products and (b) the rate determining step for C_{2+} products.

1.2.3 Copper bimetallic electrodes

Bimetallic electrodes makes use of the selectivity of an element from a different product group to increase the amount of surface adsorbed species that can aid in the CO_2RR as intermediates for certain reaction steps. Metals from the CO group (Ag, Au, and Pd) have been reported to possess synergistic effects that enhance the activity or selectivity for C_1 and C_2 products.⁵³⁻⁵⁷ These effects consist of CO spillover and electronic effects. In the case of CO spillover, hotspots of CO producing active sites form CO group metals are incorporated in a Cu electrode for an additional supply of CO at the surface. The idea of CO spillover, is that these additional CO can be adsorbed on Cu via eased surface diffusion over short length scales and/or by increasing the concentration within the diffusion boundary layer, which leads to a higher coverage of surface adsorbed CO on Cu active sites. An illustration of the CO spillover effect is shown in figure 10. The electronic effects refer to a change in the electronic structure of the host material after addition of another element, which alters the binding strength of intermediate adsorbates on the surface.^{58,59} the increased observed selectivity for (oxygenated) C_2 products, could indicate that bimetallic electrodes can aid in the rate limiting step of CO dimerization.

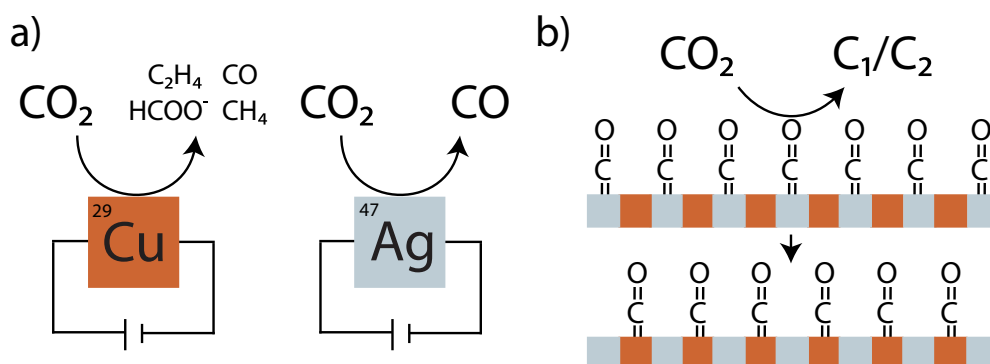


Figure 10: a) Illustration of the different selectivity groups with Cu for the hydrocarbon group and Ag for the CO group and (b) illustration of CO spillover promoting the CO pathway with a Cu/Ag bimetallic electrode.

1.3 Crystal structure

1.3.1 Structure-Function

For catalysis, the planes at the surface of crystalline material are of particular interest. At the surface of a crystal a wide range of different planes can be present and for chemical reactions such as the CO₂RR on Cu, these planes have a profound effect on the selectivity of the reaction mechanism. Important facets for the CO₂RR include the methane selective facet Cu(111) and the ethylene selective facet Cu(100). Certain intermediate reaction steps are promoted on these specific planes, therefore the structure is closely related to the reaction mechanism. With a good understanding of the crystal and surface structure, the relationship between structure and function can be unravelled.

1.3.2 Unit cell

When crystalline, solid metals possess over a certain crystal structure built up from regularly repeating structural motives of bonding atoms. To characterise these structures, the pattern of the bonding atoms is usually described as a space lattice. A space lattice defines the basic structure of the crystal by a three-dimensional infinite array of points, of which each point is surrounded in an identical way by its neighbours. The crystal structure can be obtained by associating a identical structural motive centred on each of these lattice points. The entire space lattice can be subdivided into specific unit cells, shapes constructed from straight lines through lattice points. A certain space lattice can be described by an infinite amount of different unit cells. To narrow it down to a specific unit cell, the unit cell which has the smallest dimensions that accurately describes the whole crystal by repeating itself, is the true unit cell. The position of the lattice points is how unit cells can be characterised. A unit cell is called primitive (P) when all its lattice points are only at the corners. If the unit cell has a lattice point at its center in addition to the corners it is a body-centered unit cell (I). For unit cells with lattice points at the corners and in the middle of their six faces it is a face-centered unit cell (F). The metals Cu and Ag possess over a face-centered cubic structure (fig 11).

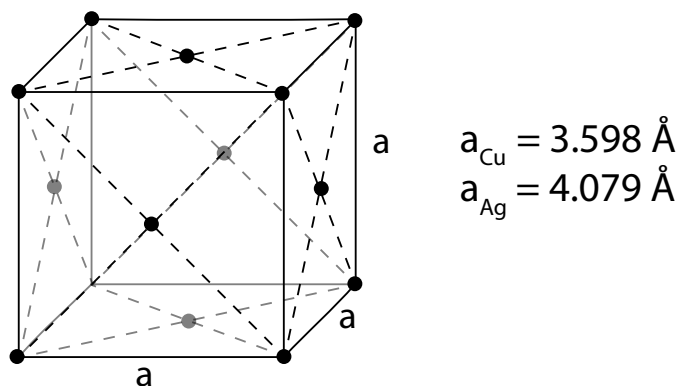


Figure 11: Illustration of the face-centered cubic (FCC) structure with the average lattice parameter (a) of Cu and Ag in angstrom.⁶⁰

1.3.3 Miller index notation

To be able to differentiate between all the possible crystal planes at the surface of a crystalline material, the miller index notation is used. The miller index notation uses three miller indices, (hkl) , where h , k , l are the reciprocals of distances at which intersection of the plane occurs with the x, y and z axes respectively of a cubic unit cell. However, when a plane is parallel to the respective axis, they are said to intersect each other at an infinite distance. To avoid labels with infinities and fractions, the reciprocal value is used, an infinite distance therefore becomes a indices of 0. The important surface planes for the CO₂R on Cu, Cu(111) and Cu(100), are represented in figure 12.

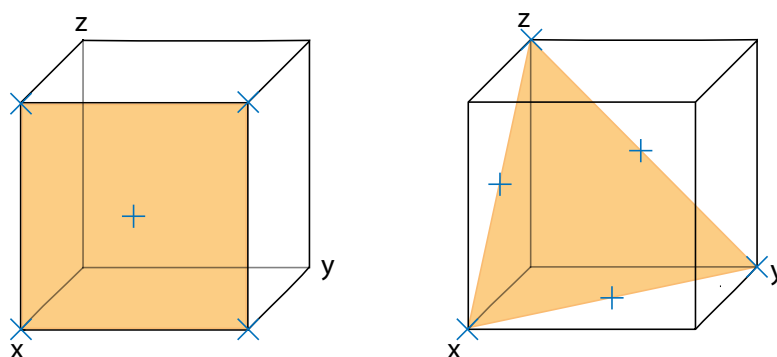


Figure 12: Illustrations of the (100) and (111) plane respectively.

A ball model can be used to interpret how these planes look like. The Cu(100) and Cu(111) facets of FCC Cu are shown in figure 13. As can be seen from the figure, the Cu(100) FCC plane is a cubic packed plane with cubic symmetry and the Cu(111) FCC plane is a closed packed plane with hexagonal symmetry.

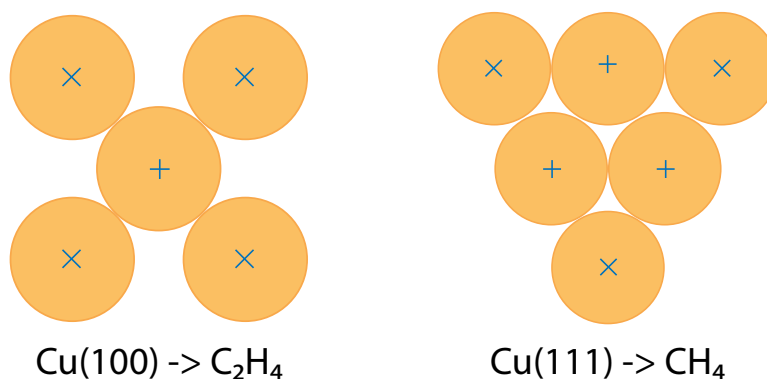


Figure 13: Ball model of the ethylene selective Cu(100) and the methane selective Cu(111) plane of FCC Cu.

1.3.4 X-ray diffraction techniques

A important characterisation technique for the crystal structure of solid materials is X-ray diffraction. When an X-ray passes through a material it will diffract when the wavelength of the X-ray is scattered by the regular array of atoms in a crystal. For most of the diffracted waves they will cancel each other out due to destructive interference, however for a few specific directions constructive interference will occur. Constructive interference will occur when the glancing angle (2θ) satisfies the Bragg's law in equation 3.

$$n\lambda = 2d\sin\theta \quad (3)$$

the n stands for the order of reflections which must be a positive integer, λ is the wavelength of the X-ray beam and d is the distance between planes of atoms also referred to as d-spacing. Each peak in a diffractogram results from a corresponding d-spacing, which relates to a Miller indices by the equation: $1/d^2 = (h^2 + k^2 + l^2)/a^2$, where a is the lattice parameter.

When measuring XRD in Bragg-Brentano mode, the crystal is usually scanned with a glancing angle at any range between 20 to 120° . For thin samples however, one might prefer to measure XRD in the grazing incidence mode. Unlike when measuring with Bragg-Brentano mode the X-ray source is not moved from its original position while maintaining a "grazing" angle, minimizing the penetration depth of the X-rays into the sample increases the diffraction contribution of the thin film. A comparison of Bragg-Brentano and grazing incidence mode is shown in figure 14.

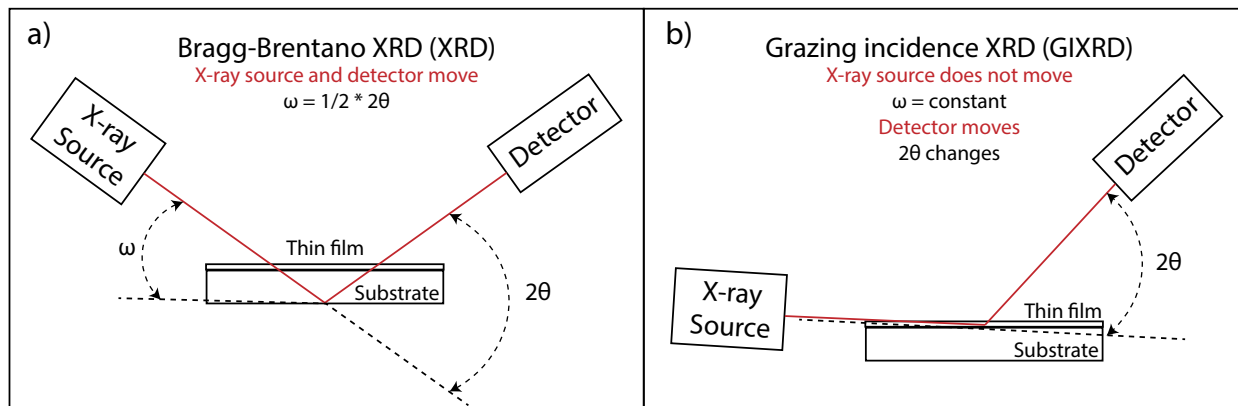


Figure 14: Illustrations of (a) XRD measured in Bragg-Brentano mode and (b) XRD measured in grazing incidence mode.

1.3.5 Electron crystallography

Other than providing a magnified image of the sample, the electron beam from a transmission electron microscope (TEM) can also be used for the determination of the crystal structure of solids by electron diffraction (ED). The periodic structure of a crystalline sample acts as a diffraction grating causing electrons to form a diffraction pattern in the back focal plane of the electron microscope which can be imaged by a CCD camera. The generated diffraction pattern corresponds to the entire illuminated area. To look at specific spot, a selected area electron diffraction (SAED) aperture can be used. The resulting diffraction pattern can consist of ring patterns in the case of polycrystalline samples or sharp spots indicating single crystal diffraction. The position of the rings or spots with respect to the central beam is related to a certain miller indices plane similar to the glancing angle in XRD. From ED, information can be obtained about the samples crystallinity, including the respective lattice parameters and symmetry, grain morphology, grain size distribution or grain orientation.

1.3.6 Diffraction patterns and unit cells

From diffraction patterns obtained by either XRD or ED information can be obtained about the ordering of the unit cell by examining the Miller indices. For cubic systems, certain rules apply from which the type of unit cell can be derived. For example, the value of the square of the hkl values of the first observed reflection in a diffraction pattern is related to the type of unit cell. If the first reflection is (100), $h^2 + k^2 + l^2 = 1$ the unit cell is simple cubic. If the first reflection is (110), $h^2 + k^2 + l^2 = 2$ the unit cell is body centered cubic and lastly if the first reflection is (111), $h^2 + k^2 + l^2 = 3$ the unit cell is face-centered cubic. Furthermore from the characteristics of reflections that occur, the type of unit cell can also be deduced according to the following conditions: the unit cell is allowed to be primitive for possible reflections with all values for h , k , and l . The unit cell is allowed to be body-centered when $(h + k + l)$ of all reflections is even, and not allowed when $(h + k + l)$ of any reflection is odd. The unit cell is allowed to be face-centered when the hkl values of all the observed reflections are either all even or all odd with 0 being an even value.

1.4 Metal nanoparticle colloidal synthesis

1.4.1 Colloidal synthesis

A highly controllable synthesis method is required to ensure nanoparticles that are dominant in the hydrocarbon selective surface facets Cu(100) or Cu(111). For this reason a colloidal synthesis method is preferred. Colloidal synthesis, like many approaches for nanoparticle synthesis, is performed in a bottom up manner from a solution of monomers. By stacking of said monomers by precipitation, nuclei are formed that grow into nanocrystals. This event was first described by LaMer, who published his model explaining the nucleation event in 1950 and is currently used as the basis for every colloidal synthesis approach. The model can be seen in figure 15.^{61,62}

1.4.2 Heat-up synthesis

The heat-up method is a colloidal approach based on thermal decomposition of metal salt precursors in the presence of a reducing agent and ligands in an organic solution. As a prerequisite for the heat-up synthesis, the nucleation rate must be highly temperature sensitive and steadily increased to an appropriate maximum as the solution is heated to the desired growth temperature.⁶³ The synthesis can be subdivided into four key parts that follow from LaMer's model: monomer formation, nucleation, growth and equilibrium.

I: Monomer formation. The synthesis is started by gradual heating of a reaction vessel containing all precursors, beginning at room temperature. It is required that the chosen precursors are stable, to enforce this the synthesis can be performed in an inert atmosphere such as N₂ or Ar. Once the reaction vessel has been sufficiently heated, the metal precursor will be reduced and monomers are formed. This stage is concluded once the concentration of the solution is increased beyond its saturated concentration (C_s) causing the solution to be supersaturated (C_{min*}).

II: Nucleation. Once the solution is supersaturated at the critical temperature, nucleation is initiated. The nuclei concentration increases drastically and moderate growth of the nuclei occurs. In this phase the level of supersaturation reaches its critical limit and the monomer concentration reaches its maximum (C_{max}). The decrease of which in time occurs as a result of the much higher nucleation rate with respect to monomer formation due to depletion of precursors. At this point the particle size distribution (PSD) is maximal due to the disparity between the size of growing nuclei and the formation of new smaller nuclei.

III: Growth. This stage is defined by a decline in nucleation rate. The supersaturation starts to decrease below its critical value as monomers are rapidly consumed for the growth of existing nuclei. Nucleation can still occur, however the nuclei will redissolve back into monomers to feed the existing particles with monomers ensuring growth by diffusion. This results in self-sharpening of the PSD.

IV: Equilibrium In this stage the depletion of the remaining precursors is realised and the nanocrystal concentration, size and distribution is considered constant. At this point the reaction would typically be cooled and the nanocrystals isolated and washed.

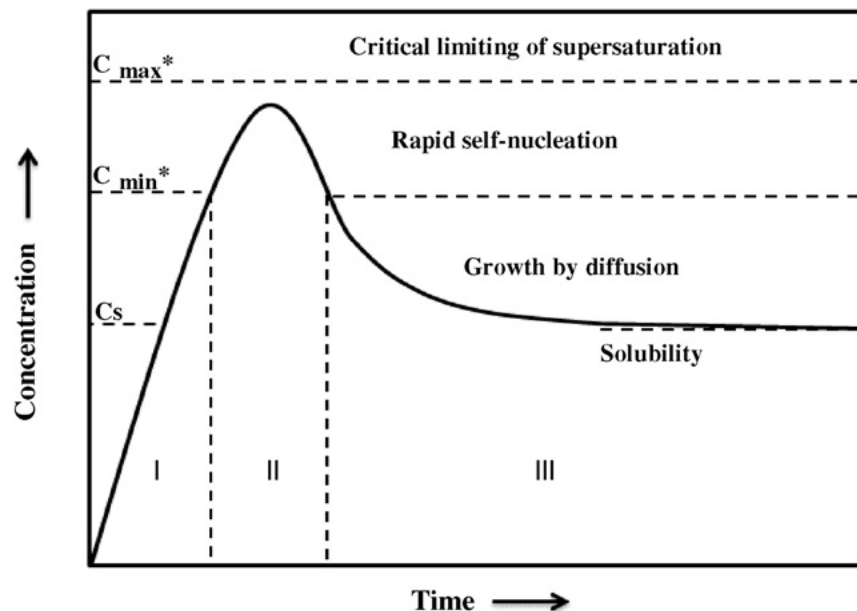


Figure 15: LaMer's model for nucleation of a precipitation reaction as a function of monomer concentration over time.

An other important factor to ensure a successful and repeatable heat-up synthesis includes the heating rate at which the synthesis is performed.⁶⁴ For example, when a slow heating rate is used, the rate of precursor conversion to monomer will be low. At this rate, the onset of nucleation will be delayed. The delay in nucleation causes the first formed nuclei to grow by a monomer consumption at a rate much higher than the precursor conversion rate resulting in a fast decrease in supersaturation quenching the nucleation phase. Ultimately causing very few nuclei to be formed which grow in relatively large nanocrystals with a wide PSD.⁶⁵ However, when a high heating rate is used, monomers are produced at a much faster rate than existing nuclei can grow. At this rate, monomers will be solely used for the formation of new nuclei, resulting in much higher concentrations of nanocrystals with smaller size and a much more narrow PSD.⁶⁶

1.4.3 Classical nucleation theory

Classical nucleation theory (CNT) describes the phase transition of monomer to nuclei based on thermodynamic relationships, providing valuable insight in reaction kinetics for the synthesis of nanocrystals. To achieve nucleation, the Gibbs energy gained from making a bulk phase must overcome the Gibbs energy required to form a surface.⁶⁷ Surface atoms are not fully coordinated resulting in ‘dangling bonds’ creating a high energy interface. Atoms in a bulk phase however are fully coordinated and therefore favourable in terms of Gibbs energy. Therefore, bulk formation is the driving force for nucleation.

$$\Delta G = \Delta G(\text{surface}) - \Delta G(\text{bulk}) \quad (4)$$

For homogeneous nucleation of a spherical nuclei, the bulk contribution in equation 4 can be described as $\Delta G(\text{bulk}) = (4\pi r^3/3)/\Delta G_V$ where ΔG_V is the Gibbs free energy per unit volume which can be expressed as $\Delta G_V = -(RT/V_M)\ln S$, where R is the gas constant, T is the temperature V_M is the molar volume of the monomer and S is the level of supersaturation.^{63,67} The surface term can be described as $\Delta G(\text{surface}) = 4\pi r^2\gamma$ where γ is the surface energy. Substitution of both terms results in the total equation for nuclei formation.

$$\Delta G = -\frac{4\pi r^3 RT \ln S}{3V_M} + 4\pi r^2 \gamma \quad (5)$$

Equation 5 has a maximum when expressed as a function of nuclei radius r. From this equation the critical value ΔG^* can be calculated by $d\Delta G/dr = 0$ resulting in equation 6.

$$\Delta G^* = \frac{16\pi\gamma^3 V_M^2}{3R^2 T^2 (\ln S)^2} \quad (6)$$

Equation 6 represents a thermodynamic barrier, the energy required to form a stable nuclei. This critical value for Gibbs energy is an important factor for the rate at which nucleation occurs. The corresponding radius at this maximum is known as the critical radius, r_C shown in equation 7.

$$r_C = \frac{2\gamma V_M}{RT \ln S} \quad (7)$$

As a system is always in favour of lowering its total free energy, nuclei with $r > r_C$ will reduce their ΔG by growth increasing their bulk phase once the nucleation phase has ended. Nuclei with $r < r_C$ will reduce their ΔG by eliminating their surface by redissolving back into monomers. Equation 6 and 7 highlight the importance of parameters such as: the supersaturation S controlled by the reactivity of the precursors, the temperature of the solution T and the surface energy γ controlled by the presence of coordinating ligands for the synthesis of nanocrystals.

1.4.4 Interactions between metals and ligands

Possibly the most important feature of any colloidal synthesis approach are the ligands that provide the stability of the formed nanocrystals. Most ligands possess a polar head group, capable of coordinating to the surface atoms of a nanocrystal and a long hydrophobic carbon tail which acts as a protective barrier preventing aggregation when fully covering the nanocrystal (fig 16b).

How ligands interact with metal precursors in solution and the resultant effect on nanocrystal formation can be understood from hard and soft acid base (HSAB) theory. The affinity between metal centres (Lewis acids) and coordinating ligands (Lewis bases) will be higher if they share similar “hard” or “soft” properties. Specifically, a hard ligand will associate more strongly than a soft ligand to a hard metal, and *vice versa*.⁶⁸ The hard and soft character of a number of metals and ligands typically used in the heat-up synthesis is shown in figure 16a. An acid or base can be defined as hard if it is weakly polarizable. This is usually the case for atoms with small atomic radii and a high oxidation state. Whereas soft acid and bases are typically highly polarizable due to their large atomic radii and low oxidation states. Bonding of hard/hard metal ligand pairs is considered ionic in nature, and soft/soft pairs have a more covalent character of binding. The strength of interaction between competing ligands and metal precursors can have profound effects on both nucleation and growth stages of nanocrystal formation. Weak monomer ligand bonding stimulates fast nucleation by a low affinity for coordination increasing the amount of available monomers. However, to ensure a controlled growth phase strong monomer ligand bonding is required to prevent uncontrolled growth into bulk phase. That is why for most heat-up synthesis methods, more than one ligand is used to gain control over the reaction kinetics.

Furthermore, ligands can be used to stimulate growth of a certain facet resulting in specific shapes of the nanocrystal. This property can be attributed to the preferential coordination of a ligand to a specific facet of the nano crystal. This adds additional complexity when trying to predict metal-ligand affinities.

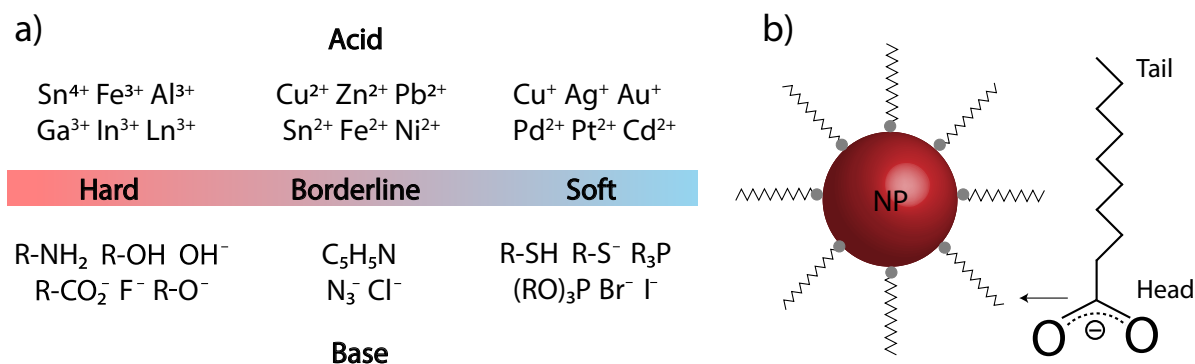


Figure 16: a) Hard and soft classification of various acid and bases frequently used in the heat-up synthesis of nanocrystals and (b) a nanoparticle covered by ligands with a carboxylic acid functional group.

1.4.5 Localised surface plasmon resonance

A unique feature of metal nanoparticles, is the excitation of their surface plasmons by a resonant radiation source. Meaning that the conduction band electrons at the nanoparticles surface start to coherently oscillate. The frequency at which this oscillation occurs depends on the density of electrons, the effective electron mass, and the size and shape of the charge distribution.⁶⁹ The excitation of surface plasmons corresponds to the nanoparticles optical absorption maximum at the plasmon resonance frequency. For noble metal nanoparticles prepared by wet chemistry, this resonance occurs at visible wavelength which gives rise to vivid colours. As the resonance frequency is tunable by size and shape, a spectrum of colours can be achieved by changing the dimensions of the noble metal nanoparticle as shown in figure 17. Therefore, by measuring the absorbance spectrum of the metal nanoparticle solution, some information can be obtained about the size, shape and PSD. A collection of nanoparticles similar in size, have similar resonance frequencies resulting in a narrow absorption maximum. Information obtained from such a spectrum is therefore highly useful when optimizing synthesis strategies.

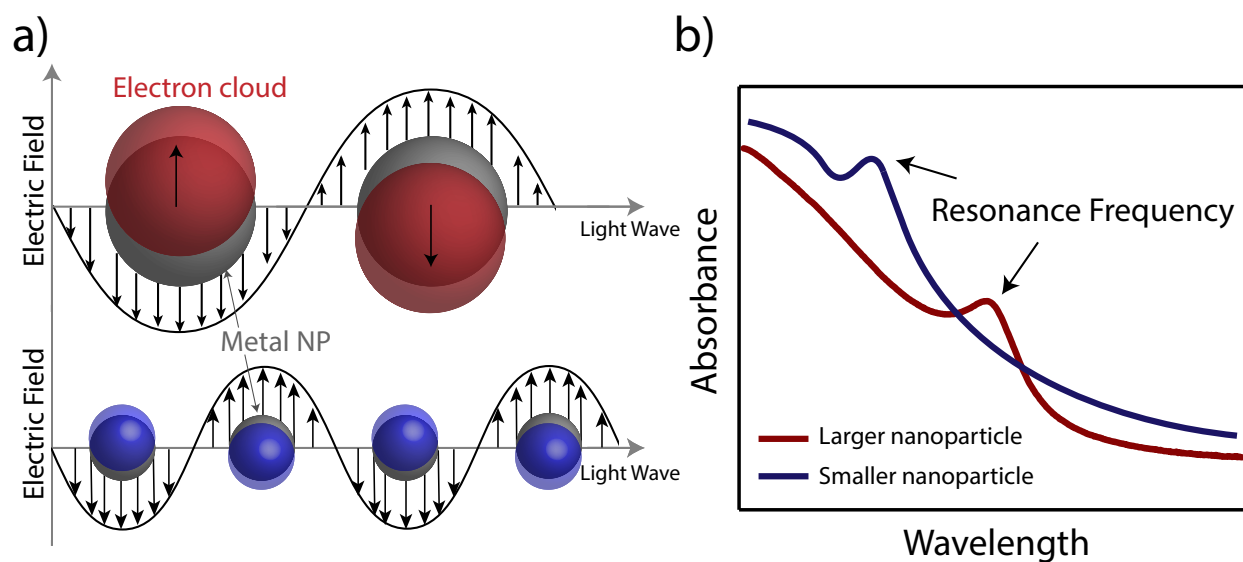


Figure 17: a) Illustration of the localised surface plasmon resonance effect on different sized nanoparticles as the result of absorbed light with their (b) respective resonance frequency.

1.5 Characterisation and element quantification

1.5.1 Electron microscopy

When working with materials in the nanoscale range, characterisation techniques are required with a sufficient resolution to provide any useful information. To determine the shape and size of nanoparticles by imaging, the only viable option is electron microscopy. The illumination source of such a microscope is a dense beam of electrons produced by an electron gun. By using an electron beam as illumination source, resolutions much higher than that of the diffraction limited optical microscope is able to be achieved. The electrons of an electron microscope, are accelerated within a range of 1 to 400 keV. When these electrons hit the sample, many different events shown in figure 18 can occur. A variety of electron microscopy techniques are based of these events.

To create a highly magnified image of a sample, one could use the transmission, secondary or backscattered electrons. In transmission electron microscopy (TEM) a wide, homogeneous and parallel electron beam is directed onto the sample. Areas of the sample can absorb or scatter the electrons of the electron beam. The extend to which this occurs depends on the thickness and orientation of a crystalline sample with respect to the electron beam. These events give rise to mass-thickness and diffraction contrast. The transmitted electrons are collected and used to project a highly magnified image, by electron optics, of the sample. In the scanning mode (STEM), the electron beam is focused into a fine spot. Such a spot is referred to as an electron probe, which is raster scanned over the sample. The benefit of the scanning mode is the increased resolution, however as the probe is raster scanned over the sample, the measurement time is longer and beam damage becomes more probable. Lastly, a second scanning microscopy technique that uses the secondary electrons and backscattered electrons of the sample is scanning electron microscopy (SEM). The main difference between SEM with respect to TEM is that the secondary electrons provide a three-dimensional image of the surface, and allows for a much larger maximum field of view, however at the cost of lower magnification.

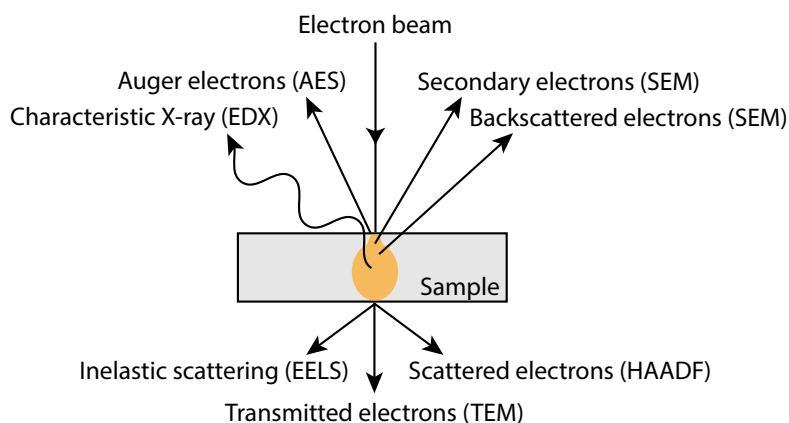


Figure 18: Schematic representation of all the possible events that can occur upon exposure of a sample to a high intensity electron beam.

1.5.2 High angle annular dark field imaging

The scanning mode of TEM and SEM allows for a range of analytical techniques to be used in accordance such as Z-contrast or high angle annular dark-field imaging (HAADF), and spectroscopic techniques such as energy dispersive X-ray (EDX) spectroscopy or electron energy loss spectroscopy (EELS). When performing a STEM-HAADF measurement, a ring shaped detector collects the electrons that have scattered at a certain angle underneath the sample. Depending on the heaviness of the atoms of the sample indicated by the atomic mass (Z), the scattering angle can either be large (for high Z value atoms) or low (for low Z value atoms). By varying the angle of the edges of the ring shaped director, Z contrast can be obtained and applied in imaging.

1.5.3 Energy-dispersive X-ray spectroscopy

Besides the scattering of the incident electron beam, the electrons of the beam can also cause holes in the core shell of the atoms of the sample resulting in the emission of characteristic X-rays upon recombination by electrons of the outer shells (fig 19). At rest, the electrons of the atoms within the sample are in the ground state in discrete energy levels. When exposed to an incident electron beam, electrons that reside in the inner shell of the atom may be ejected, leaving a hole behind. An electron from a higher energy outer shell then fills the electron hole. Recombination of the electron hole causes the emission of a X-ray photon, of which the energy is in accordance with the energy difference between the inner and the outer shell. With the scanning transmission mode of an electron microscope, an electron probe can be used to generate an X-ray spectrum at every pixel of the image. As the emitted X-rays of the sample are specific for each element, these pixels can be used to create a chemical map made of all atom species of the sample.

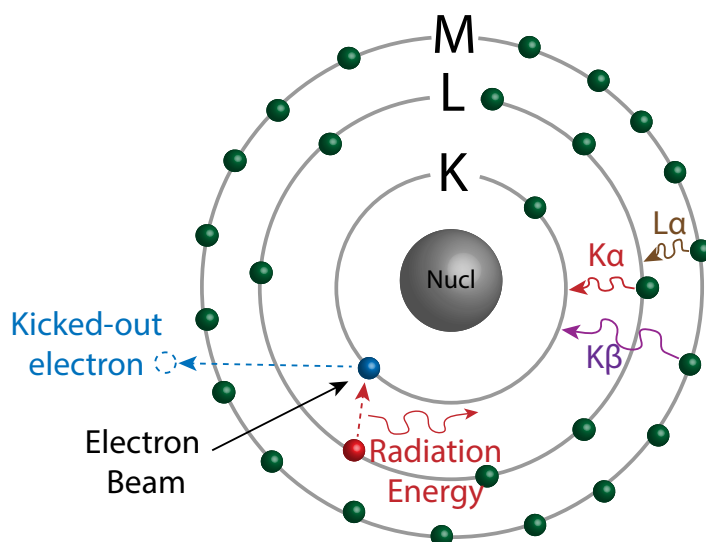


Figure 19: Illustration of a kicked out electron by a electron beam source resulting in the characteristic radiation of X-rays by recombination of the electron holes by electrons from higher energy shells.

1.5.4 Inductively coupled plasma atomic optical emission spectrometry

An other powerful tool to analyse and quantitatively deduce the amount and type of elemental species in a sample is by inductively coupled plasma atomic optical emission spectrometry (ICP-OES). In ICP-OES, a sample is exposed to an inductively coupled plasma, producing excited atoms and ions which emit characteristic electromagnetic radiation for a certain element. With the use of a calibration curve of which the concentration of a certain element is known, the measured emission intensity of a sample can be quantified to a concentration. The main advantage of ICP-OES is its unmatched detection limit of parts per billion levels and high accuracy. A disadvantage of ICP-OES is that it is a destructive method, a piece of sample is sacrificed as the measurement requires the sample to be completely dissolved. This also means that the obtained results give no information about the spatial distribution of elements unlike EDX mapping.

1.5.5 X-ray photoelectron spectroscopy

Specifically for the characterisation of surface species including element and oxidation state, X-ray photoelectron spectroscopy (XPS) is a powerful spectroscopic technique. XPS is based on the photoelectric effect, the stimulated emission of electrons from a material by electromagnetic radiation. When such an electron is ejected from the host material, it is called a photoelectron. A detector collects the ejected photoelectrons and calculates its kinetic energy. From the photoelectric effect equation the electron binding energy of the emitted photoelectron can be calculated which is element and oxidation state specific.

$$E_{\text{binding}} = E_{\text{photon}} - (E_{\text{kinetic}} + \phi) \quad (8)$$

In this equation the E_{photon} is the energy of the X-ray photons of the radiation source, E_{kinetic} is the kinetic energy of the ejected photoelectron and ϕ is the work function, which is specific for the material. The binding energies, E_{binding} , correspond to a specific electron configuration within the atoms, 1s, 2s, 2p, 3s etc, which is plotted in a typical XPS spectrum as a function of intensity. This spectroscopic technique is highly specific for surface atoms, as the ejected photoelectrons must reach the detector, of which is only realistic for the first ten layers of atoms of a material. For the bulk atoms, the ejected photoelectrons are more likely to be recaptured or trapped in various excited states within the material.

1.5.6 Vibrational spectroscopy

The most important tool to experimentally determine the type of organic species on the surface of an electrode during the CO₂RR is *in situ* vibrational spectroscopy. More specifically, Raman spectroscopy and various forms of infrared (IR) spectroscopy. When used during the CO₂RR, the type of vibrations that occur at the electrodes surface can studied. Depending on the wavenumber, intensity, order and applied potential at which said vibration occurs, insight can be gained in the reaction mechanism. Both techniques make use of an incident radiation source to probe vibrational modes, however the way in which differs from each other. In Raman spectroscopy, incident photons are scattered from a sample molecule. The frequencies of these scattered photons are analysed to determine the changes in molecular states that accompany the scattering process. In infrared spectroscopy the incident photons of a infrared radiation source are not scattered but absorbed. The frequency of absorbed radiation matches the vibrational frequency of a certain vibrational mode of the molecule. Whether a molecule can be observed by either vibrational spectroscopy technique depends on whether the induced vibrational mode causes a change in polarizability for Raman or if the vibrational mode induces a change in the molecules dipole moment. For some vibrations these criteria are not satisfied for both techniques, therefore Raman and IR spectroscopy complement each other.

2 Nanoparticle synthesis and characterisation

In this chapter of the thesis, the focus is put on the synthesis and characterisation of the copper and silver nanoparticles. First the synthesis procedure is described followed by the used characterisation techniques and lastly, the optimization of the synthesis, the crystal structure and the surface species of the Cu and Ag nanoparticles are discussed.

2.1 Experimental methods and materials

2.1.1 Chemicals

All chemicals were used as received from their supplier without further purification. Chemicals sensitive to oxidation were stored in a glovebox with an inert N₂ atmosphere. Anhydrous hexane, anhydrous ethanol, 1-tetradecylphosphonic acid (98%), tri-n-octylamine (95%) and Oleic acid (90%) were purchased from Alfa Aesar. Anhydrous ethanol, n-hexane (99+%), copper(I)acetate (97%), silver nitrate (99%) and 1-octadecene (90%) were purchased from Sigma Aldrich.

2.1.2 Cu nanoparticle synthesis

Copper nanoparticles were prepared by the thermal decomposition of copper(I)acetate (CuOAc) with the reducing agent tri-n-octylamine (TOA) in the presence of the surfactants tetradecylphosphonic acid (TDPA) and Oleic acid. The following description is of the final optimised synthesis procedure, which is an adaptation of a reported method (Appendix).²³ To a 100 ml three neck flask, 123 mg of CuOAc and 139 mg of TDPA was added. The flask was then attached to a schlenk line by a condenser. Subsequently, 10 ml of 1-octadecene, 10 ml of TOA and 0.7 ml of oleic acid was added to the flask. For temperature control, a halfway filled glass tube filled with 1-octadecene and a thermocouple was attached to the three neck flask. The flask was heated at 100 °C while vigorously stirring for an hour, after vacuum was applied to ensure the evaporation of solvent impurities. The following step was rapid heating of the solution to 180 °C once a N₂ flow was applied while maintaining a high stirring rate. This temperature was maintained for 30 minutes after which the solution was further heated to 220 °C for another 30 minutes. The resulting red colloidal solution was cooled to room temperature. The colloidal solution was extracted and subsequently washed by a 1 to 1 ratio of reaction solution and anhydrous ethanol by centrifuging for 5 minutes at 3000 rpm. After the removal of the supernatant, a solid pellet of nanoparticles remained which was redispersed in n-hexane and stored in a glovebox. A schematic representation of the synthesis is illustrated in figure 20.

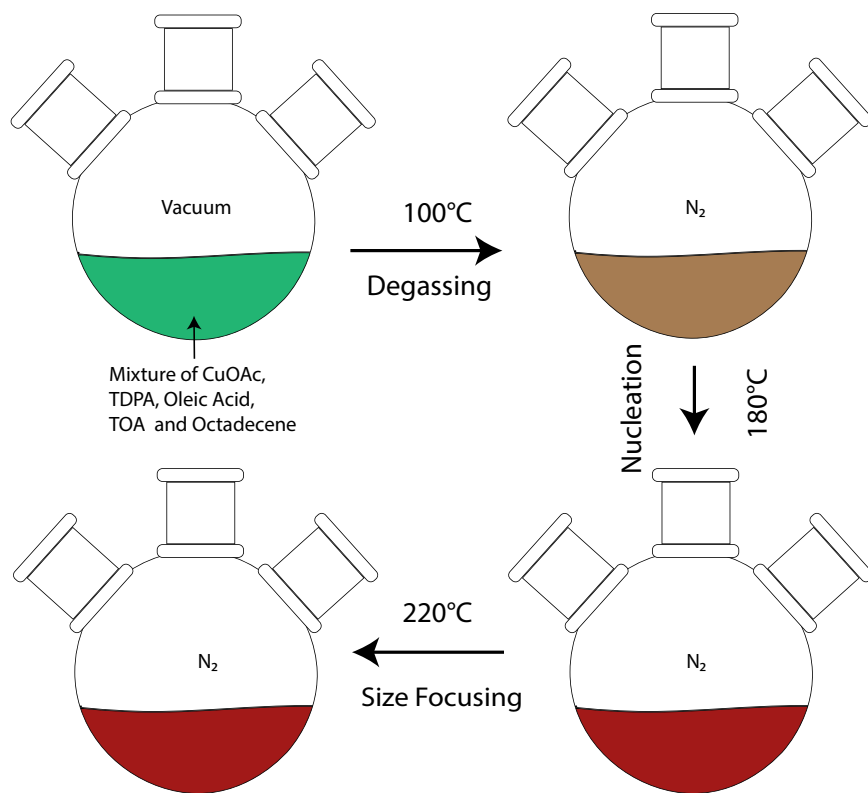


Figure 20: Schematic representation of the colloidal Cu nanoparticle synthesis.

2.1.3 Ag nanoparticle synthesis

The silver nanoparticle synthesis procedure was an adaptation of the optimised copper nanoparticle synthesis as mentioned above. The slight difference in the following procedure are to account for the increased reactivity of the strong oxidizing character of silver nitrate. The silver nanoparticles were prepared by the thermal decomposition of silver nitrate (AgNO_3) in the reducing agent tri-n-octylamine (TOA) in the presence of the surfactants tetradecylphosphonic acid (TDPA) and Oleic acid. The same synthesis set-up as for the optimised copper nanoparticle synthesis was used. To the three neck flask, 170 mg of AgNO_3 and 278 mg of TDPA were added together with 20 ml of 1-octadecene, 1.0 ml of TOA and 0.7 ml of oleic acid. The solution was put under vacuum for one hour at room temperature. After which, a N_2 atmosphere was applied and the solution was rapidly heated to 100 °C and maintained at this temperature for half an hour. Subsequently, the solution was further heated to 120 °C for another 30 minutes. The resulting yellow colloidal solution was extracted and washed with the same method as for the copper nanoparticle procedure. After the extraction and re-dispersion of the Ag nanoparticles in hexane, the colloidal solution was stored in a glovebox. A schematic representation of the synthesis is illustrated in figure 21.

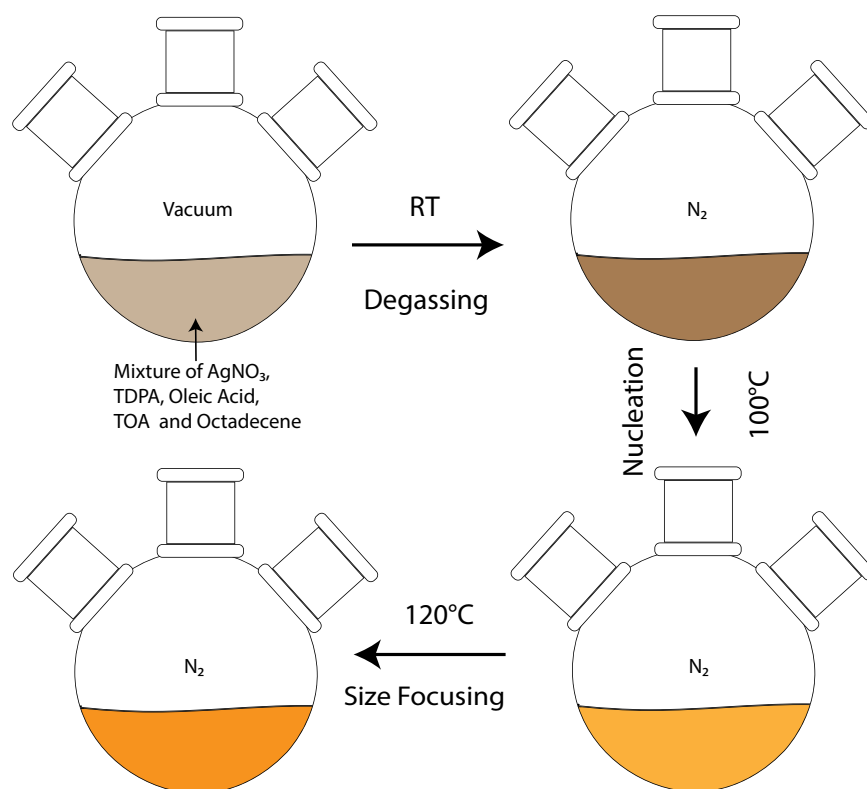


Figure 21: Schematic representation of the colloidal Ag nanoparticle synthesis.

2.2 Characterization techniques

2.2.1 UV/Vis-spectroscopy

UV-VIS measurements were performed in a Cary 60 UV-Vis Spectrophotometer with a Xenon source lamp. Samples were measured in Helma Quartz Glass seal-able cuvettes, spectral range 200-2500 nm.

2.2.2 Transmission electron microscopy and electron diffraction

TEM samples were prepared by drop-casting 10 μl of a 100 times dilution of the colloidal sample solution. The images were acquired with a FEI Talos F200X transmission electron microscope equipped with a LaB₆ filament and operated at an acceleration voltage of 200 kV. HR-TEM and selected area diffraction, high-angle annular dark field imaging, tomography series and EDX elemental maps were acquired using a FEI-Osiris transmission electron microscope. The tomography series of Cu nanoparticles was performed by HAADF imaging in STEM mode (CL:87mm) from -58° to $+66^\circ$ with a tilt increment of 2° . For the silver nanoparticles, the tomography series was performed by HAADF imaging in STEM mode (CL:75 mm) from -70° to $+76^\circ$ with a tilt increment of 2° . The reconstruction was performed using the EM algorithm.

2.2.3 X-ray diffraction

X-ray diffraction with Bragg-Brentano configuration was recorded with a Bruker D8 advance diffractometer using Co K α (1.789 Å). X-ray diffraction measured with grazing incidence mode was performed on Bruker D8 Advance with Cu K α (1.540 Å). For both diffractometers the sample placed in an airtight specimen holder.

2.2.4 X-ray photoelectron spectroscopy

XPS spectra were recorded on a ThermoScientific K-Alpha spectrometer with a Al K α source (1486 eV). Fitting of the spectra was done with CasaXPS software with which a Shirley background protraction was performed. Survey scans were collected at constant pass energy of 200 eV and region scans at 50 eV.

2.3 Results and Discussion

2.3.1 Cu nanoparticle synthesis optimisation

To achieve Cu nanoparticles with the desired narrow size distribution and surface structure, the synthesis procedure of the reference was optimized.⁶⁶ After degassing at a vacuum atmosphere and heating to the first temperature threshold of 180 °C, samples were taken from the reaction vessel while maintaining a high heating rate. Extraction was performed by a N₂ flushed needle attached to a syringe with hexane. Only a small amount (0.5-1 ml) of the total reaction volume was taken as a sample to minimize its effect on the overall synthesis. The obtained samples were washed, centrifuged and re-dispersed in hexane. Of these samples the UV/VIS-absorbance was measured, shown in figure 22. To account for concentration differences between samples, the intensity of absorbance was normalised at 300 nm.

The sample taken at 170 °C possess a broad absorption band with its maximum at 600 nm. With increased reaction temperature this absorption maximum starts to sharpen and shift towards 580 nm until the sample that corresponds to a reaction temperature of 220 °C. After 220 °C the absorption band starts to broaden and has a slight blue shift with respect to the 220 °C sample. As the absorbance of the Cu nanoparticles is related to the localised surface plasmon resonance, the most narrow peak corresponds likely to the most narrow particle size distribution, which is the sample taken at 220°C. The less sharp absorption bands before the 220 °C sample, could be attributed to a large difference in size of nuclei which had been formed within different time frames. The broadening of absorbance after the 220 °C sample can be attributed to uncontrolled growth of nanoparticles to minimize their surface area. Based on these results, the second temperature threshold was chosen to be 220°C for the following heat-up synthesis of Cu nanoparticles.

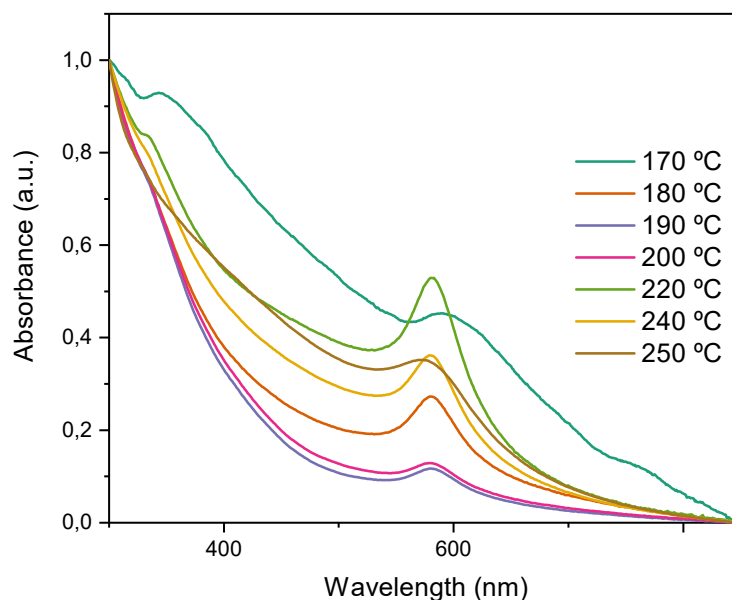


Figure 22: Normalised absorbance spectrum of samples taken from the reaction vessel at increasing reaction temperatures during the synthesis of colloidal Cu nanoparticles.

The resulting nanoparticles from the temperature optimised synthesis procedure were prepared for TEM imaging by drop-casting $10\ \mu\text{l}$ of a 100 times dilution of the sample on a TEM grid. As shown in figure 23, the produced Cu nanoparticles have a sufficiently small average diameter of 5.7 nm however, also posses a large PSD as can be seen from the size histogram. A deviation of 1.5 nm (over 10%) from the average Cu nanoparticle size is not sufficient for the use of analytical techniques based on ensemble statistics. Further optimisation of the synthesis to reduce the PSD is required.

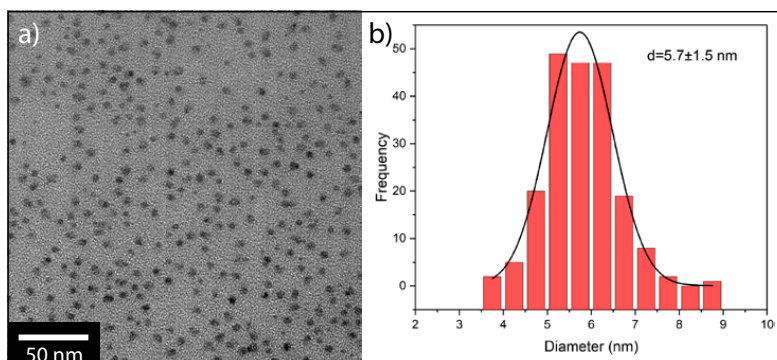


Figure 23: a) TEM image of Cu nanoparticles, (b) and the corresponding size histogram with average size and deviation.

The Cu nanoparticle synthesis was further optimised by the addition of an additional ligand, oleic acid, to the temperature optimised procedure to ensure control over nuclei growth. As shown in figure 24, the Cu nanoparticles have a uniform size distribution of 9.4 ± 0.7 nm and an absorption maximum at 580 nm. Furthermore, regular patterns of assembled nanoparticle structures can be observed. Such assemblies are a strategy of nanoparticles to reduce their surface energy, characteristic for nanoparticles with a sufficiently small size distribution. The uniform size distribution and self assembling character is ideal for the creation of thin catalytic films for the CO_2RR , thus concludes the Cu nanoparticle synthesis optimization.

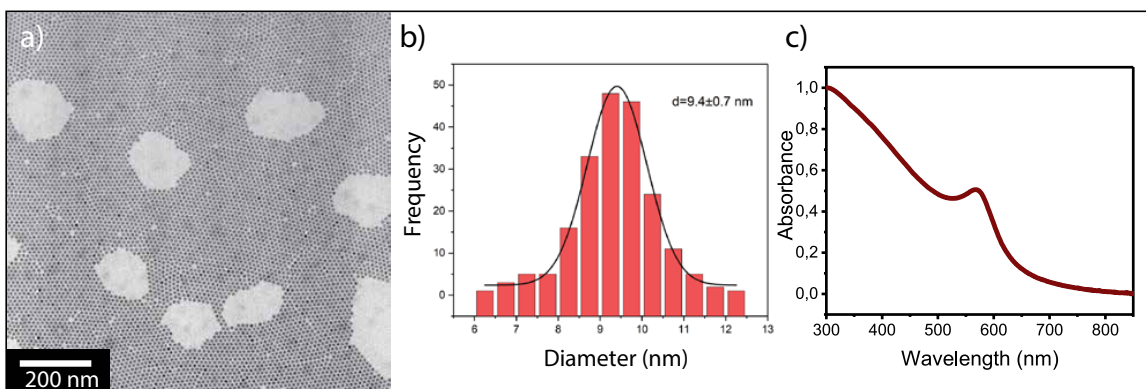


Figure 24: a) TEM image of Cu nanoparticles, (b) the corresponding size histogram of 200 counted nanoparticle, with average nanoparticle size and deviation and (c) the absorbance spectrum of the Cu colloidal dispersion with a maximum at 580 nm.

2.3.2 Ag nanoparticle synthesis optimisation

The silver nanoparticle synthesis procedure was adapted from the optimised copper nanoparticle synthesis. However to account for the increased reactivity of the AgNO_3 precursor, reaction temperatures were lowered to a maximum of $120\text{ }^\circ\text{C}$ to prevent rapid evolution of NO_x gas. As shown in figure 25 the acquired nanoparticle solution has an absorption maximum at 405 nm and a fairly uniform size distribution of $6.9 \pm 0.9\text{ nm}$. Difference in average particle and distribution of the Cu nanoparticles with respect to the silver nanoparticles could be as a result of the different nature of the elements as well as the increased reactivity of the AgNO_3 precursor. As increased reactivity may cause simultaneous rapid nucleation and growth resulting in a more broad particle size distribution.

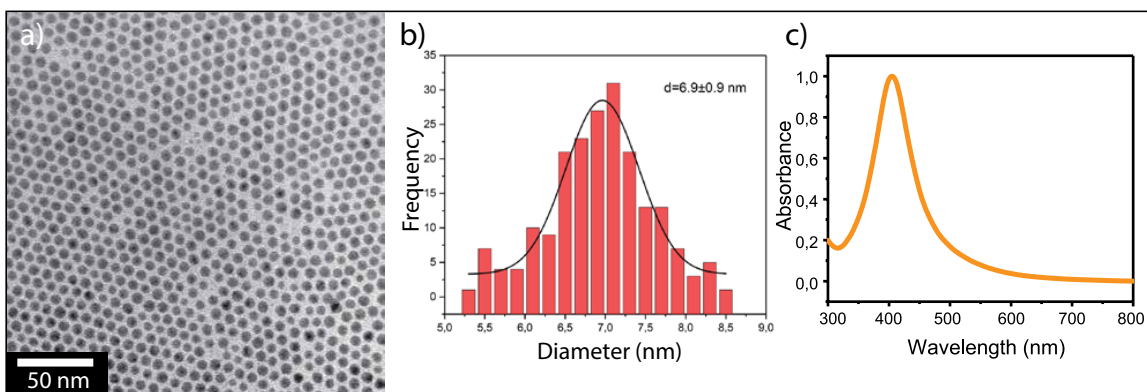


Figure 25: a) TEM image of Ag nanoparticles, (b) the corresponding size histogram of 200 counted nanoparticles, with average size and deviation and (c) absorbance spectrum of the Ag colloidal dispersion with a maximum at 405 nm .

2.3.3 Crystal structure determination of Cu and Ag nanoparticles

For the characterisation of the crystal structure of the Cu and Ag nanoparticles, X-ray diffraction (XRD) measurements with Bragg-Brentano and grazing incidence mode were performed as well as high resolution TEM (HRTEM) imaging and electron diffraction experiments.

Cu nanoparticles

A Cu film was made by drop-casting the colloidal Cu solution onto an ITO substrate inside a N_2 filled glovebox. The sample was loaded into an airtight dome to prevent the oxidation and characterised by XRD. In similar fashion, samples for HRTEM were prepared by drop-casting the colloidal Cu solution on a carbon coated Mo grid which were loaded in an airtight specimen holder in a N_2 filled glovebox.

The XRD pattern in figure 26a possess a Cu(111) reflection. The broad shape is characteristic of a nanoparticle sample, as the stacking of many nanoparticles results in disorder compared to the structure of a bulk metal. As Cu(111) is the first observed reflection in the diffraction pattern, the FCC lattice structure of the nanoparticles is evident. The FCC structure was further confirmed by the selected electron diffraction pattern (SAED) in figure 26c of the high resolution HAADF-STEM image in figure 26b. The observed rings correspond to the Cu(111), Cu(200), Cu(220) and Cu(311) Miller indices of which the hkl values are either fully even or odd, characteristic of a FCC crystal structure also indicating that only the metallic phase of Cu is present.

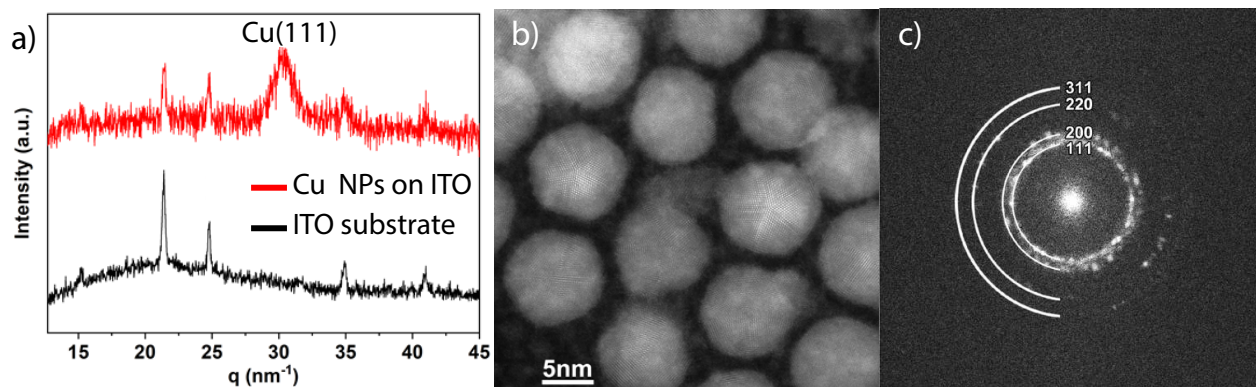


Figure 26: a) X-ray diffraction pattern of colloidal Cu nanoparticles on a ITO substrate with a ITO reference pattern, (b) High resolution HAADF-STEM image of Cu and (c) a selected area diffraction pattern (SAED) of the Cu nanoparticles.

From the magnified HRTEM image in figure 27a the icosahedral like shape of the nanoparticles can be observed, made apparent by the presence of the visible 5-fold symmetry of a pentatwinned domain. The icosahedron is a fivefold twinned particle of which the formation can be favoured for nanoscale crystallites of the FCC lattice.⁶⁶ A characteristic of this shape is a surface face energy anisotropy such that the $\{111\}$ indices are the lowest in energy for the surface of FCC crystals. To further investigate the surface faceting of the Cu nanoparticles, atomic resolution electron tomography was performed for four Cu nanoparticles. From the orthoslice (fig 27c) through the 3D reconstruction shown in fig 27b, it can be determined that the pentatwinned domains are present in all investigated nanoparticles, also confirming that the Cu(111) is the dominant facet. The surface facets of the Cu nanoparticles are therefore also dominant in the Cu(111) facet, on which the selectivity of methane is favoured for the CO₂RR.

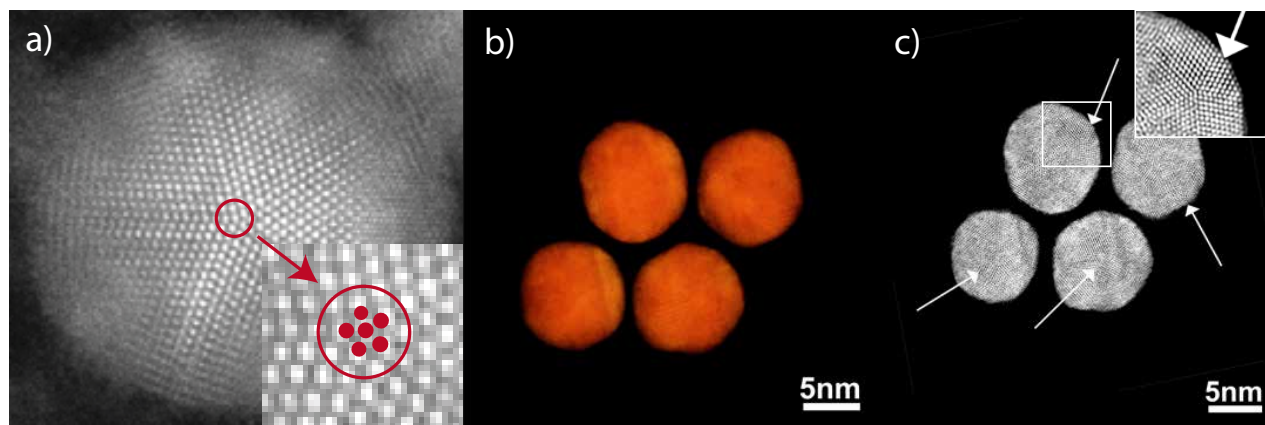


Figure 27: a) a magnification of the HRTEM image revealing 5-fold symmetry of the colloidal, (b) 3D presentation of the reconstructed volume of 4 Cu nanoparticles, obtained by an atomic resolution tilt series in HAADF-STEM mode and (c) a orthoslice through the reconstructed volume in (b), showing the pentatwinned domains, indicated by white arrows.

Ag nanoparticles

A Ag film was made by drop-casting the colloidal Ag solution onto a glassy carbon substrate and HRTEM samples were prepared by drop-casting the Ag colloidal solution on a carbon coated Mo grid.

The grazing incidence XRD pattern in figure 28 indicates the FCC lattice of the Ag nanoparticles of which the Ag(111) reflection is dominant. The shape of the nanoparticles at first glance can be approximated as spherical, as can be seen from the high resolution HAADF-STEM image in figure 29a. Increased magnification however reveals similar pentatwinned domains as observed for the Cu nanoparticles in figure 29c. The electron diffraction pattern in figure as well as the XRD pattern 29b confirm the FCC lattice. Similar to the Cu nanoparticles, only fully odd or even Miller indices can be observed, indicating the FCC lattice, the presence of only the metallic phase of Ag and that the Ag nanoparticles are polycrystalline.

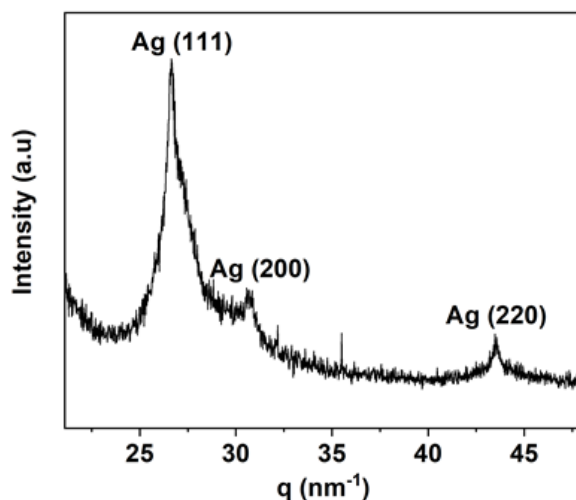


Figure 28: Grazing incidence X-ray diffraction pattern (0.5° angle of incidence).

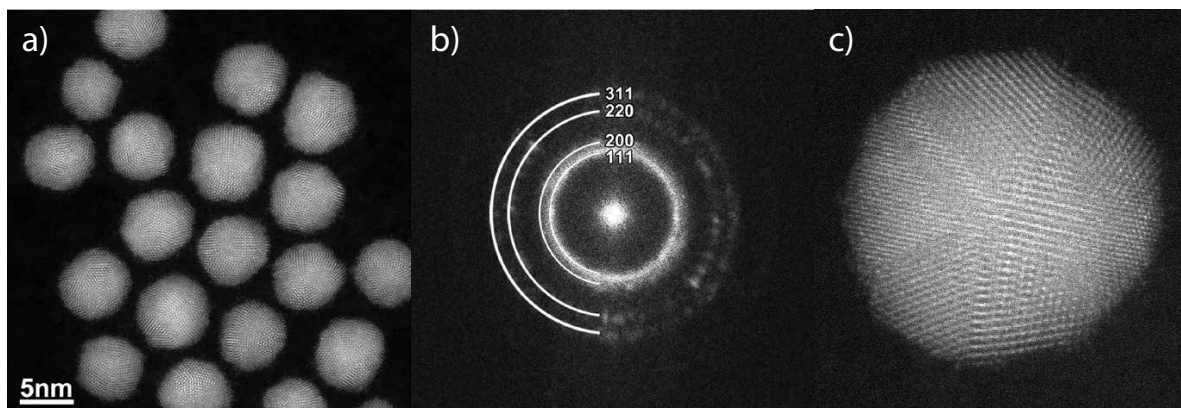


Figure 29: a) high resolution HAADF-STEM image, (b) electron diffraction pattern of colloidal Ag nanoparticles and (c) magnification of STEM image revealing penta-twinned domain.

2.3.4 Cu nanoparticle surface species

The Cu nanoparticles were proven to be extremely sensitive to oxidation by exposure to air. From the high resolution HAADF-STEM image of Cu nanoparticles that were exposed to air in figure 30 the loss of the well defined shape can be observed. The weaker contrast around the particles indicating a presumed copper oxide layer is further investigated by EDX mapping and XPS.

By EDX mapping of the high resolution HAADF-STEM image in figure 31a, elemental maps were obtained of Cu, O and a Cu O overlay, shown in figure 31b, c and d respectively. The elemental maps reveal the presence of oxygen on the Cu nanoparticles. To identify the oxygen species, XPS was performed of which the Cu 2p spectrum is shown in figure 32. Deconvolution of the peak at 935 eV by multiple peak fitting revealed the presence of three peaks corresponding to $\text{Cu}(\text{OH})_2$, CuO and elemental Cu in the order of decreasing binding energy. The peak area is proportional to the number density of the species. Thus it can be concluded that the surface species is mainly occupied by elemental Cu and to a lesser extend by CuO and $\text{Cu}(\text{OH})_2$. No peaks of any Cu(I) oxygen species could be observed.

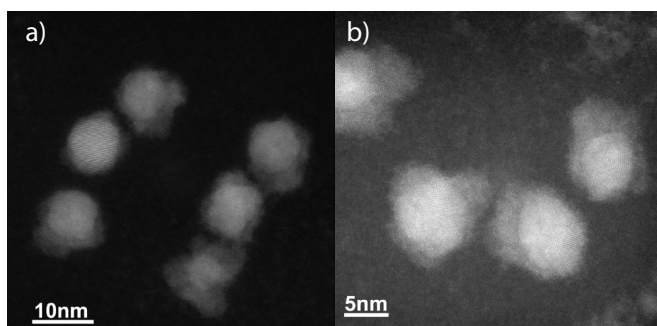


Figure 30: High resolution HAADF-STEM image of Cu nanoparticles after exposure to air.

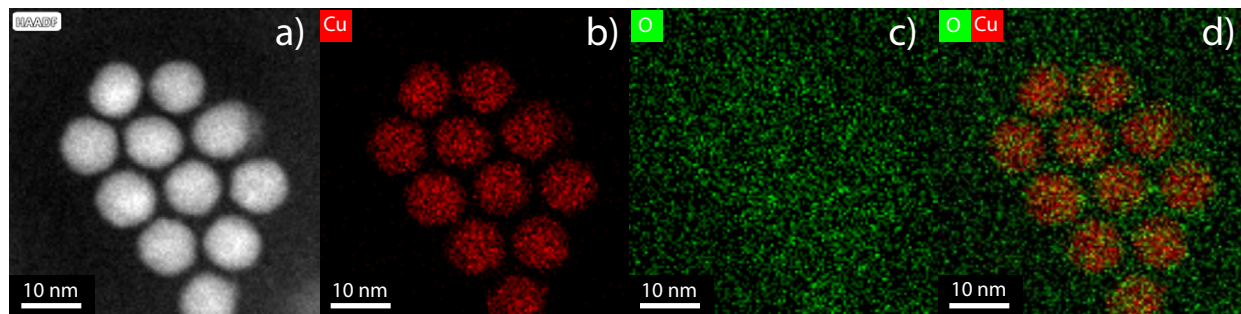


Figure 31: a) High resolution HAADF-STEM image, (b) Cu elemental map, (c) O elemental map and (d) overlay of Cu and O elemental maps from EDX measurements of colloidal Cu nanoparticles.

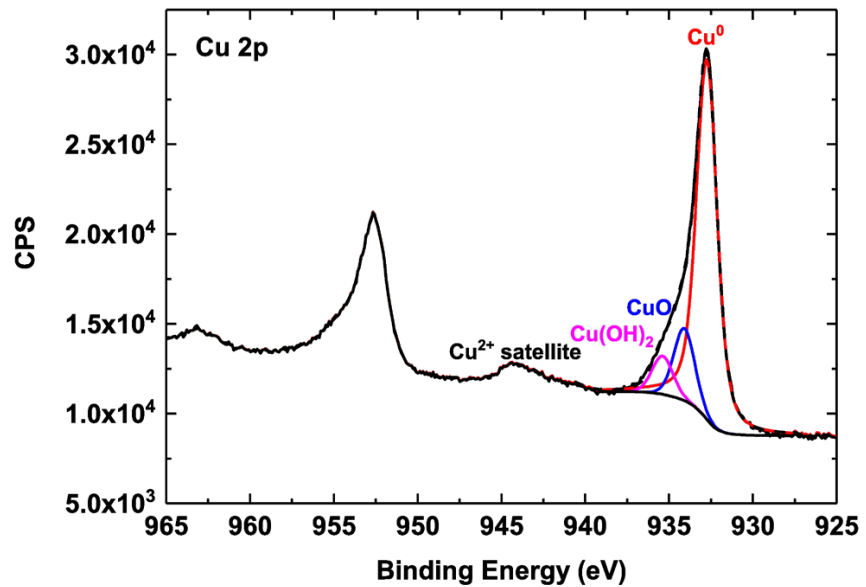


Figure 32: Cu 2P XPS spectrum of colloidal Cu nanoparticles.

2.3.5 Ag nanoparticle surface species

To determine the presence of possible oxygen species on the surface of the colloidal Ag nanoparticles similar EDX mapping (fig 33 and XPS (34) experiments were performed.

In figure 33a the high resolution HAADF-STEM image of the Ag nanoparticles is presented of which the Ag, O and Ag/O overlay elemental maps are shown in figure 33b, c and d respectively. The elemental maps indicate the presence of oxygen atoms at the surface of the nanoparticles, however considerably less than for the Cu nanoparticles. The Ag 3d XPS spectrum indicates that the surface exist entirely out of elemental Ag. Therefore the increased observed density of oxygen atoms with respect to the background can most likely be attributed to the presence of the oxygen atoms within the acid groups of the surface bound organic ligands.

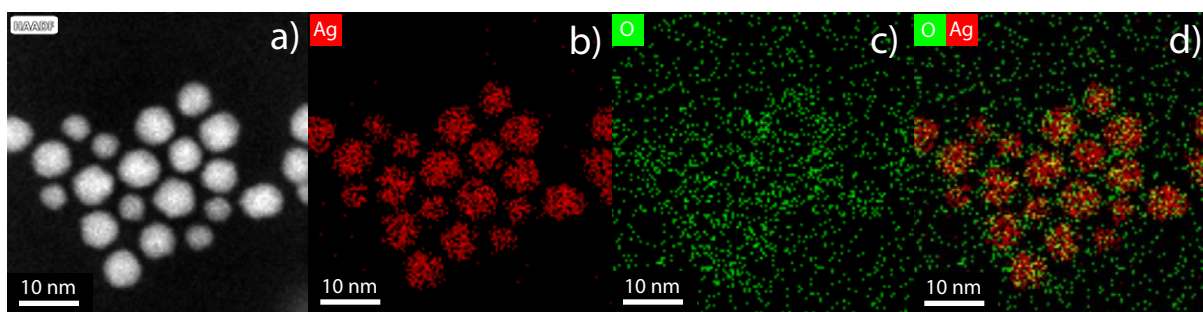


Figure 33: a) High resolution HAADF-STEM image, (b) Ag elemental map, (c) O elemental map and (d) overlay of Ag and O elemental maps from EDX measurements of colloidal Ag nanoparticles.

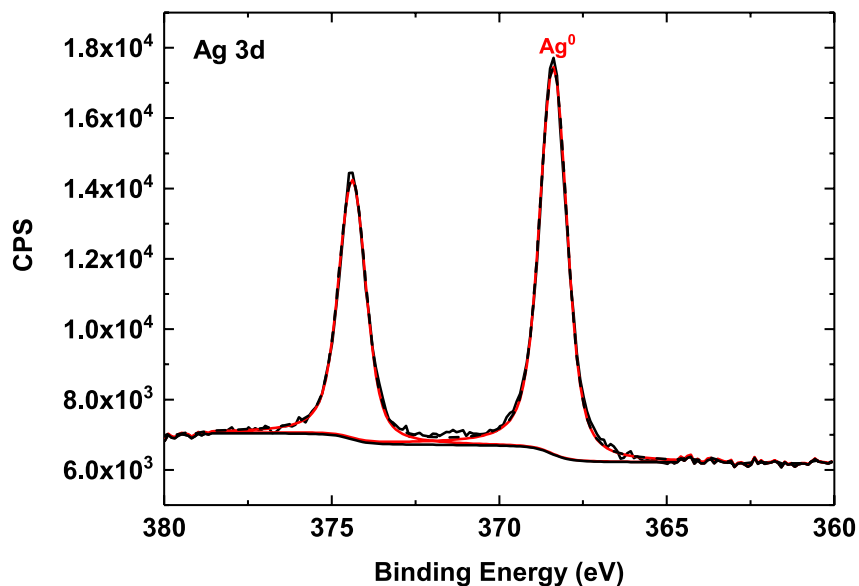


Figure 34: Ag 3d XPS spectrum of colloidal Ag nanoparticles

The difference in the susceptibility for oxidation between the Cu and Ag nanoparticles can be explained from their respective Pourbaix diagrams shown in figure 53 (Appendix), from which can be seen that metallic Ag is the dominant phase over a wide potential-pH range as well as the standard reduction potential. Ag has a higher positive standard reduction potential to be oxidized with respect to Cu.



Therefore, Cu is more much more easily oxidized than Ag when exposed to ambient conditions.

3 Electrochemical measurements and catalysis

From the Cu and Ag colloidal solutions described in the previous chapter, single element and binary nanoparticles electrodes were developed. In this chapter of the thesis the activity and selectivity of these electrodes is discussed. The accompanied structural changes with respect to surface oxides, surface bound ligands and nanoparticle agglomeration are investigated by *ex situ* infrared spectroscopy and scanning electron microscopy (SEM) and *in situ* Raman spectroscopy.

3.1 Experimental methods and materials

3.1.1 Activity set-up

The activity measurements of the nanoparticle electrodes were executed in a two-compartment home made three-electrode electrochemical H-cell. The cathode and anode chambers were separated by a cation exchange membrane (NafionTM 155). Prior to the CO₂RR, the electrolyte (0.1 M KHCO₃ in mili-Q water) was saturated through CO₂ by bubbling. During the measurements a continuous flow of CO₂ was bubbled through the cathode side of the electrochemical cell with a flow of 10 ml/min. The gas products generated at the cathode were directly vented into the gas-sampling loop of the gas chromatograph (Thermo Scientific TRACE 1300 Gas Chromatograph) equipped with a thermal conductivity detector (TCD) and a flame ionization detector (FID) for quantification.

3.1.2 Electrode preparation

Dropcasted nanoparticle electrodes were prepared by drop-casting the colloidal solutions onto a 1.0 cm² glassy carbon electrode in a nitrogen filled glovebox, letting the solvent evaporate overnight. The Ag and Cu concentration of the stock nanoparticle solutions were determined to be 0.026 and 0.064 mol/L respectively from ICP-OES. Cu nanoparticle electrodes were prepared by drop-casting 50 μ l resulting in a total Cu content of 0.20 mg. Ag nanoparticle electrodes were prepared by drop-casting 120 μ l resulting in a total Ag content of 0.34 mg. The metal content of both single element electrodes is in one to one stoichiometric ratio. Binary electrodes were made by the preparation of a Cu_{1.0}-Ag_{1.0} (molar ratio Cu/Ag = 1) mixture stock solution of both elemental colloidal solutions. Of the _{1.0}-Ag_{1.0} solution 85 μ l was dropcasted onto the glassy carbon electrodes resulting in a Cu content of 0.10 mg and a Ag content of 0.17 mg. Nanoparticle electrodes prepared by electrophoresis were made in a home-made two-electrode electrochemical cell with 1 cm distance between cathode and anode, of which the potential was controlled by a DELTA ELEKTRONIKA SM 300-5 power supply. A 100 times dilution was made of the stock Cu nanoparticle solution with hexane, 1 ml of this solution was added to the electrophoresis cell. For electrophoresis the cell was set at 100 V for 60 minutes for a thin film and 200 V for 60 min for a thick film. The electrodes were dried in a glovebox for at least 12 hours to ensure the evaporation of solvents. Before any catalytic performance measurements the electrodes were rinsed with 0.1 M KHCO₃.

3.2 Characterization techniques

3.2.1 Inductively coupled plasma optical emission spectrometry

The concentration of the nanoparticle solutions after synthesis was determined by inductively coupled plasma optical emission spectrometry (ICP-OES) by a PerkinElmer Optima 8300 Optical Emission Spectrometer.

3.2.2 Infrared spectroscopy (*ex situ*)

Infrared spectroscopy measurements were performed on pristine and spent nanoparticle electrodes, prepared by drop-casting 50 μl of Cu colloidal solution onto a 1 cm^2 glassy carbon electrode. The spent sample was used for the CO_2RR for one hour with an applied potential of -1.0 V vs RHE. A reference sample was prepared by drop-casting 0.5 ml of oleic acid onto a glassy carbon electrode. Vibrations were attributed using figure 52 (Appendix) and refs [70, 71].

3.2.3 Raman spectroscopy (*in situ*)

The *in situ* Raman measurements were performed in a home-made three-electrode electrochemical cell in a aqueous KHCO_3 solution of 0.1 M while bubbling CO_2 with a flow of 10 ml/min. The working electrode was prepared by drop-casting 50 μl of Cu colloidal dispersion onto a 1.0 cm^2 Ti (99.6+%) disk electrode. The Raman spectra were measured on a Renishaw inVia confocal Raman microscope with a laser with an excitation wavelength of 785 nm at various reducing potentials (V vs. RHE). Vibrations were attributed using ref [43, 72, 73].

3.2.4 Scanning electron microscopy (*ex situ*)

Scanning electron microscopy (SEM) images as well as EDX elemental maps were acquired on a FEI Helios Nanolab G3 with an accelerating voltage of 5.0 keV and a probe current of 0.2 nA.

3.3 Electrochemical measurements

3.3.1 Cyclic voltammetry

A broad range voltammogram was made of a Cu nanoparticle electrode with a scan rate of 20 mVs^{-1} . For the electrochemical active surface area determinations cyclic voltammograms were recorded in the non-faradaic region from 0.46 to 0.50 V vs. RHE at the scan rates 30, 50, 90, 110, 140 and 160 mVs^{-1} .

3.3.2 Chronoamperometry

For the activity and selectivity assessment of the single element and binary nanoparticle electrodes, measurements were performed for 1 hour at applied potential levels ranging from -0.8 to -1.3 V vs. RHE. For each potential a pristine nanoparticle electrode was used to account for possible surface reconstruction of the previous measurement.

3.4 Results and discussion

3.4.1 Study of ligands under CO₂RR conditions

Surface bound molecules such as ligands are undesired for any catalytic process. The presence of ligands makes the surface less accessible for reactants, reducing reaction rates thereby, decreasing the activity of the catalyst. With *ex situ* infrared (IR) spectroscopy and *in situ* Raman spectroscopy the ligands of a Cu nanoparticle electrode prepared by drop-casting were studied under CO₂RR conditions.

Infrared spectroscopy (*ex situ*)

From the IR spectrum in figure 36, the CH₃ and CH₂ stretching vibrations can be observed for the pristine Cu nanoparticle electrode. These vibrations indicate the presence of some organic material at the surface of the electrode. The C-H vibrations, as well as the fingerprint area, seem to overlap with the IR spectrum of oleic. However, the characteristic C=O stretch vibration (1708 cm⁻¹) acid as well as the P=O stretch vibration (1470 cm⁻¹) of both ligands functional groups are missing. Looking at the fingerprint area, vibrations at 1510 and 1455 cm⁻¹ can be observed and were attributed to the symmetric and asymmetric stretch of (-COO⁻), from which it can be concluded that oleic acid is present. The absence of the C=O stretch vibration can be explained by coordination to the Cu surface atoms (fig 35a), also indicating that the Cu nanoparticle surface is only covered by a single layer of oleic acid.⁷⁰ The only possible configuration for a phosphonic acid functional group to coordinate to the surface, without allowing for the P=O stretching mode is by tri-dentate bonding to the surface atoms.⁷¹ TDPA could therefore be attached to the surface via three symmetric P-O-Cu bonds, shown in figure 35b. The fingerprint area of the pristine sample spectrum however, more closely resembles that of oleic acid.

The occupation of the surface by oleic acid can be confirmed. The presence of TDPA is unclear, a more detailed investigation of the fingerprint area is needed. The IR spectrum of the spent Cu nanoparticle electrode possess no vibrations that could be attributed to organic molecules, other than the small peak at 2981 cm⁻¹ that corresponds to isopropanol, which was an impurity in the measuring crystal. It can therefore be concluded that the organic ligands are removed within one hour of applying CO₂RR conditions.

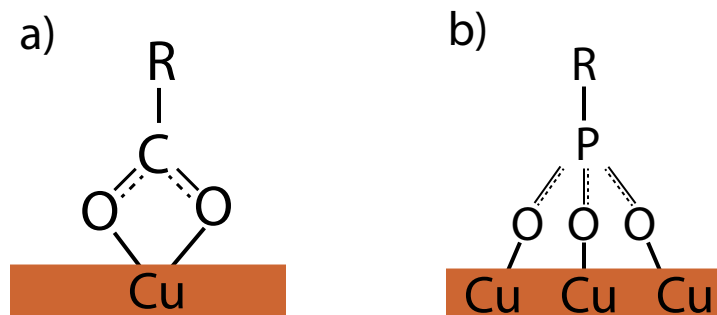


Figure 35: Configuration of surface bound (a) carboxylic acid and (b) phosphonic acid functional groups that do not exhibit their characteristic C=O and P=O stretching vibration in IR spectroscopy.

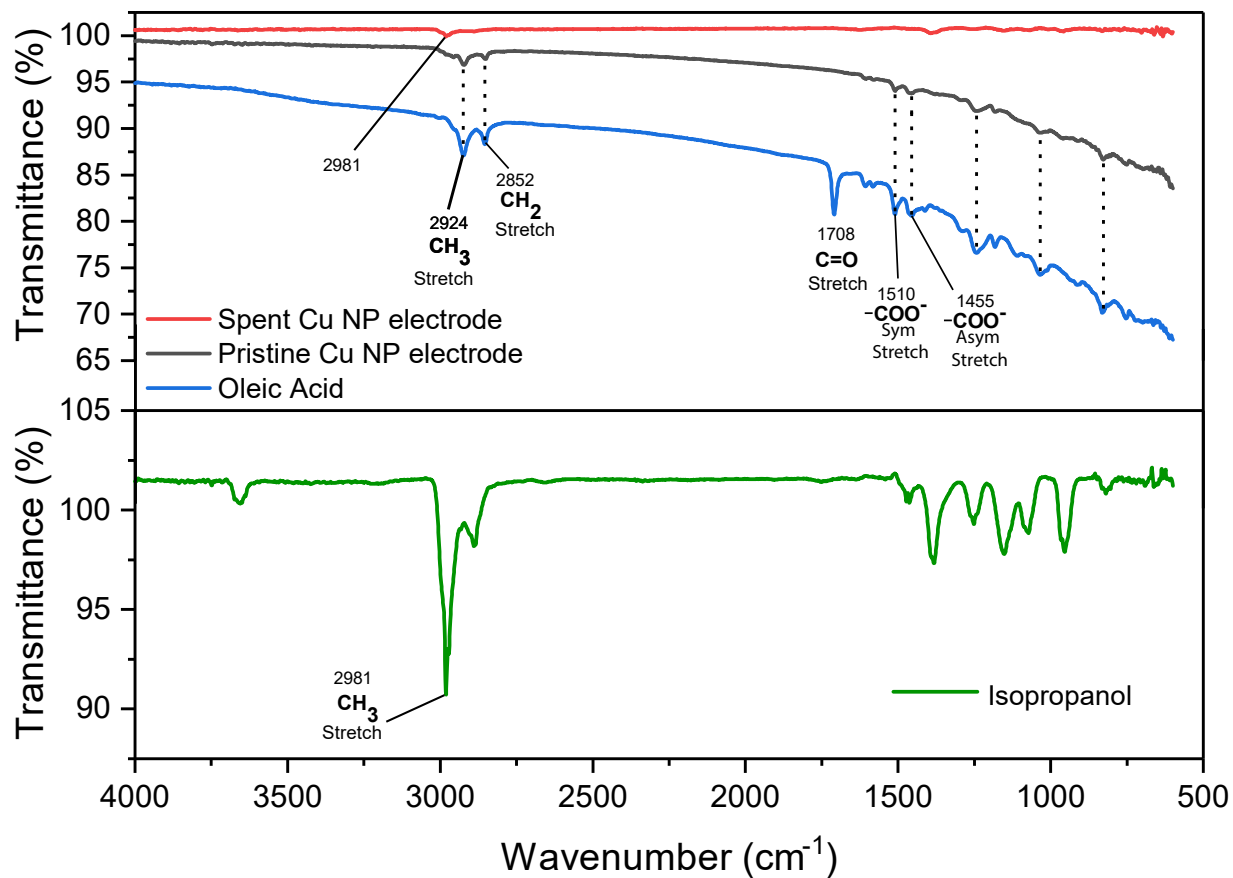


Figure 36: IR spectrum of a pristine Cu nanoparticle electrode, spent Cu nanoparticle electrode with an oleic acid and isopropanol reference spectrum.

Raman spectroscopy (*in situ*)

From the Raman spectra in 38a, only two vibrations at 1300 and 1463 cm^{-2} could be distinguished at circuit potential (OCP) and at -1.2 V vs. RHE. The vibrations have been assigned to the CH_2 twisting and scissoring respectively (fig 37). Both CH_2 vibrations occur in the reference spectrum of TDPA and oleic acid at a similar position. Again the characteristic $\text{C}=\text{O}$ vibration of oleic acid is not visible in the spectrum. From IR it was concluded that oleic acid is present however the functional group is coordinated to the Cu surface atoms not allowing the vibrational mode of $\text{C}=\text{O}$. Similar to IR, the absence of the $\text{C}=\text{O}$ vibrational mode in Raman can therefore be explained by surface coordination. Furthermore, no characteristic features of TDPA could be distinguished. Vibrations that would be expected for an alkyl phosphonic acids include, the stretching vibrations $\text{P}-\text{O}$ (890 cm^{-1}), $\text{P}=\text{O}$ (1178 cm^{-1}) and $\text{PO}-\text{H}$ (1250 cm^{-1}).⁷⁴ However, if the phosphonic acid functional group is coordinated by tri-dentate bonding as discussed in the IR section, none of these vibrational modes are possible and would therefore not show up in the Raman spectrum.

By increasing the potential from -0.8 to -0.9 V vs. RHE the CH_2 vibrations diminish, indicating the desorption of oleic acid and TDPA from the surface of the nanoparticle. Within the same time frame it can be seen from figure 38b that the intensity of the 1070 cm^{-1} vibration, attributed to surface adsorbed carbonate species, increases as a function of applied potential by the establishment of the electrical double layer around the nanoparticle electrode. Thus indicating a possible exchange between surface adsorbed ligands for carbonate species as shown in figure 39.

From both the IR and Raman spectra the presence of surface a organic molecule at the surface of the electrode can be confirmed from CH_2 vibrations. These vibrations are from coordinated oleic acid and possibly coordinated TDPA ligand molecules. Once a potential is applied, the CH_2 vibrations diminish and the electrical double layer is established as a result of potential induced ligand stripping.

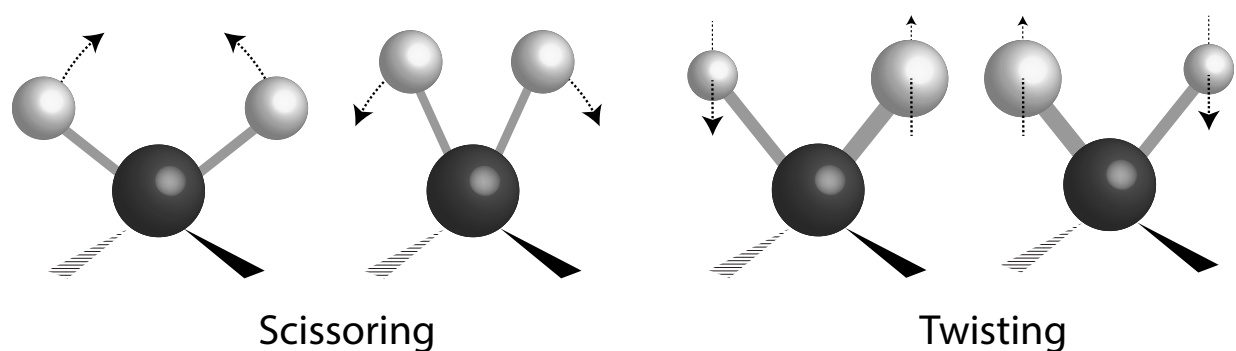


Figure 37: The scissoring, the simultaneous movement of carbon bonded hydrogen atoms towards and apart from each other within the same plane and twisting, the alternating movement of carbon bonded hydrogen atoms through and out of their plane, vibrational modes of a methylene group in a molecule.

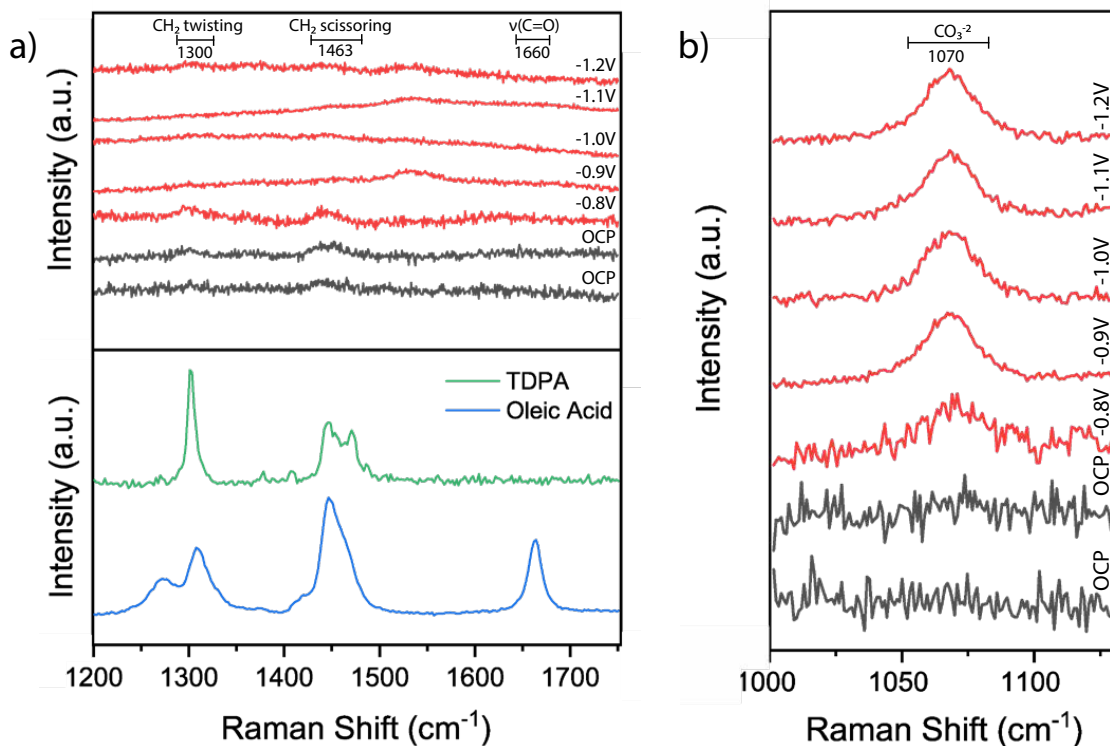


Figure 38: *in situ* Raman spectra with increasing applied potential V vs. RHE starting from open circuit potential (OCP) of a Cu nanoparticle electrode (a) with a reference spectrum of the ligands TDPA and oleic acid and (b) in the carbonate region.

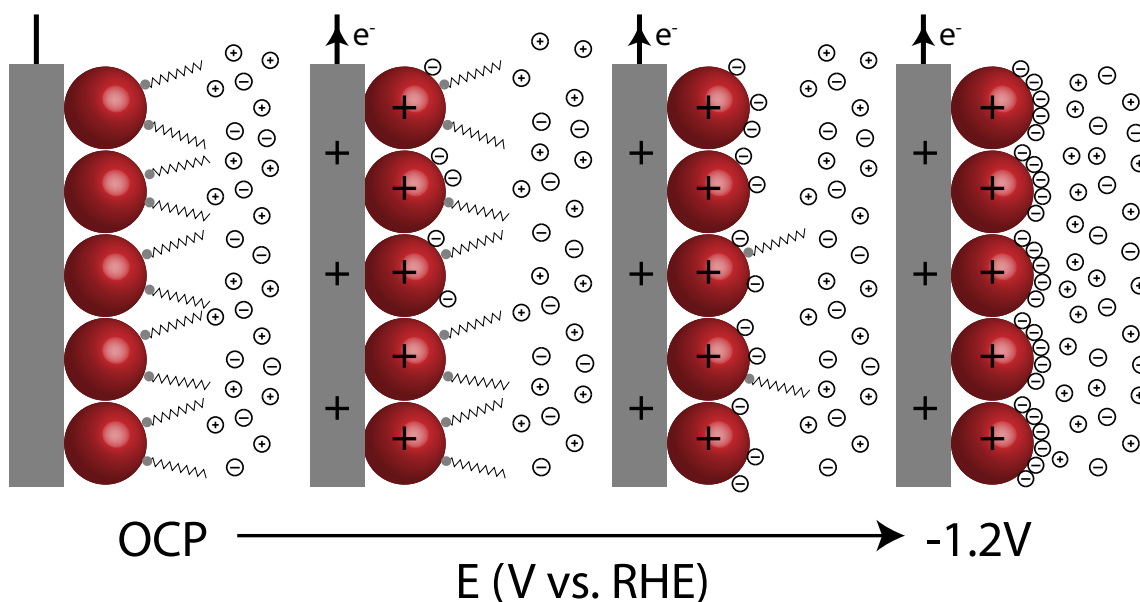


Figure 39: Removal of surface bound ligands and the simultaneous establishment of the electrical double layer with increasing applied potential with CO_3^{2-} anions and K^+ cations

3.4.2 Study of the electrode surface and oxide species during the CO₂RR

From high resolution electron microscopy imaging and EDX mapping (figures 30 and 31) the sensitivity of the Cu nanoparticles for oxidation was observed. With *in situ* Raman spectroscopy and optical microscopy, these oxide species and the general surface of a dropcasted Cu nanoparticle electrode were studied during the CO₂RR.

Two vibrations can be observed in the low wave number region of the Raman spectra in figure 40. Vibrations can be observed around 360 cm⁻¹ and a broad vibration at 620 cm⁻¹ with a shoulder at 530. The vibrations around 360 cm⁻¹ were attributed to surface adsorbed species of CO₂ and the vibrations at 530 and 620 were attributed to the Cu/Cu₂O species.^{43,73} Once a reducing potential was applied, the observed vibrations shift or disappear within each Raman spectrum over time. The shifting of vibrations around 360 cm⁻¹ indicates different coordination of surface bound CO₂.⁷³

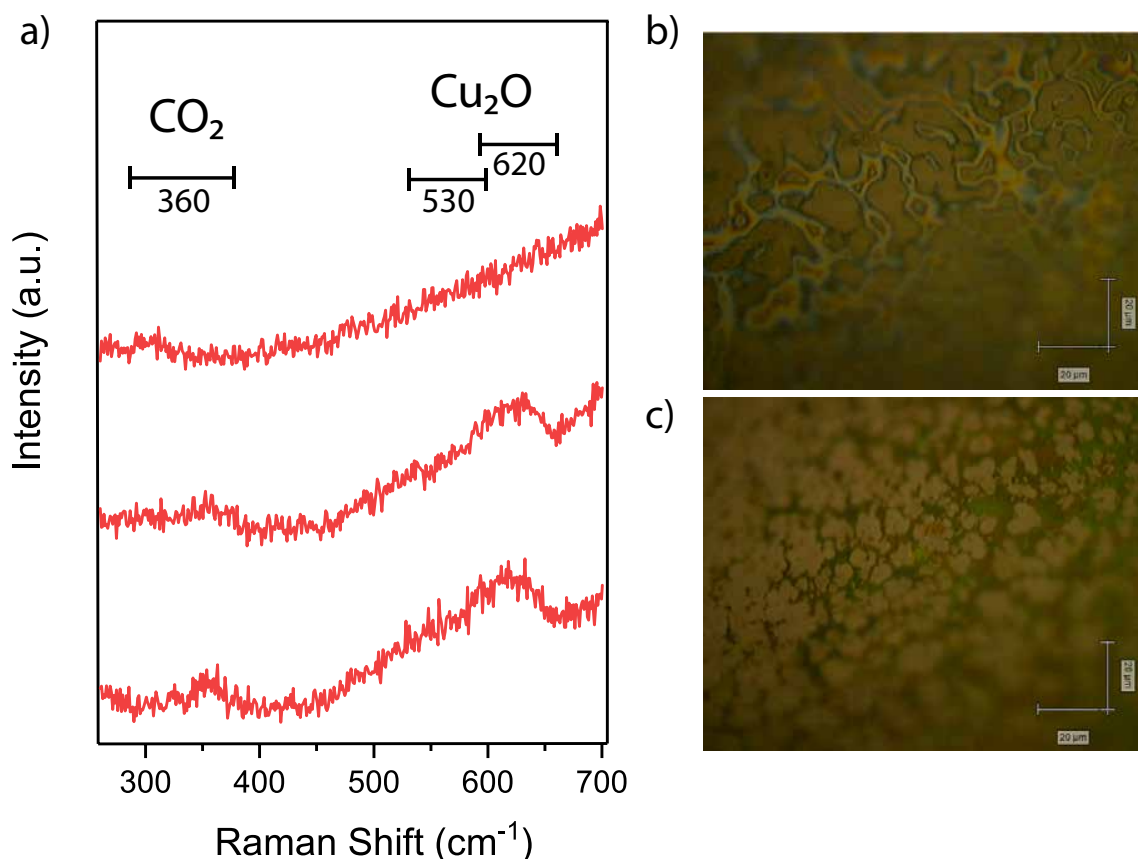
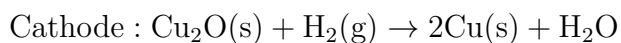
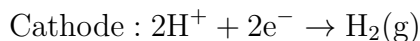
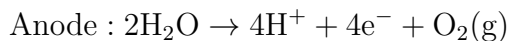


Figure 40: Time resolved Raman spectrum of the *in situ* CO₂RR with a Cu nanoparticle electrode at an applied potential of -1.2 V vs. RHE with 10 seconds between each spectrum. (b) Image of the nanoparticle electrode before reduction and (c) image of the nanoparticle electrode after reduction.

The vibrations of the Cu/Cu₂O species diminish once the sample has been exposed to an applied potential for some time, indicating the reduction of Cu₂O to Cu by the following reactions:



Images from the optical microscope of the electrode are shown in figure 40b and c. Before reduction (fig 40b) slight hints of blue and red can be observed at the surface of the in water submerged electrode. The colours seem to resemble iridescence from a oil water interface by thin film interference.⁷⁵ After reduction (fig 40c), the colours have disappeared and the surface is covered in larger Cu structures. The disappearance of iridescence could be caused by the removal of the fatty ligands that are covering the surface of the electrode by the potential induced stripping. After the ligands are removed, no stabilizing agent is present to prevent the aggregation of nanoparticles, resulting in the observed larger structures of Cu. The potential induced surface reconstruction is further investigated with SEM imaging in the following sections.

3.4.3 Dropcasted Cu nanoparticle electrodes faradaic efficiency/stability

The faradaic efficiencies of the Cu nanoparticle electrodes prepared by dropcasting are presented in figure 41a. At relatively low applied potentials, -0,8 and -1.0 V vs. RHE, the majority of the reaction product is hydrogen by over 90% and about 1 to 2% of CO. Faradaic efficiencies in this range are uncharacteristic for a Cu based electrode, especially with surface that is dominant in the Cu(111) facet (section 2.3.3). However, it was determined that the Cu nanoparticles are extremely sensitive to oxidation (section 2.3.4). Cu-oxide layers are quickly formed when the nanoparticles are exposed to air and cause the loss of their well defined shape as a result. As the electrochemical measurements are performed under ambient conditions, oxidation of the nanoparticle electrodes will occur before a reducing potential is applied. Upon reduction of the oxide species during the electrochemical measurement, the resulting surface structure is drastically reconstructed as can be seen from the *ex situ* SEM images in figure 42.

The overall CO₂RR selectivity has been reported to decrease drastically when approaching the nanoscale size range (1-10 nm), with an intrinsic selectivity favouring hydrogen production as a result of the dominance of highly undercoordinated surface atoms.⁷⁶ The reconstructed structures at low applied potential are likely also dominant in highly undercoordinated Cu surface atoms, resulting in the high selectivity for hydrogen. Alternatively, the high selectivity for hydrogen could be explained by ligands that are still coordinated to the surface, blocking active sites for hydrocarbon products. However, no vibrations of ligands could be perceived after an hour of the CO₂RR at -1.0 V vs. RHE (section 3.4.1).

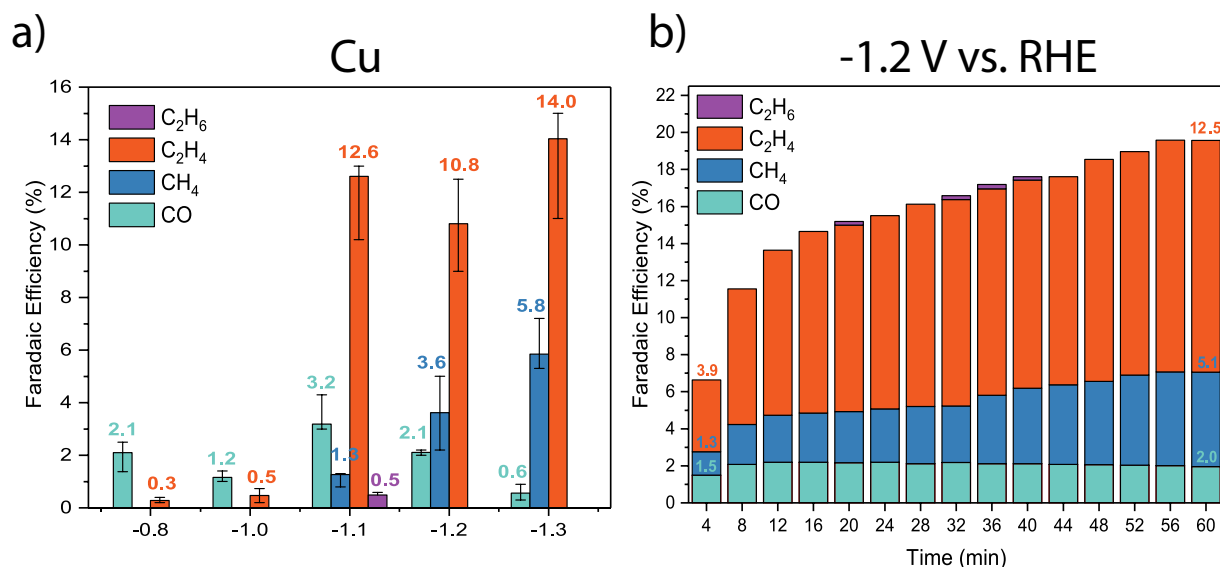


Figure 41: a) Faradaic efficiency for the CO₂RR of Cu nanoparticle electrodes prepared by drop-casting at various potentials for an hour and (b) the faradaic efficiency of a Cu nanoparticle electrode measured at -1.2 V vs. RHE with respect to time.

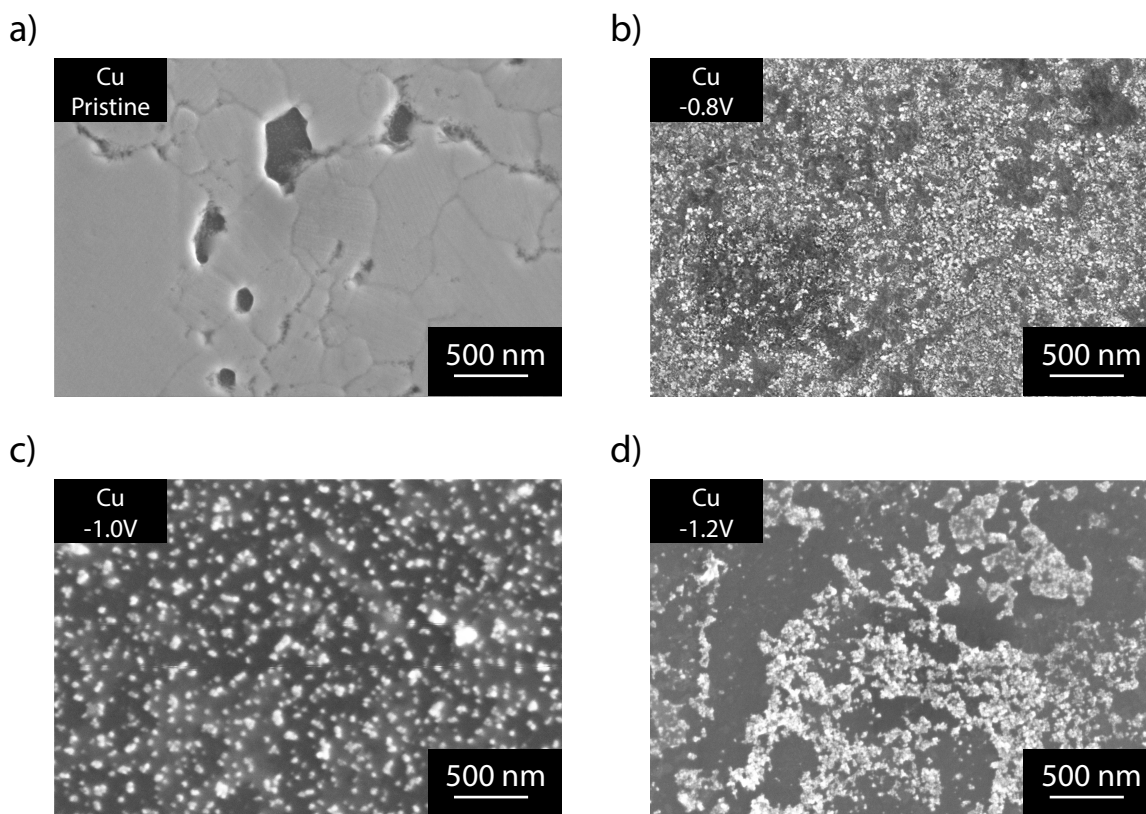


Figure 42: SEM images Cu nanoparticle films prepared by drop-casting. (a) Pristine nanoparticle electrode, (b) nanoparticle electrode after -0.8, (c) -1.0 and (d) -1.2 V vs. RHE for an hour of CO₂RR.

At higher applied potentials, from -1.1 to -1.3 V vs RHE, the overall CO₂RR faradaic efficiency for C products is increased to 17.6, 16.5 and 20.4% respectively. From figure 41b, an increase in selectivity for ethylene and methane and a decrease in selectivity of CO can be seen as a function of time of a Cu nanoparticle electrode measured at -1.2 V vs. RHE. A similar trend was observed for the Cu nanoparticle electrodes measured at -1.1 and -1.3 V vs. RHE (Appendix figure 54).

As the activity measurement progresses, the overall selectivity of CO₂ reduction approaches the intrinsic selectivity of a bulk Cu electrode. From the SEM image after catalysis in figure 42d, large structures of agglomerated nanoparticles can be observed on the surface of the electrode, explaining the bulk like selectivity for CO₂ reduction. The dropcasted catalytic films order their nanoparticles in patterns by assembly. The resulting distance between the respective nanoparticle can therefore be approximated by the length of the intervening surfactant molecules. Once the ligands are removed, coalescence of nanoparticles will be favourable to minimize their surface area.²⁴ At such small length scales between particles, rapid aggregation is likely to ensue. However, recently the most likely assumed degradation mechanism for Cu nanocrystals electrodes is growth by dissolution redeposition.⁷⁷ Clusters of nanoparticles are fragmented once oxidized by the electrolyte and redeposit back on the electrodes surface resulting in the growth of the original nanocrystals into larger particles as shown in figure 42.

3.4.4 Dropcasted Ag nanoparticle electrodes faradaic efficiency/stability

The faradaic efficiencies of the Ag nanoparticle electrodes prepared by dropcasting are presented in figure 43a. The main product was determined to be CO with a maximum of 69.3% at -1.0 V vs. RHE and hydrogen. As can be seen from 43b, the selectivity for CO over time was determined to increase until 70% after which it was stable for the remainder of the measured hour. A similar trend was observed for the nanoparticle electrodes measured at -0.8 and -1.2 V vs. RHE (Appendix figure 55). When observing the surfaces by the SEM images in figure 44 of the pristine and spent electrodes, the formation of dendritic structures is revealed. Dendritic structures could already be perceived under the mild reaction condition of -0.8 V vs. RHE. Further exposure to potential for longer periods of time ultimately transforms the dendrite structures to micro scale needles (fig 43c).

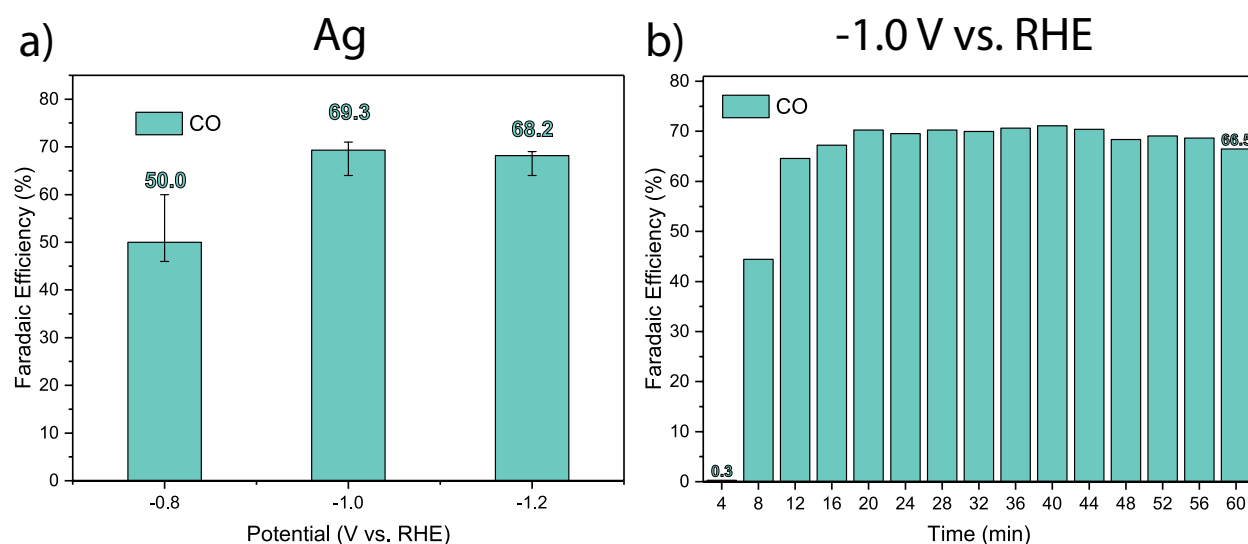


Figure 43: a) Faradaic efficiency for the CO₂RR of Ag nanoparticle electrodes prepared by drop-casting measured at various potentials for an hour and (b) the faradaic efficiency of a Ag nanoparticle electrode measured at -1.0 V vs. RHE with respect to time.

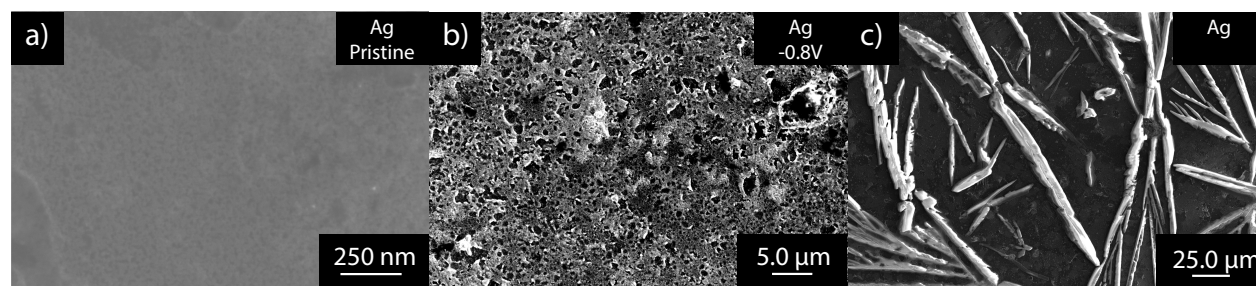


Figure 44: SEM images of Ag nanoparticle films prepared by drop-casting (a) Pristine nanoparticle electrode, (b) nanoparticle electrode after -0.8 V vs. RHE for an hour of the CO₂RR and (c) after multiple measurements.

Similar dendritic structures have been reported in previous research for Au nanoparticles during CO₂ reduction.⁷⁸ The formation of the dendritic structures was attributed to surfactant-ligated nanoparticles taking a random walk along the support, colliding with their neighbours and fusing. Furthermore, Brownian motion, bubble formation and particle charging are thought to contribute to the mobility of small aggregates stimulating dendrite formation with increased negative applied potential. Based on the selectivity over time, the aggregation of nanoparticles must be very fast as the faradaic efficiency rapidly approaches that of bulk Ag.

As the dropcasted Ag nanoparticle films are highly dense in nanoparticles, the chance of two randomly walking Ag nanoparticles to meet each other and collide is very likely. The formed dendrite structures are therefore likely the result of this mechanism. The difference in assumed degradation mechanism for Cu and Ag nanoparticle electrodes explains the difference in the resulting formed aggregate structures that are perceived in the (*ex situ*) SEM images in figures 42 and 44. The reason for dissolution redeposition to be the unlikely mechanism for degradation is that oxidation is required for dissolution to occur. As proven from section 2.3.5, the Ag nanoparticles do not oxidise like the Cu nanoparticles under similar conditions.

3.4.5 Dropcasted Cu-Ag nanoparticle electrodes faradaic efficiency/stability

The faradaic efficiencies of the $\text{Cu}_{1.0}\text{-Ag}_{1.0}$ (molar ratio $\text{Cu}/\text{Ag} = 1$) binary electrodes prepared by drop-casting are presented in figure 45a. Compared to the single element electrodes, the faradaic efficiency for methane, ethylene and CO is substantially lower. Maximum faradaic efficiencies for ethylene (1.3%) and CO (15.6%) were obtained at -1.0 V vs. RHE. In comparison to the single element electrodes, severe aggregation of nanoparticles is not observed for the binary $\text{Cu}_{1.0}\text{-Ag}_{1.0}$ electrode at -0.8V vs. RHE in figure 46a. However, the very low faradaic efficiency of 1.3% for ethylene is not relate able to a Cu(111) dominated surface as was perceived for the Cu nanoparticles.

The corresponding EDX elemental map in figure 46b reveals a relatively uniform distribution of Cu and Ag. With increased applied potential however, phase segregation of Cu and Ag occurs, forming domains of Cu and Ag aggregates on the -1.0 V vs. RHE nanoparticle electrode (figures 46c and d). By further increasing the applied potential to -1.2 V vs. RHE, aggregation of nanoparticles occurs across the entire binary film (figures 46e and f), similar to the single element electrodes. The faradaic efficiency for CO and ethylene at -1.0 and -1.2 V vs. RHE could be attributed to these large aggregated domains of Ag and Cu nanoparticles respectively. The aggregated structures were further investigated by scraping some of the aggregated electrode film onto a TEM grid for HAADF-STEM imaging and development of elemental maps by EDX. The results of which are shown in figure 47.

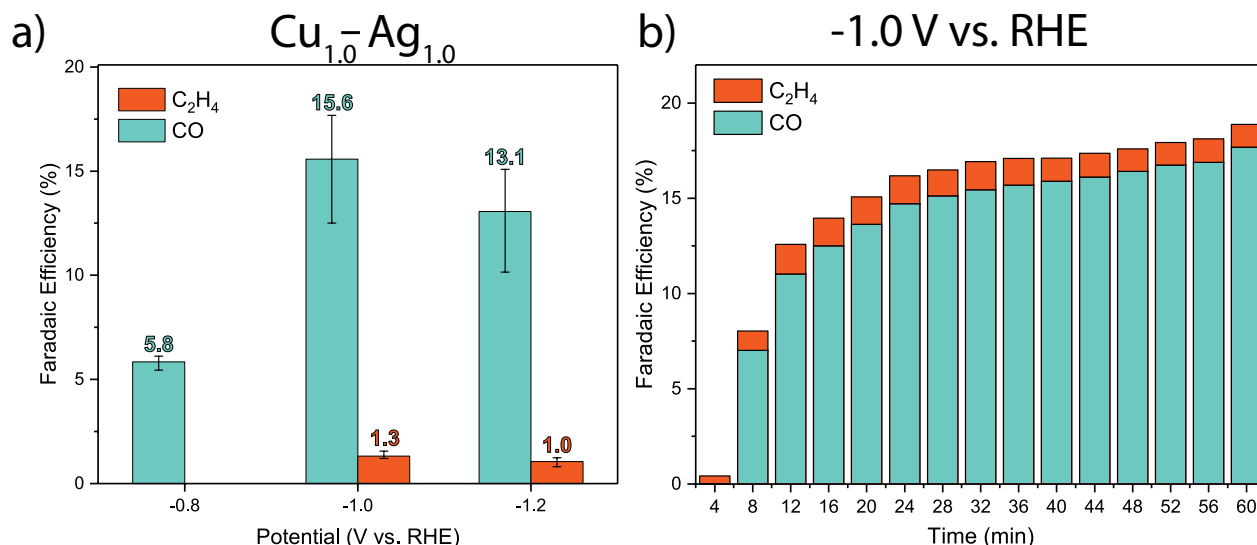


Figure 45: a) Faradaic efficiency for the CO_2RR of $\text{Cu}_{1.0}\text{-Ag}_{1.0}$ binary electrodes prepared by drop-casting at various potentials for an hour and, (b) the faradaic efficiency of a binary electrode measured at -1.0 vs. RHE.

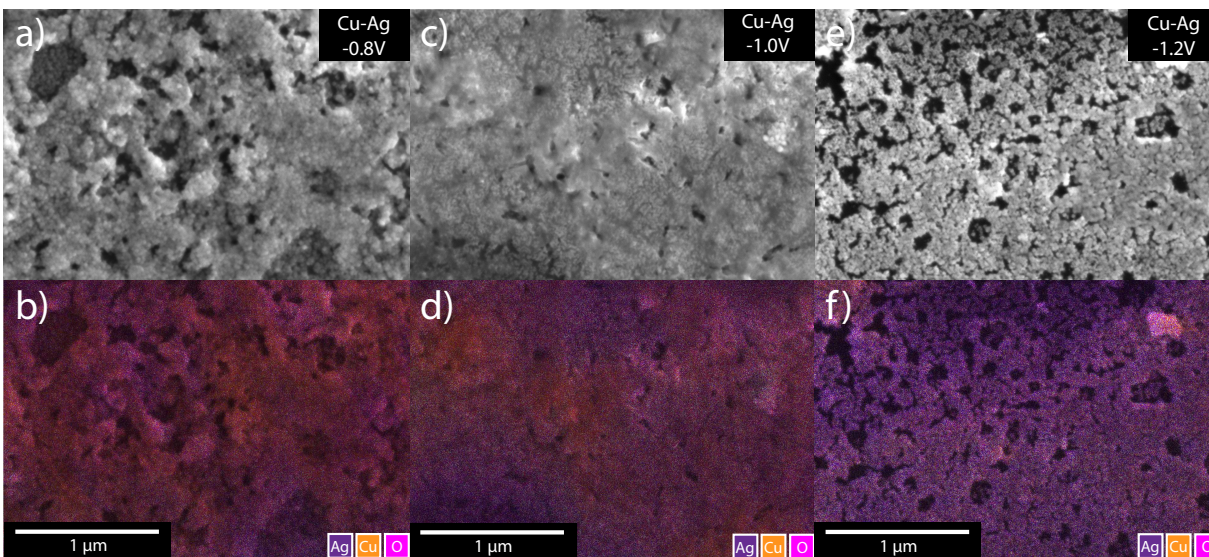


Figure 46: SEM images of $\text{Cu}_{1.0}\text{-Ag}_{1.0}$ binary films prepared by drop-casting after CO_2RR at various applied potentials for an hour, (a) -0.8 V (c) -1.0 V (e) -1.2 V vs. RHE and with their respective EDX elemental maps (b, d and f).

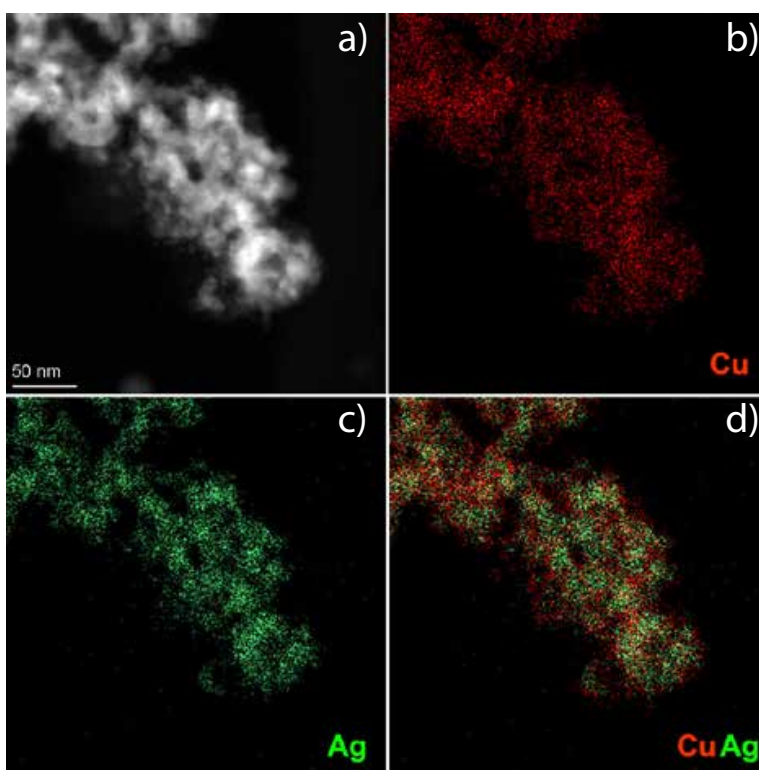


Figure 47: a) HAADF-STEM image and the corresponding EDX elemental maps of (b) Cu, (c) Ag and (d) Cu and Ag for Cu-Ag nanoparticle electrodes the CO_2RR at -1.0 V vs. RHE for 1 hour

The less severe aggregation for the -0.8 and to some extent the -1.0 V vs. RHE electrodes could be explained by the immiscible nature of Cu and Ag based on the previously discussed degradation mechanisms of Cu and Ag nanocrystals. From the *ex situ* SEM images, no dendritic structures can be seen at low applied potential. By the mixture of Cu and Ag nanoparticles, the chance that a Ag nanoparticle would collide to a fellow Ag nanoparticle is substantially smaller. As a result less collisions between Ag nanoparticles occur that can result in the formation of small aggregates that can agglomerate into dendritic structures.

Furthermore, the dissolution redeposition of Cu nanoparticles is less likely to result in large Cu structures or Cu rich regions as can be seen from the *ex situ* SEM images in figure 47 for Cu and Ag mixed nanoparticle electrodes. The analysed fragment is well mixed in Cu and Ag nanoparticles as can be seen from the EDX mapping. The Cu clusters that are fragmented from the mixed nanoparticle electrodes most likely redeposit while preserving their mixed distribution and their original nanoscale size.

An explanation for this is given in previous research. It has been shown that Cu-Ag binary systems possess positive enthalpy of mixing in both solid and liquid states, causing copper and silver to be immiscible.⁷⁹ From Cu-Ag experiments with alloyed films or nanoparticles, phase separation is usually perceived during their preparation,⁷⁹⁻⁸¹ suggesting that FCC Cu and Ag are immiscible phases incapable of forming solid solutions. The fragmented Cu nanoparticles that traverse to the electrolyte are therefore more likely to redeposit back on the well separated Cu nanoparticles, preserving the mixed Cu and Ag morphologies under mild reaction conditions.

Based on the CO₂RR faradaic efficiency and *ex situ* SEM measurements of the Cu, Ag and binary electrode films, we suggest that there is a stabilisation effect between Cu and Ag nanoparticles that mitigates aggregation of small (<10 nm) nanoparticles by preserving of the original morphology during electrocatalytic measurements, summarised in figure 48.

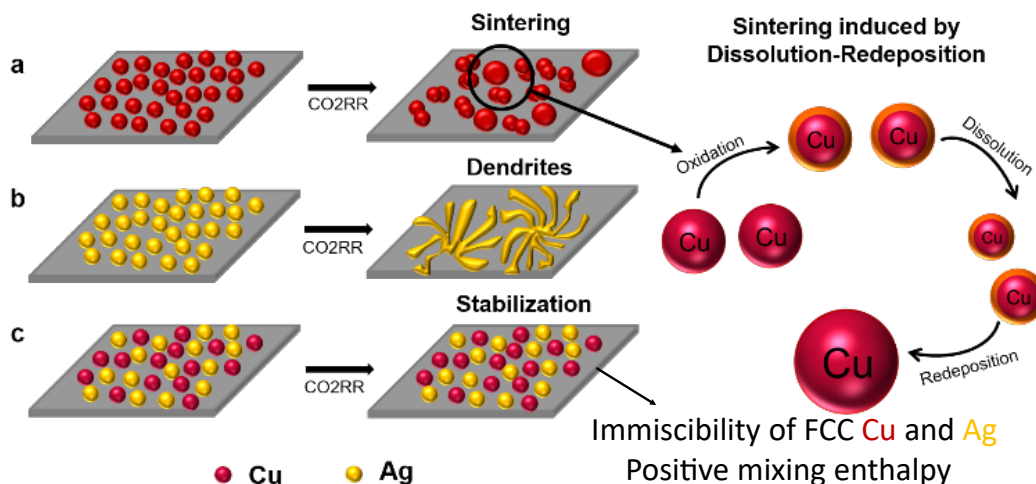


Figure 48: Illustration of the proposed stabilization effect

3.4.6 Electrochemical active surface area

To provide evidence for the observed stabilization effect, the electrochemically active surface area was determined for mono- and bimetallic electrodes. Because stabilization only occurs upon mixing of the Cu and Ag nanoparticles, the surface area of the bimetallic nanoparticle electrode is expected to be much larger after the CO₂RR compared to the mono-metallic electrodes that suffer from severe aggregation as shown in the previous sections.

The electrochemically active surface area (ECSA) was determined from the electrochemical double layer capacitance. Cyclic voltammograms were measured in the non faradaic region with various scan rates of single element and binary electrodes after an hour of the CO₂RR at -1.0 V vs. RHE. The ECSA was calculated determined from the following relationships:

$$\text{ECSA} = R_f \times S = C/C_s \times S \quad R_f = C/C_s \quad (9)$$

Where R_f is the roughness factor, C is the double layer capacitance of the sample in Farad ($F = A^2s^4kg^{-1}m^{-2}$) and C_s is the double layer capacitance of the substrate (glassy carbon), and S is the geometric surface area of the electrode (1.0 cm^2). A linear fit of the charging current with respect to the various scan rates provided the electrochemical double layer capacitance C (figure 49a). The capacitance was determined to be $8.6 \mu F$ for the glassy carbon substrate and 233 , 254 and $528 \mu F$ for the Cu, Ag and Cu-Ag nanoparticle electrodes. From the equation 9, the ECSA were determined to be 26 and 30 cm^2 for the single element Cu and Ag nanoparticle electrodes respectively and a much larger ECSA of 104 cm^2 for the binary nanoparticle electrode after catalysis. The large ECSA of the binary electrode with respect to the single element electrodes is most likely an indication of the preserved nanoscale structure of the electrode films by the stabilization effect (section 3.4.5)

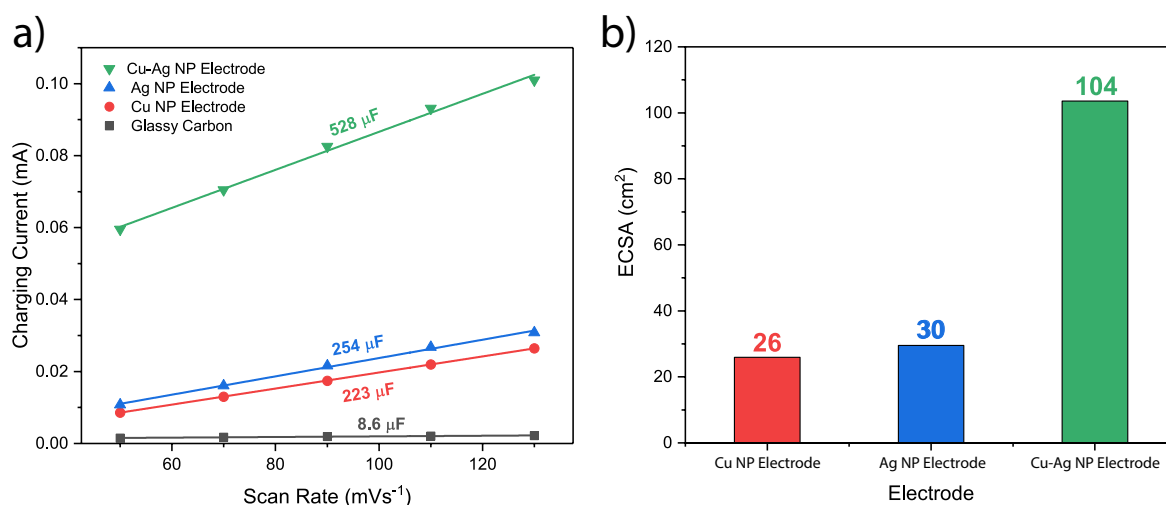


Figure 49: a) linear fit of the charging current measured from cyclic voltammograms in the non-faradaic region of the respective electrodes measured after an hour of the CO₂RR at -1.0 V vs RHE and (b) the determined electrochemical active surface area of the single element and binary electrodes in cm².

3.4.7 Cu and Cu-Ag nanoparticle electrodes by electrophoresis deposition faradaic efficiency/stability

Even though a well mixed colloidal solution is used for drop-casting, the resulting electrode film can still consist of Ag and Cu rich domains, which were highly sensitive to aggregation. To ensure stabilization, the electrode film must consist of a high degree of mixed nanoparticles. A second deposition method was used to develop highly mono-metallic and bimetallic nanoparticle electrodes by electrophoresis deposition.

The faradaic efficiencies of single element Cu nanoparticle electrode and $\text{Cu}_{1.0}\text{-Ag}_{2.5}$ (molar ratio $\text{Cu}/\text{Ag} = 2.5$) binary nanoparticle electrodes prepared by electrophoresis are presented in figure 50a. The faradaic efficiency of each of the films has a large contribution (70-80%) towards H_2 production, similar to the nanoparticle electrodes made by dropcasting, as a result of the highly under-coordinated surface species. By increasing the Cu nanoparticle layer thickness a faradaic efficiency increase from 0 to 7.5% of CH_4 is seen for the thick Cu nanoparticle electrode while the CO selectivity remains similar (around 6%). Furthermore, the selectivity of formic acid is suppressed from 12.5% to 8.7% by increasing the thickness of the Cu nanoparticle layer. Formic acid and CO are products that are derived from separate competing pathways, of which only the pathway that creates CO can lead to hydrocarbons (section 1.2.1). Therefore, by a decrease in intermediate steps that lead to the formate pathway, the pathway towards CO and hydrocarbons such as methane are increased as observed in previous research.^{19,28,35} By mixing of Cu and Ag nanoparticles the faradaic efficiency for CO was increased from 5.2% to 8.8% and for CH_4 from 7.5% to 10.3%. The faradaic efficiency for formic acid was further suppressed from 8.7% to 5.2%. Similar to the electrodes prepared by drop-casting, a series of SEM imaging experiments were performed to gain insight in the relationship between selectivity and nanoparticle electrode structure.

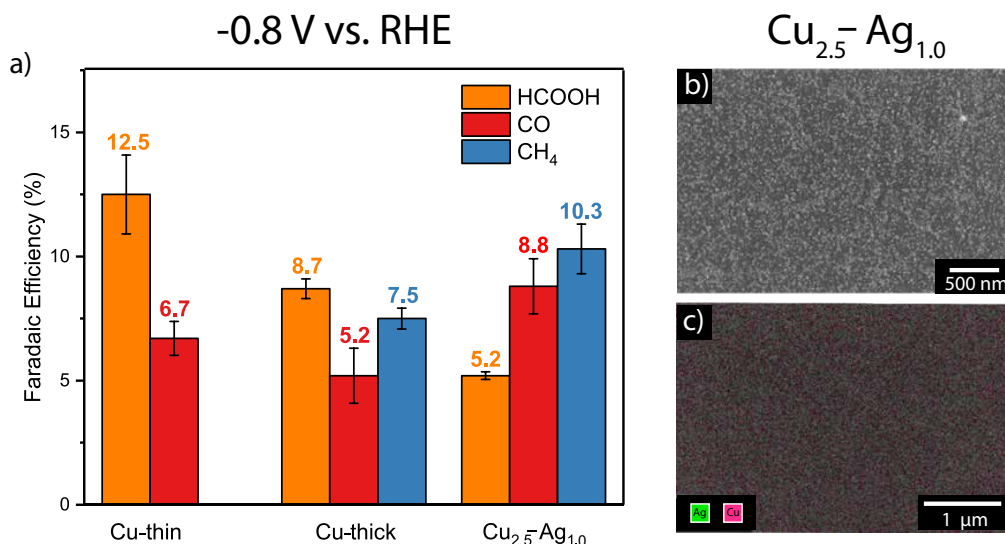


Figure 50: a) Faradaic efficiency for the CO_2RR of Cu and $\text{Cu}_{1.0}\text{-Ag}_{2.5}$ nanoparticle electrodes prepared by electrophoresis at -0.8 V vs. RHE for an hour and (b) a SEM image of the pristine $\text{Cu}_{1.0}\text{-Ag}_{2.5}$ binary nanoparticle electrode with (c) the corresponding EDX elemental map.

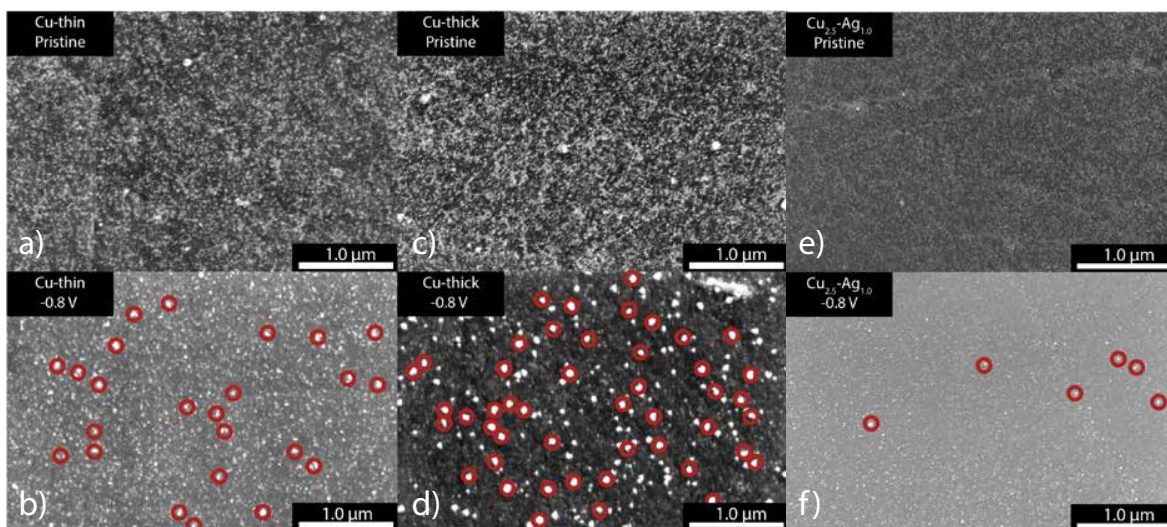


Figure 51: SEM images of Cu-thin (a,b), Cu-thick (c,d) and Cu_{1.0}-Ag_{2.5} binary nanoparticle electrode before (a, c, e) and after (b, d, f) the CO₂RR at -0.8 V vs. RHE for 1 hour. Red circles highlight domains of aggregated nanoparticles.

By comparing the SEM images of the pristine and spent Cu nanoparticle electrodes, it can be seen that domains are formed of aggregated nanoparticles at an applied potential of -0.8 V vs. RHE, similar to the drop-casted electrodes however, less severe. Also, a difference in the extent to which aggregation occurs is seen between the Cu-thin and Cu-thick samples. For higher density nanoparticle films the effect of dissolution re deposition is more likely to cause large aggregated structures. The increase in faradaic efficiency for methane of Cu-thick with respect to Cu-thin is most likely the result of these larger Cu domains formed by nanoparticle aggregation by the conversion of highly undercoordinated surface species into Cu(111) facets which are known to be selective for methane.

From the SEM image of the Cu_{1.0}-Ag_{2.5} binary nanoparticle electrode and its corresponding elemental map in figures 50b and d, it can be seen that the electrode film consists of a well-mixed layer of Cu and Ag nanoparticles. On the SEM image of the spent binary nanoparticle electrode, less domains of aggregated nanoparticles can be seen as for the pure Cu nanoparticle electrode. This result is again attributed to the stabilization effect by the immiscible character of Cu and Ag and the smaller inter-particle distances acquired by the electrophoretic deposition method. The increase in faradaic efficiency for CO of the Cu_{1.0}-Ag_{2.5} electrode (8.8%) compared to the pure Cu electrode (5.2%) is attributed to the presence of stable Ag nanoparticles which favour CO production. Furthermore, the faradaic efficiency for methane increased to 10.3%, which could be attributed to the stabilized Cu nanoparticles,⁸²⁻⁸⁶ which resulted in full or partial conservation of its original icosahedral shape rich in Cu(111) surface facets. The overall CO₂RR faradaic efficiency to C products for Cu-thin, Cu-thick and Cu_{1.0}-Ag_{2.5} are 19.2, 21.4 and 24.4% respectively. The increased faradaic efficiency of the binary nanoparticle electrode could be attributed to CO spillover. The CO produced from the Ag nanoparticles is spilled over to active sites on Cu nanoparticles resulting in the perceived increase in faradaic efficiency for methane and the reduction of formate by the stimulation of the CO pathway (section 1.2.3).^{16,35,84,87}

3.4.8 Comparison between drop-casting and electrophoresis deposition

Compared to the dropcasted nanoparticle electrodes, the overall nanoparticle loading is less dense for the catalytic films created by electrophoresis to the films prepared by drop-casting. As the films made by electrophoresis are made by forcing nanoparticles onto the substrate by an applied electric field, instead of layer formation by assembly of individual nanoparticles. This results in a larger distance between individual nanoparticles compared to drop-casting. The larger distance between nanoparticles explains the less severe aggregation that occurs on the Cu nanoparticle electrodes made by electrophoresis compared to the dropcasted electrodes as dissolutes are less likely to redeposit on nanoparticles instead of the substrate.

Furthermore as the colloidal solution is submitted to an electric field, negatively charged species such as the organic ligands (TDPA and oleic acid) are likely separated from the positively charged nanoparticles during electrophoresis deposition. The ligand stripping before catalytic testing could explain why the electrode films prepared by electrodeposition are active at a low applied reducing potential of -0.8 V vs. RHE compared to the dropcasted electrodes.

With respect to Ag and Cu nanoparticle mixing, the films made by electrophoresis are well mixed compared to the dropcasted nanoparticle binary electrodes. By dropcasting the nanoparticle films are the result of assembly of nanoparticles. Due to the small difference in Cu and Ag nano particle size, ordered patterns of the same metal nanoparticles are preferred resulting in local Cu and Ag domains, which are prone to form aggregates at mild CO₂RR conditions already at -0.8 V vs. RHE. Further increasing the applied potential resulted in total phase separation across the binary, stirring the faradaic efficiency towards their bulk component. The well mixed binary nanoparticle electrodes prepared by electrophoresis showed little of such aggregates compared to the dropcasted binary electrode at -0.8 V vs. RHE. The stabilisation effect caused by the immiscible character of Cu and Ag, is therefore more pronounced for catalytic films created by electrophoresis, combined with the larger acquirable distances between nanoparticles.

4 Conclusions

Highly monodisperse Cu and Ag nanoparticles were synthesised by colloidal chemistry. The shape of both metallic nanoparticles can be approximated as icosahedral from the presence of pentatwinned domains throughout the particles as was determined by STEM-HAADF. Furthermore it was perceived by imaging that (111) facet was the dominant surface facet for both the Ag and Cu nanoparticles. Of the Cu nanoparticles it was determined that Cu-oxide species formed rapidly when the Cu nanoparticles were exposed to air causing the loss of their defined shape. The Ag nanoparticles however, remained stable when exposed to the same conditions. From the colloidal solutions, single element and binary nanoparticle electrode films were developed by drop-casting and electrophoresis deposition. The nanoparticle electrode films from drop-casting resulted in dense nanoparticle films with small interparticle distances as a result of self-assembly that could be approximated by the length of the intervening ligands. The films created by electrophoresis deposition were less dense in comparison, however the distribution of Cu and Ag for the binary electrode was more homogeneous. By a combination of *in situ* and *ex situ* vibrational spectroscopy techniques the oxide species and ligands of a Cu nanoparticle electrode prepared by dropcasting were studied under CO₂RR conditions. It was determined that the observed Cu₂O was reduced and the coordinating ligands of the Cu nanoparticles were removed once a reducing potential of -1.0 V vs. RHE was applied during the CO₂RR. The monometallic Cu and Ag nanoparticle electrode films developed by dropcasting and electrophoresis deposition were found to be very unstable even at moderate CO₂RR conditions (-0.8 V vs. RHE), resulting in large domains of Cu and Ag aggregates with faradaic selectivities similar to their bulk component. For the binary electrodes, a stabilization effect between Cu and Ag nanoparticles was observed at the same potential. By stabilizing the Ag en Cu nanoparticles the intrinsic selectivity could be determined, which was evaluated to be 9% faradaic efficiency for CO from the Ag nanoparticles and 10% for methane from the Cu nanoparticles at -0.8 V vs RHE. For the binary films created by electrophoresis, the stabilization effect was determined to be more significant as a result of the well mixed morphology of Cu and Ag nanoparticles compared to the electrode films by dropcasting. Furthermore, the films prepared by electrophoresis deposition were determined to be less dense in nanoparticles which was correlated to increased stability. The observed stabilization effect by the mixture of Cu and Ag nanoparticles provides an efficient approach to prepare CO₂RR catalysts with increased durability. as well as an alternative way to study the intrinsic selectivity of colloidal nanoparticle electrodes.

5 Outlook

The observed stabilisation effect by the addition of Ag nanoparticles to a Cu nanoparticle based electrode could be used to enhance the durability of well performing Cu based nanoelectrodes and might even enhance selectivity towards hydrocarbons as a result of CO that is spilled over CO. For example, Cu nanoparticle electrodes that are rich in Cu(100) surface facets could be combined with Ag nanoparticles to develop a nanoscale electrode that is high in selectivity for ethylene and highly stable because of the Cu/Ag stabilization effect. The effectiveness of the stabilization effect can be further investigated with the used of specialized electrochemical cells. For examples, gas diffusion electrodes and membrane electrode assemblies have been imported to greatly increase activity by the minimization of mass transfer limitations but more importantly by much higher achievable current densities compared to conventional aqueous-phase reactors.¹⁰⁻¹² It would therefore be interesting to test the strength of the stabilized Cu/Ag nanoparticle electrode in a specialised cell where the electrode is exposed to much higher current.

It was proven in this thesis that the oleic acid and TDPA ligated Cu nanoparticles were highly sensitive to oxidation. As oxidation is the first step in the dissolution redepositon degradation mechanism of Cu nanoparticles, oxidation prevention could increase nanoparticle electrode stability drastically. The used surfactant molecules play a key role in the stabilization rate of the Cu nanoparticle when exposed to ambient or general oxidizing conditions.^{88,89} Contributing factors to oxidation rate include the length of the hydrocarbon tail, and the chemical nature of the functional head group of the ligand. After the synthesis of the desired Cu nanocrystal structure with the respective required ligands, with the use of ligand exchange techniques, a ligand can be coordinated to the Cu nanocrystal that drastically decreases the oxidation rate. This allows for the preservation of the original crystal structure when developing and assembling the electrodes for activity measurements. When exposed to the electrolyte at open circuit potential, the nanoparticles should be protected. Once a reducing potential is applied the ligands should be removed by potential induced ligand stripping while hopefully preserving the original structure. As the initial oxidation of the electrode is prevented, dissolution redepositon is less likely to be prevalent and the nanoparticle electrode should be more stable as a result.

Appendix

Original synthesis procedure

Copper NPs are prepared by decomposition of Copper(I)acetate (CuOAc) in Trioctylamine (TOA) in the presence of the surfactant Tetradecylphosphonic acid (TDPA).

Degass the solution of 123 mg of CuOAc and 278 mg of TDPA in 10 ml of TOA and 10 ml of 1-Octadecene for 1 hour at 100 °C under vacuum. Rapidly heat the solution to 180 °C under a nitrogen or argon atmosphere and maintain that temperature for 30 minutes followed up by rapidly heating to 270 °C and maintaining the temperature for an additional 30 minutes. Cool the colloidal dispersion to room temperature and remove the nanoparticles using air free techniques.

Removal of the nanoparticles for characterization and particle loading.

Extract the colloidal solution using air free techniques and disperse in a small amount of hexane. Precipitate the colloidal particles with a 1:1 ratio of anhydrous polar antisolvent (e.g. methanol/butanol or isopropanol). Separate the nanoparticles from the solution by centrifuging at 3000 rpm for 3 minutes. Decant the supernatant using air free techniques. Redisperse the nanoparticles in hexane and store in a glovebox.

Reference IR-Spectrum

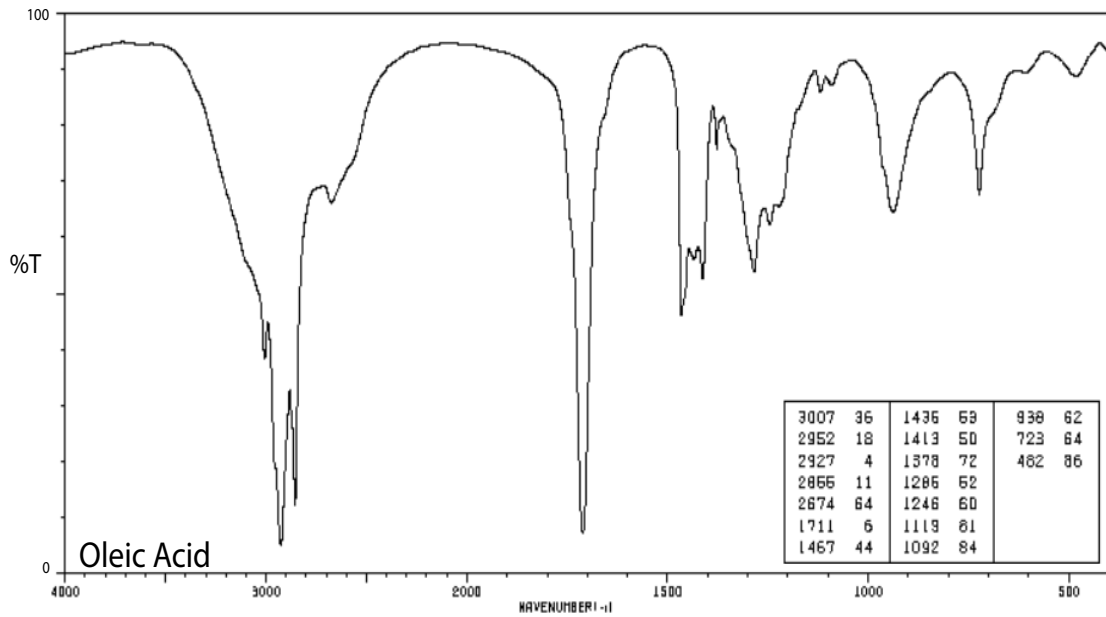
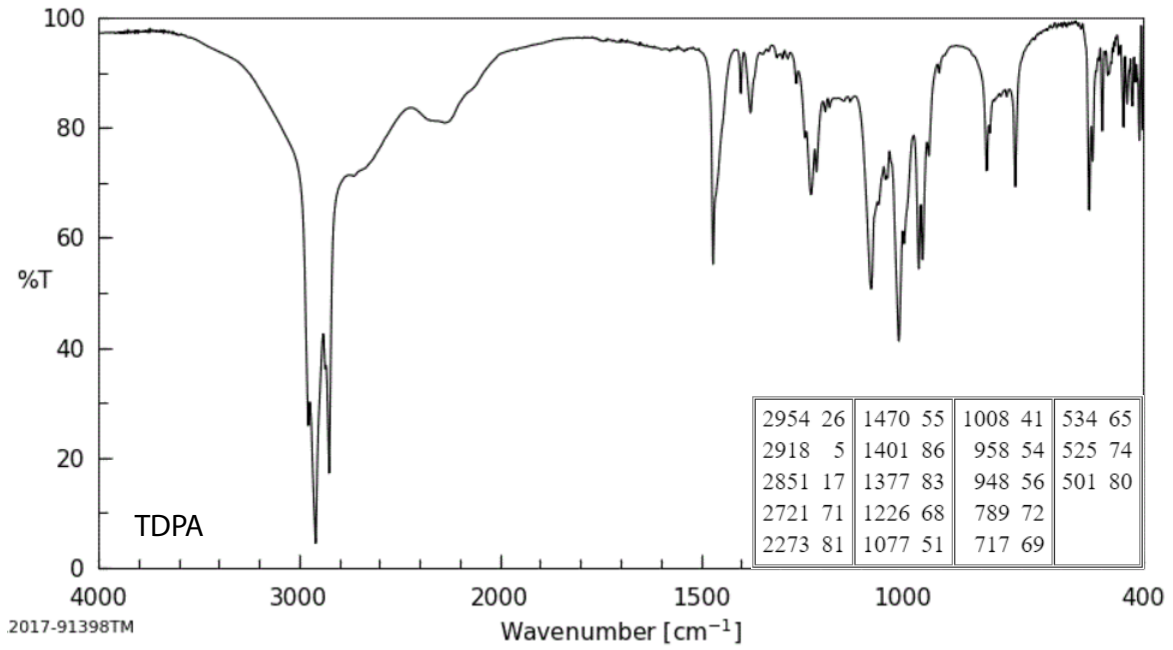


Figure 52: Reference IR spectrum of TDPA and Oleic acid.

Pourbaix diagram

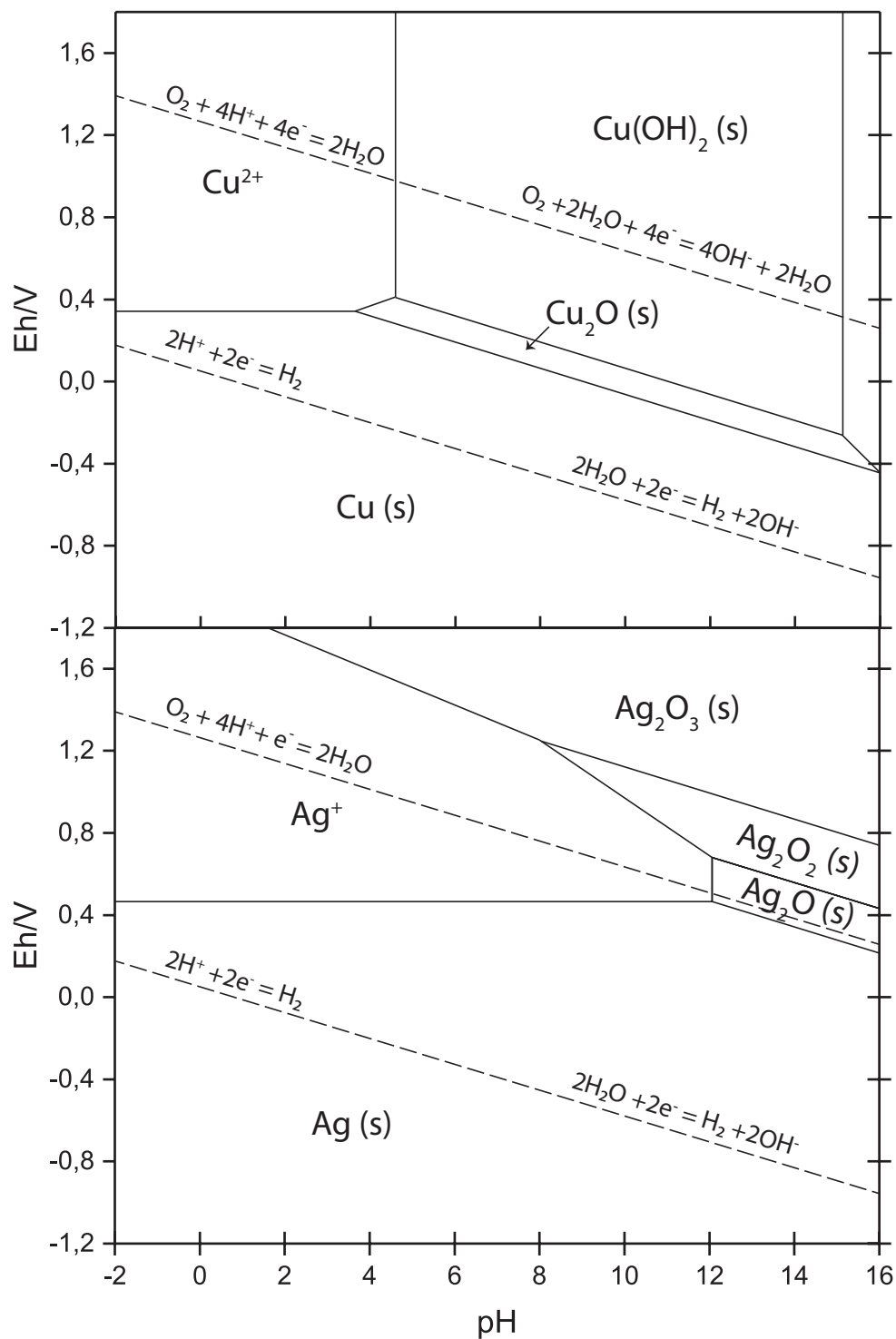


Figure 53: Pourbaix diagram of Cu and Ag (V vs. SHE) in water.

Cu nanoparticle electrode faradaic efficiency over time

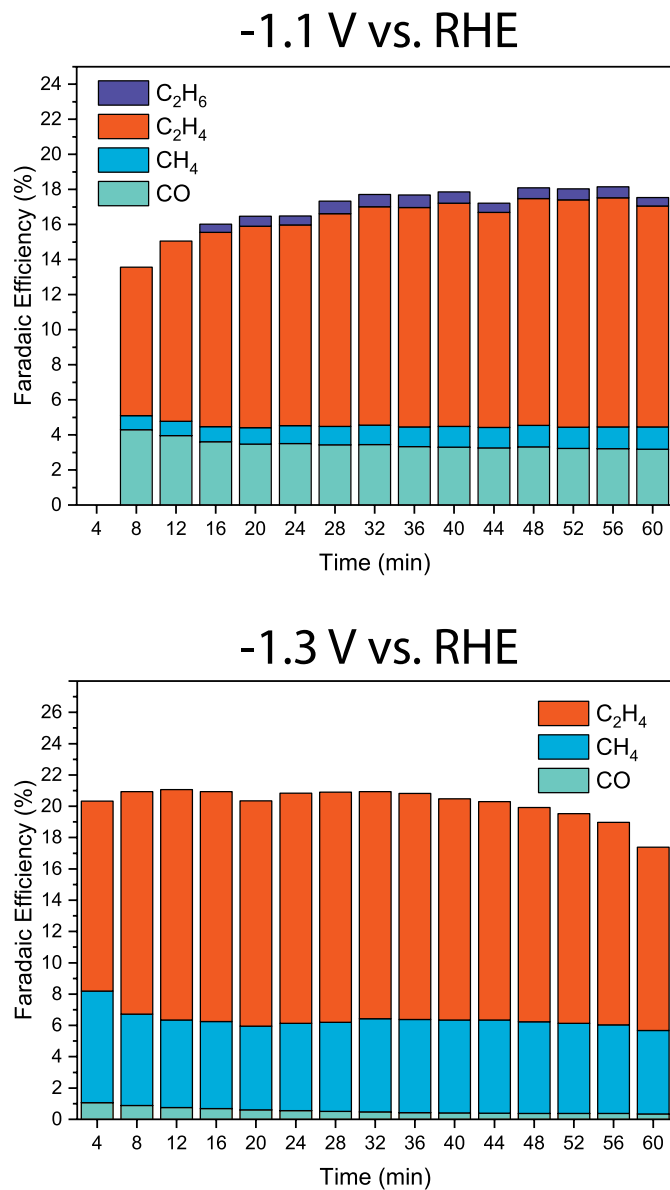


Figure 54: Faradaic efficiency of a Cu nanoparticle electrode over time at -1.1 (top) and -1.3 (bottom) V vs. RHE.

Ag nanoparticle electrode faradaic efficiency over time

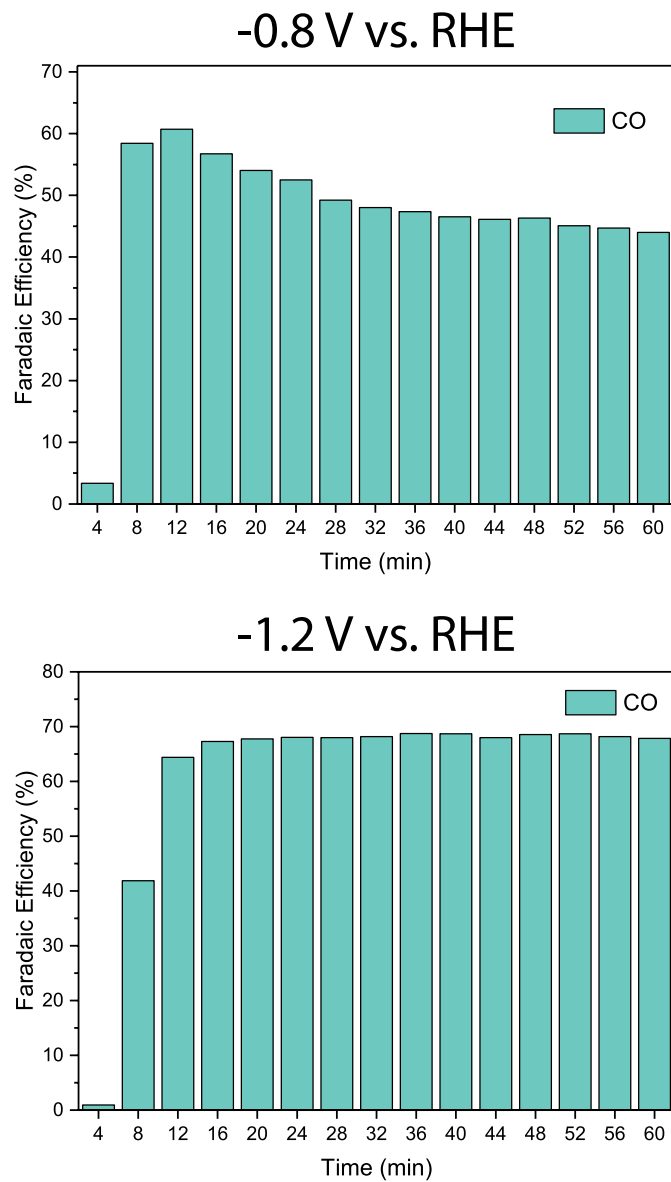


Figure 55: Faradaic efficiency of a Ag nanoparticle electrode over time at -0.8 (top) and -1.2 (bottom) V vs. RHE.

References

- (1) Rogelj, J.; Den Elzen, M.; Höhne, N.; Fransen, T.; Fekete, H.; Winkler, H.; Schaeffer, R.; Sha, F.; Riahi, K.; Meinshausen, M. *Nature* **2016**, *534*, 631–639.
- (2) Vogt, C.; Monai, M.; Kramer, G. J.; Weckhuysen, B. M. *Nature Catalysis* **2019**, *2*, 188–197.
- (3) Zheng, Y.; Vasileff, A.; Zhou, X.; Jiao, Y.; Jaroniec, M.; Qiao, S. Z. *Journal of the American Chemical Society* **2019**, *141*, 7646–7659.
- (4) Hori, Y.; Wakebe, H.; Tsukamoto, T.; Koga, O. *Electrochimica Acta* **1994**, *39*, 1833–1839.
- (5) Peterson, A. A.; Abild-Pedersen, F.; Studt, F.; Rossmeisl, J.; Nørskov, J. K. *Energy and Environmental Science* **2010**, *3*, 1311–1315.
- (6) Peterson, A. A.; Nørskov, J. K. *Journal of Physical Chemistry Letters* **2012**, *3*, 251–258.
- (7) Hori, Y.; Wakebe, H.; Tsukamoto, T.; Koga, O. *Surface Science* **1995**, *335*, 258–263.
- (8) Takahashi, I.; Koga, O.; Hoshi, N.; Hori, Y. *Journal of Electroanalytical Chemistry* **2002**, *533*, 135–143.
- (9) Hori, Y.; Takahashi, I.; Koga, O.; Hoshi, N. *Journal of Molecular Catalysis A: Chemical* **2003**, *199*, 39–47.
- (10) De Luna, P.; Quintero-Bermudez, R.; Dinh, C. T.; Ross, M. B.; Bushuyev, O. S.; Todorović, P.; Regier, T.; Kelley, S. O.; Yang, P.; Sargent, E. H. *Nature Catalysis* **2018**, *1*, 103–110.
- (11) Ross, M. B.; Dinh, C. T.; Li, Y.; Kim, D.; De Luna, P.; Sargent, E. H.; Yang, P. *Journal of the American Chemical Society* **2017**, *139*, 9359–9363.
- (12) Ma, S.; Sadakiyo, M.; Luo, R.; Heima, M.; Yamauchi, M.; Kenis, P. J. *Journal of Power Sources* **2016**, *301*, 219–228.
- (13) Reller, C.; Krause, R.; Volkova, E.; Schmid, B.; Neubauer, S.; Rucki, A.; Schuster, M.; Schmid, G. *Advanced Energy Materials* **2017**, *7*, 1–8.
- (14) Ma, S.; Sadakiyo, M.; Heim, M.; Luo, R.; Haasch, R. T.; Gold, J. I.; Yamauchi, M.; Kenis, P. J. *Journal of the American Chemical Society* **2017**, *139*, 47–50.
- (15) Hoang, T. T.; Verma, S.; Ma, S.; Fister, T. T.; Timoshenko, J.; Frenkel, A. I.; Kenis, P. J.; Gewirth, A. A. *Journal of the American Chemical Society* **2018**, *140*, 5791–5797.
- (16) Huang, J.; Mensi, M.; Oveisi, E.; Mantella, V.; Buonsanti, R. *Journal of the American Chemical Society* **2019**, *141*, 2490–2499.
- (17) Chen, X.; Henckel, D. A.; Nwabara, U. O.; Li, Y.; Frenkel, A. I.; Fister, T. T.; Kenis, P. J.; Gewirth, A. A. *ACS Catalysis* **2020**, *10*, 672–682.
- (18) Hori, Y.; Takahashi, R.; Yoshinami, Y.; Murata, A. *Journal of Physical Chemistry B* **1997**, *101*, 7075–7081.

- (19) Schouten, K. J.; Kwon, Y.; Van Der Ham, C. J.; Qin, Z.; Koper, M. T. *Chemical Science* **2011**, *2*, 1902–1909.
- (20) Peterson, A. A.; Abild-Pedersen, F.; Studt, F.; Rossmeisl, J.; Nørskov, J. K. *Energy and Environmental Science* **2010**, *3*, 1311–1315.
- (21) Montoya, J. H.; Shi, C.; Chan, K.; Nørskov, J. K. *Journal of Physical Chemistry Letters* **2015**, *6*, 2032–2037.
- (22) Cheng, T.; Xiao, H.; Goddard, W. A. *Proceedings of the National Academy of Sciences of the United States of America* **2017**, *114*, 1795–1800.
- (23) Manthiram, K.; Beberwyck, B. J.; Alivisatos, A. P. *Journal of the American Chemical Society* **2014**, *136*, 13319–13325.
- (24) Huang, J.; Hörmann, N.; Oveisi, E.; Loiudice, A.; De Gregorio, G. L.; Andreussi, O.; Marzari, N.; Buonsanti, R. *Nature Communications* **2018**, *9*, 1–9.
- (25) Hori, Y.; Wakebe, H.; Tsukamoto, T.; Koga, O. *Electrocatalytic process of CO selectivity in electrochemical reduction of CO₂ at metal electrodes in aqueous media*; tech. rep. 11-12; 1994, pp 1833–1839.
- (26) Kuhl, K. P.; Cave, E. R.; Abram, D. N.; Jaramillo, T. F. *Energy and Environmental Science* **2012**, *5*, 7050–7059.
- (27) Montoya, J. H.; Shi, C.; Chan, K.; Nørskov, J. K. *Journal of Physical Chemistry Letters* **2015**, *6*, 2032–2037.
- (28) Kortlever, R.; Shen, J.; Schouten, K. J. P.; Calle-Vallejo, F.; Koper, M. T. *Journal of Physical Chemistry Letters* **2015**, *6*, 4073–4082.
- (29) Cheng, T.; Xiao, H.; Goddard, W. A. *Journal of Physical Chemistry Letters* **2015**, *6*, 4767–4773.
- (30) Lum, Y.; Cheng, T.; Goddard, W. A.; Ager, J. W. *Journal of the American Chemical Society* **2018**, *140*, 9337–9340.
- (31) Feaster, J. T.; Shi, C.; Cave, E. R.; Hatsukade, T.; Abram, D. N.; Kuhl, K. P.; Hahn, C.; Nørskov, J. K.; Jaramillo, T. F. *ACS Catalysis* **2017**, *7*, 4822–4827.
- (32) Liu, X.; Schlexer, P.; Xiao, J.; Ji, Y.; Wang, L.; Sandberg, R. B.; Tang, M.; Brown, K. S.; Peng, H.; Ringe, S.; Hahn, C.; Jaramillo, T. F.; Nørskov, J. K.; Chan, K. *Nature Communications* **2019**, *10*, 1–10.
- (33) Garza, A. J.; Bell, A. T.; Head-Gordon, M. *ACS Catalysis* **2018**, *8*, 1490–1499.
- (34) Chernyshova, I. V.; Somasundaran, P.; Ponnurangam, S. *Proceedings of the National Academy of Sciences of the United States of America* **2018**, *115*, E9261–E9270.
- (35) Nitopi, S.; Bertheussen, E.; Scott, S. B.; Liu, X.; Engstfeld, A. K.; Horch, S.; Seger, B.; Stephens, I. E.; Chan, K.; Hahn, C.; Nørskov, J. K.; Jaramillo, T. F.; Chorkendorff, I. *Chemical Reviews* **2019**, *119*, 7610–7672.
- (36) Singh, M. R.; Kwon, Y.; Lum, Y.; Ager, J. W.; Bell, A. T. *Journal of the American Chemical Society* **2016**, *138*, 13006–13012.
- (37) Lum, Y.; Ager, J. W. *Angewandte Chemie - International Edition* **2018**, *57*, 551–554.

- (38) Resasco, J.; Chen, L. D.; Clark, E.; Tsai, C.; Hahn, C.; Jaramillo, T. F.; Chan, K.; Bell, A. T. *Journal of the American Chemical Society* **2017**, *139*, 11277–11287.
- (39) Singh, M. R.; Kwon, Y.; Lum, Y.; Ager, J. W.; Bell, A. T. *Journal of the American Chemical Society* **2016**, *138*, 13006–13012.
- (40) Kyriacou, G. Z.; Anagnostopoulos, A. K. *Journal of Applied Electrochemistry* **1993**, *23*, 483–486.
- (41) Pérez-Gallent, E.; Marcandalli, G.; Figueiredo, M. C.; Calle-Vallejo, F.; Koper, M. T. *Journal of the American Chemical Society* **2017**, *139*, 16412–16419.
- (42) Elgrishi, N.; Rountree, K. J.; McCarthy, B. D.; Rountree, E. S.; Eisenhart, T. T.; Dempsey, J. L. *Journal of Chemical Education* **2018**, *95*, 197–206.
- (43) Deng, Y.; Handoko, A. D.; Du, Y.; Xi, S.; Yeo, B. S. *ACS Catalysis* **2016**, *6*, 2473–2481.
- (44) Dunwell, M.; Yan, Y.; Xu, B. Understanding the influence of the electrochemical double-layer on heterogeneous electrochemical reactions, 2018.
- (45) Liang, Z. Q. et al. *Nature Communications* **2018**, *9*, 1–8.
- (46) Nie, X.; Esopi, M. R.; Janik, M. J.; Asthagiri, A. *Angewandte Chemie* **2013**, *125*, 2519–2522.
- (47) Cheng, T.; Xiao, H.; Goddard, W. A. *Journal of Physical Chemistry Letters* **2015**, *6*, 4767–4773.
- (48) Akhade, S. A.; Luo, W.; Nie, X.; Asthagiri, A.; Janik, M. J. *Catalysis Science and Technology* **2016**, *6*, 1042–1053.
- (49) Gattrell, M.; Gupta, N.; Co, A. *Energy Conversion and Management* **2007**, *48*, 1255–1265.
- (50) Montoya, J. H.; Shi, C.; Chan, K.; Nørskov, J. K. *Journal of Physical Chemistry Letters* **2015**, *6*, 2032–2037.
- (51) Goodpaster, J. D.; Bell, A. T.; Head-Gordon, M. *Journal of Physical Chemistry Letters* **2016**, *7*, 1471–1477.
- (52) Calle-Vallejo, F.; Koper, M. T. M. *Angewandte Chemie* **2013**, *125*, 7423–7426.
- (53) Lee, S.; Park, G.; Lee, J. *ACS Catalysis* **2017**, *7*, 8594–8604.
- (54) Ren, D.; Ang, B. S. H.; Yeo, B. S. *ACS Catalysis* **2016**, *6*, 8239–8247.
- (55) Hoang, T. T.; Verma, S.; Ma, S.; Fister, T. T.; Timoshenko, J.; Frenkel, A. I.; Kenis, P. J.; Gewirth, A. A. *Journal of the American Chemical Society* **2018**, *140*, 5791–5797.
- (56) Morales-Guio, C. G.; Cave, E. R.; Nitopi, S. A.; Feaster, J. T.; Wang, L.; Kuhl, K. P.; Jackson, A.; Johnson, N. C.; Abram, D. N.; Hatsukade, T.; Hahn, C.; Jaramillo, T. F. *Nature Catalysis* **2018**, *1*, 764–771.
- (57) Lum, Y.; Ager, J. W. *Energy and Environmental Science* **2018**, *11*, 2935–2944.
- (58) Kitchin, J. R.; Nørskov, J. K.; Barteau, M. A.; Chen, J. G. *Physical Review Letters* **2004**, *93*, 156801.

- (59) Kitchin, J. R.; Nørskov, J. K.; Barteau, M. A.; Chen, J. G. *Journal of Chemical Physics* **2004**, *120*, 10240–10246.
- (60) Davey, W. P. *Physical Review* **1925**, *25*, 753–761.
- (61) Lamer, V. K.; Dinegar, R. H. *Journal of the American Chemical Society* **1950**, *72*, 4847–4854.
- (62) Whitehead, C. B.; Özkar, S.; Finke, R. G. *Chemistry of Materials* **2019**, *31*, 7116–7132.
- (63) Van Embden, J.; Chesman, A. S.; Jasieniak, J. J. *Chemistry of Materials* **2015**, *27*, 2246–2285.
- (64) Timonen, J. V. I.; Seppälä, E. T.; Ikkala, O.; Ras, R. H. A. *Angewandte Chemie* **2011**, *123*, 2128–2132.
- (65) Owen, J. S.; Chan, E. M.; Liu, H.; Alivisatos, A. P. *Journal of the American Chemical Society* **2010**, *132*, 18206–18213.
- (66) Abe, S.; Čapek, R. K.; De Geyter, B.; Hens, Z. *ACS Nano* **2012**, *6*, 42–53.
- (67) Auer, S.; Frenkel, D. *Prediction of absolute crystal-nucleation rate in hard-sphere colloids*; tech. rep. 6823; 2001, pp 1020–1023.
- (68) Pearson, R. G. *Science* **1966**, *151*, 172–177.
- (69) Kelly, K. L.; Coronado, E.; Zhao, L. L.; Schatz, G. C. *Journal of Physical Chemistry B* **2003**, *107*, 668–677.
- (70) Yang, K.; Peng, H.; Wen, Y.; Li, N. *Applied Surface Science* **2010**, *256*, 3093–3097.
- (71) Luschtinetz, R.; Seifert, G.; Jaehne, E.; Adler, H. J. P. *Macromolecular Symposia* **2007**, *254*, 248–253.
- (72) Li, X.; Wang, S.; Li, L.; Sun, Y.; Xie, Y. *Journal of the American Chemical Society* **2020**, *142*, 9567–9581.
- (73) Deng, Y.; Yeo, B. S. *ACS Catalysis* **2017**, *7*, 7873–7889.
- (74) Xu, K.; Vickers, E. T.; Rao, L.; Lindley, S. A.; Allen, A. C.; Luo, B.; Li, X.; Zhang, J. Z. *Chemistry - A European Journal* **2019**, *25*, 5014–5021.
- (75) Goodling, A. E.; Nagelberg, S.; Kaehr, B.; Meredith, C. H.; Cheon, S. I.; Saunders, A. P.; Kolle, M.; Zarzar, L. D. *Nature* **2019**, *566*, 523–527.
- (76) Reske, R.; Mistry, H.; Behafarid, F.; Roldan Cuenya, B.; Strasser, P. *Journal of the American Chemical Society* **2014**, *136*, 6978–6986.
- (77) Popović, S.; Smiljanić, M.; Jovanović, P.; Vavra, J.; Buonsanti, R.; Hodnik, N. *Angewandte Chemie - International Edition* **2020**, *59*, 14736–14746.
- (78) Manthiram, K.; Surendranath, Y.; Alivisatos, A. P. *Journal of the American Chemical Society* **2014**, *136*, 7237–7240.
- (79) Subramanian, P. R.; Systems, U. E.; Perepezko, J. H. **1993**, *14*, 62–75.
- (80) Elofsson, V.; Almyras, G. A.; Lü, B.; Boyd, R. D.; Sarakinos, K. *Acta Materialia* **2016**, *110*, 114–121.

- (81) Nag, S.; Mahdak, K. C.; Devaraj, A.; Gohil, S.; Ayyub, P.; Banerjee, R. *Journal of Materials Science* **2009**, *44*, 3393–3401.
- (82) Clark, E. L.; Hahn, C.; Jaramillo, T. F.; Bell, A. T. *Journal of the American Chemical Society* **2017**, *139*, 15848–15857.
- (83) O'Mara, P. B.; Wilde, P.; Benedetti, T. M.; Andronescu, C.; Cheong, S.; Gooding, J. J.; Tilley, R. D.; Schuhmann, W. *Journal of the American Chemical Society* **2019**, *141*, 14093–14097.
- (84) Gurudayal, G.; Perone, D.; Malani, S.; Lum, Y.; Haussener, S.; Ager, J. W. *ACS Applied Energy Materials* **2019**, *2*, 4551–4559.
- (85) Lee, S.; Park, G.; Lee, J. *ACS Catalysis* **2017**, *7*, 8594–8604.
- (86) Liu, K.; Ma, M.; Wu, L.; Valenti, M.; Cardenas-Morcoso, D.; Hofmann, J. P.; Bisquert, J.; Gimenez, S.; Smith, W. A. *ACS Applied Materials and Interfaces* **2019**, *11*, 16546–16555.
- (87) Kim, D.; Resasco, J.; Yu, Y.; Asiri, A. M.; Yang, P. *Nature Communications* **2014**, *5*, 4948–4956.
- (88) Kanninen, P.; Johans, C.; Merta, J.; Kontturi, K. *Journal of Colloid and Interface Science* **2008**, *318*, 88–95.
- (89) Cure, J.; Glaria, A.; Collière, V.; Fazzini, P. F.; Mlayah, A.; Chaudret, B.; Fau, P. *Journal of Physical Chemistry C* **2017**, *121*, 5253–5260.